Off-Axis Texture and Crystallographic Accommodation in Multicomponent Nitride Thin Films Deposited by Pulsed Magnetron Sputtering

THÈSE N^{O} 5547 (2012)

PRÉSENTÉE LE 16 NOVEMBRE 2012
À LA FACULTÉ DES SCIENCES DE BASE
LABORATOIRE DE PHYSIQUE DE LA MATIÈRE COMPLEXE
PROGRAMME DOCTORAL EN PHYSIQUE

ÉCOLE POLYTECHNIQUE FÉDÉRALE DE LAUSANNE

POUR L'OBTENTION DU GRADE DE DOCTEUR ÈS SCIENCES

PAR

Akshath Raghu SHETTY

acceptée sur proposition du jury:

Prof. V. Savona, président du jury
Prof. L. Forró, Dr A. Karimi, directeurs de thèse
Prof. A. Dommann, rapporteur
Prof. P. Muralt, rapporteur
Dr A. Santana, rapporteur

ÉCOLE POLYTECHNIQUE
FÉDÉRALE DE LAUSANNE
Suisse
2012

……TO MY FAMILY and TEACHERS

Acknowledgements

Thank you all for all that you have done.
Hard times are now turned into time of pride.
All this I managed with you by side,
Nor could I otherwise this course have run.
Kindness isn't tendered on demand;
You gave with love, not merely out of duty.
Our days are daily burnished by that beauty.
Upon your love and help I now proudly stand.

I would like to take this opportunity while submitting the PhD thesis, to express my regards to those who offered me invaluable assistance and guidance during my research.

It has been a learning experience working under the guidance of Dr. Ayat Karimi, who has been my guru and mentor. I would not be able to start and finish this thesis without his support. I am thankful to him for his valuable suggestions, inspiration, encouragement, criticism and guidance throughout the tenure of this research. I wish to express sincere thanks to Prof. L. Forro, Head of LPMC, for this support during the PhD thesis. I would like to acknowledge the opportunities and funding provided by Swiss National Fund (SNF) during my doctoral study at the EPFL. Special thanks to Prof. A. Dommann and Dr. Neels for their interest in my work as well as very fruitful discussions regarding pole figure XRD and stress measurements. Many thanks to CIME (Interdisciplinary Centre of Electron Microscopy) specially Dr. Cantoni, Dr. Alexander, Dr. Barbara, Mme. Fabienne, Mme. Danièle, Mme. Collette for their support, training, and advice.

Members of the jury, Prof. V. Savona, Prof. P. Muralt, Prof. A. Dommann, and Dr. A. Santana – thank you all for your careful reading and for your valuable comments and suggestions.

I sincerely thank my colleague and friend Hossein Najafi for his great support and help during my PhD thesis. Interacting with you has always been an inspiring and joyous time. My officemate Dejan Djokic thank you for the positive working environment and enjoyable discussions we had. I have learned a lot from you (Body Building). I am grateful to David Oezer for the valuable discussions and suggestions regarding crystallography and thin films. I am thankful to you for always finding time for my random queries. Axel Fanget, thank you for the French abstract and the AFM training. I am grateful to Desi Zlatko Mickovic for keeping up the good mood with this trademark humor and helping me out with the abstract. I would also like to thank Dr. R. Sanjinés, Dr. B. Alling, Dr. K. Schenk, and Dr. Berger for their advices and assistance. Gaëtan Girardin, thank you for your support and friendship. I am grateful to Massimo Spina for his help in AFM imaging. I am grateful to our secretaries, Monique Bettinger and Evelyn Ludi, for the help concerning administrative issues. I would like to thank the LPMC's "technician group", B. Gérald, G. Daniel, Florian, D. Clément, P. Bugnon, M. Doy, P. Locatelli, G. Camarda and H. Jotterhand for all their support and assistance.

I thank my friend Shrinivas for great time spent during traveling, restaurant hunting and week-end parties. They made Switzerland a fun place to live. I take this opportunity to acknowledge Prof. R. R. Deshmukh who inspired me to become a researcher. I thank all my friends and well-wishers who have stood beside me through every thick and thin, indeed.

Last but not the least, least I would like to thank my parents, my brother Anup for their patience, encouragement and moral support. And above all, I am grateful to Almighty God for the virtues he has bestowed upon me like wisdom, vision, patience, perseverance and clearing all my obstacles in my way of research.

There are so many people who contributed to various parts of this work; if unknowingly I neglect to mention your name, rest assured that I greatly appreciated your assistance.

Akshath R. Shetty

Lausanne, 2012

Abstract

The study of texture in thin films is one of the possibilities to obtain information on the fundamental physical processes which govern the thin film growth. Near the substrate, the crystalline orientation of the coating layer will usually be influenced by the surface state of the substrate (grain orientation and dimensions, roughness etc.). However, during the film deposition, the texture of the coating can evolve. This evolution is a particular interesting phenomenon in order to unravel the atomic movements occurring during the deposition.

To gain an overall picture for the evolution of texture and development of microstructure with film thickness and substrate material in nanostructured nitride films, a variety of analytical x-ray diffraction (XRD) techniques like θ–2θ scan, pole figure, and residual stress by $\sin^2\psi$ method were utilized. The coatings of $Ti_{1-x}Al_xN$ from different target compositions were deposited onto various substrates (WC-Co, glass, Si(100)). Based on the results obtained, $Ti_{0.5}Al_{0.5}N$ films on WC-Co and glass reveal that surface energy minimization at low thickness leads to the development of (002) orientation. On the other hand, the competitive growth promotes the growth of (111) planes parallel to film surface at higher thickness. However, despite the prediction of growth models, the (002) grains are not completely overgrown by (111) grains at higher thickness. Rather, the (002) grains still constitute the surface, but are tilted away from the substrate normal showing substantial in-plane alignment to allow the (111) planes remain parallel to film surface. Conversely, films on Si had a dominant (002) texture nearly parallel to the surface for all samples, not changing with thickness. This indicates that the surface and interface energy anisotropies provide the driving force for texture development. For films on WC-Co, the stress along (002) which was compressive at low thickness decreases with gradual tilt of (002) and changes to tensile at higher thickness. Tilting of (002) is to minimize the overall energy of the system as the (111) planes develop with thickness store very high compressive stress. On the contrary, the stress state in (002) grains on Si remained compressive through the film thickness. Morphological and roughness observation by SEM and AFM reveal that films on WC-Co and glass display higher roughness than on Si. This confirms that the development of <111> orientation is accompanied by an increase in surface roughness of the film. In contrast, cross-sectional TEM observations reveal a smooth surface region, and the SAED patterns and HR-TEM image support the crystallographic results regarding the texture formation for films on Si. Film hardness was measured by nanoindentation and a correlation between (111) texture, stress, hardness and the type of substrate is obtained.

However, for $Ti_{0.67}Al_{0.33}N$ films, the texture growth mechanism is similar to $Ti_{0.5}Al_{0.5}N$, but the final dominant orientation at higher thickness is (113) and not (111) as expected. Using θ–2θ scans and pole figures, we establish that the preferential orientation changes with film thickness from low index (002) across (111) to high index (113) plane. We have found that to minimize the total energy of the system, the orientation of the growing film switches from (111) to (113) with preferentially less density that causes a decrease in hardness and stress formed in the (111)-oriented grains. Different mechanisms which could explain the crossover of (002), (111), and (113) orientations through film thickness are discussed. Development of the (113) orientation is examined with respect to stress, morphology and mechanical properties.

In order to obtain further information on the crystallographic accommodation and to resolve whether the incident flux angle α plays any role in this off-axis texture formation, we have deposited series of $Ti_{0.5}Al_{0.5}N$ films under various incident angles from 0° to 60° on Si(100) substrates at room temperature. We show that both in-plane and out-of-plane crystallographic orientations respond strongly to the deposition angle. For $\alpha = 0°$, the pole figures display a (111) and (002) mixed out-of-plane orientation with random in-plane alignment. In contrast, under oblique angle deposition (OAD), inclined textures are observed with the (111) direction moving toward the incident flux direction and the (002) moving away, showing substantial in-plane alignment. This observation suggests that TiAlN crystals prefer to grow with the (002) direction perpendicular to the substrate while maintaining the minimization of the surface free energy by maximizing the (111) surface area toward the incident flux. The in-plane texture, which is randomly oriented at normal incidence, gives rise to two preferred orientations under oblique angles – one along the direction of flux and other away from the deposition source. The biaxial texture results from a competition among texture mechanisms related to surface mobilities of adatoms, geometrical and directional effects. The surface and cross-section of the films were observed by SEM. OAD films develop a kind of smooth tiles of a roof structure, with no faceted crystallites. The columns of these films were tilted toward the direction of incident flux. The dependence of (111) texture tilt angle and column angle β on the incidence flux angle α is evaluated using four well-known models. Transmission electron microscopy (TEM) study reveals a voided, intercolumnar structure with oblique growth toward the flux direction. The selected area diffraction pattern (SAED) pattern supports the pole figure observations. Measurements of the nanoindentation test were performed in order to discuss the change of mechanical properties as a function of incident flux angle. Furthermore, when the substrate temperature is elevated from room temperature to 400°C and 650°C, due to the enhanced mobility of the adatoms, the surface diffusion length overrules the self-shadowing effects in traditional OAD at ambient temperature. The mobility affects the angle of columns, off-axis angles of (111) and (002) texture as well as the microstructure and mechanical properties of the coatings. We also demonstrate that the biaxial alignment and inclination of columns is independent of film composition.

Keywords:

Competitive growth; shadowing effect; biaxial texture; fiber texture; pole figure; XRD; TiAlN; nanoindentation; evolutionary selection; adatom mobility; off-axis texture, inclined columns; texture accommodation; stress.

Résumé

L'étude de la texture dans les couches minces est l'une des possibilités pour obtenir des informations sur les processus physiques fondamentaux qui régissent la croissance des couches minces. À proximité du substrat, l'orientation cristalline de la couche de revêtement est habituellement influencée par l'état de surface du substrat (l'orientation et la dimension des grains, de la rugosité, etc.) Cependant, lors du dépôt du film, la texture du revêtement peut évoluer. Cette évolution est un phénomène particulièrement intéressant pour identifier les mouvements atomiques qui se produisent pendant le dépôt.

Pour avoir une vue d'ensemble de l'évolution de la texture et du développement de la microstructure en fonction de l'épaisseur du film et du substrat dans les films de nitrure nanostructurés, une variété d'analyses par diffraction des rayons X (XRD), telles que les balayages θ-2θ, les figures de pôle et les contraintes résiduelles par méthode $\sin^2\psi$, a été utilisée. Des couches de $Ti_{1-x}Al_xN$ ont été déposées à partir de cibles de compositions différentes sur différents substrats (WC-Co, verre, silicium (100)). Sur la base des résultats obtenus, les films $Ti_{0.5}Al_{0.5}N$ sur WC-Co et verre révèlent que la minimisation de l'énergie de surface à faible épaisseur conduit à l'élaboration d'orientation (002). D'autre part, la croissance compétitive favorise la croissance des plans (111) parallèles à la surface du film à une épaisseur plus élevée. Cependant, malgré la prédiction des modèles de croissance, les grains (002) ne sont pas complètement remplacés par des grains (111) à haute épaisseur. Au contraire, les grains (002) constituent toujours la surface, mais sont inclinées loin de la normale du substrat, démontrant un alignement dans le plan substantiel pour permettre aux plans (111) de rester parallèle à la surface du film. Inversement, les films sur silicium ont une dominante de texture (002) presque parallèle à la surface pour tous les échantillons, indépendamment de l'épaisseur. Ceci indique que la surface et les anisotropies d'énergie d'interface fournissent la force motrice pour le développement de la texture. Pour les films sur WC-Co, la contrainte le long de (002) qui est en compression à faible épaisseur diminue progressivement avec l'inclinaison de (002) et change en force de tension à plus grande épaisseur. Il y un basculement de (002) afin de minimiser l'énergie globale du système comme les plans (111) se développe avec l'épaisseur et emmagasine une très grande contrainte de compression. Au contraire, la contrainte dans les grains (002) sur Si est restée compressive quelque soit l'épaisseur du film. L'observation morphologique et de la rugosité par SEM et AFM révèle que les films sur WC-Co et verre ont une rugosité plus élevée que sur silicium. Ce qui confirme que le développement d'orientation <111> s'accompagne d'une augmentation de la rugosité de surface du film. En revanche, les observations en TEM transversales révèlent une région de surface lisse, et les motifs SAED et les images HR-TEM confirment les résultats cristallographiques concernant la formation de la texture des films sur silicium. La dureté des films a été mesurée par nano-indentation et une corrélation entre texture (111), stress, dureté et type de substrat a été obtenue.

Toutefois, pour les films $Ti_{0.67}Al_{0.33}N$, le mécanisme de croissance des textures est similaire à $Ti_{0.5}Al_{0.5}N$, mais l'orientation finale dominante à plus grande épaisseur est (113) et non (111) comme prévu. En utilisant des analyses θ-2θet et des figures de pôles, on a établit que l'orientation privilégiée change avec l'épaisseur de film, de faible indice (002), puis (111) et finalement à des plans de haut indices (113). Nous avons constaté que, pour minimiser l'énergie totale du système, l'orientation des films en croissance passe de (111) à (113) avec une densité préférentiellement inférieure, ce qui provoque une diminution de la dureté et du stress induits dans les grains orientés (111). Différents mécanismes qui pourraient expliquer le croisement d'orientations (002), (111) et (113) à travers l'épaisseur du film sont discutés. Le développement de l'orientation (113) est examiné en ce qui concerne le stress, la morphologie et les propriétés mécaniques.

Afin d'obtenir de plus amples renseignements sur le logement cristallographique et résoudre si l'angle incident du flux α joue un rôle dans la formation de la texture hors axe, nous avons déposé une série de films $Ti_{0.5}Al_{0.5}N$ sous des angles d'incidence allant de 0° à 60° sur des substrats Si (100) à température ambiante. Nous montrons que, tant dans le plan et hors plan, l'orientation cristallographique réagit fortement à l'angle de dépôt. Pour $\alpha = 0°$, les figures de pôles affiche un mélange d'orientation (111) et (002) hors du plan avec un alignement dans le plan aléatoire. En revanche, en dépôt à angle oblique (OAD), les textures observées sont inclinées, avec la direction (111) se déplaçant dans la direction du flux incident et la direction (002) dans le sens opposé, montrant un alignement dans le plan important. Cette observation suggère que les cristaux TiAlN préfèrent croitre avec la direction (002) perpendiculaire au substrat tout en maintenant la minimisation de l'énergie libre de surface et en maximisant la surface (111) vers le flux incident. La texture dans le plan, qui est orientée de façon aléatoire à incidence normale, donne naissance à deux orientations préférentielles sous des angles obliques - une le long de la direction du flux et l'autre à l'opposé de la source de dépôt. La texture biaxiale résulte d'une compétition entre les mécanismes de textures, liés à la mobilité de surface des adatomes et aux effets géométriques et directionnels. La surface et section transversale des films ont été observées en SEM. Les Films OAD développent une sorte de structure en tuiles lisses, avec cristaux sans face. Les colonnes de ces films ont été inclinées dans la direction du flux incident. La dépendance de l'ange d'inclinaisons des textures (111) et de l'angle β des colonnes avec l'incidence du flux d'angle α est évaluée au moyen de quatre modèles bien connus. La microscopie électronique à transmission (TEM) révèle une structure inter-colonnes avec une croissance oblique à la direction du flux. Les motifs de diffraction (SAED) supportent les observations tirées des figures de pôles. Les mesures de nanoindentation ont été réalisées afin de discuter de l'évolution des propriétés mécaniques en fonction de l'angle de flux incident. En outre, lorsque la température du substrat est élevée de la température ambiante jusqu'à 400°C et 650°C, en raison de la mobilité accrue des adatomes, la longueur de diffusion de surface annule les effets de l'auto-ombrage en OAD traditionnel à température ambiante. La mobilité affecte l'angle des colonnes, les angles hors axe des textures (111) et (002) ainsi que la microstructure et les propriétés mécaniques des

revêtements. Nous démontrons également que l'alignement biaxial et l'inclinaison des colonnes est indépendante de la composition du film.

Mots-clés:

Croissance compétitive; effet d'ombrage, texture biaxiale; texture fibreuse; figure de pôle; XRD; TiAlN, nanoindentation, mobilité des adatomes; texture hors axe, colonnes inclinées, accommodations de texture, stress.

Contents

Chapter 1:

Introduction

1.1 Prelude

Correlation between the process conditions and film structure has been extensively studied in the field of thin film processing. One such topic of study is the texture formation, where grains with specific crystallographic direction normal to the substrate dominate in a polycrystalline film. The texture in thin film has long been drawing much attention because various predominant orientations will cause the change of the film properties, which directly determine the application of the film.

Thin films usually exhibit strong fibre textures which develop during deposition. This texture – the dominant grain orientation – has great influence on the mechanical response of materials and consequently on the performance and reliability of components. Thus, the understanding and control of texture evolution provides at the same time a powerful tool for adjusting elastic and plastic properties. Grain growth in preferred directions causing texture evolution in thin films is driven by energy minimization. Anisotropic energies such as surface, interface and strain energy result in an orientation-dependent driving force on the grain boundaries determining the resulting texture. Polycrystalline films develop restricted crystallographic orientations, or texture, during (a) the pre-coalescence stage, (b) during coalescence and (c) during thickening of continuous films.

Texture is caused by anisotropy of certain properties, such as surface energy or reactivity. These properties depend on the crystallographic plane of deposited materials and influence film formation processes. Therefore many studies tried to relate such anisotropies to film formation processes that finally determine the preferred orientation. For fcc metal films, the texture evolution during grain growth often favours (111)-textured grains. The (111) planes in fcc metals are closed packed and (111) surfaces have a minimum density of frustrated bonds and therefore the lowest free surface energy of all possible orientations in fcc metals. At higher thickness, strain-energy-minimizing textures are favoured which result in (001) orientation. However, the texture of fcc nitrides films has been found to exhibit more complex behaviour than that of fcc metals. For instance, lowest surface energy plane of $Ti_{1-x}Al_xN$ is (002). Studies report that the (002) texture changed into (111) with increasing film thickness. What remains the subject to controversy is the driving force governing the texture change and associated orientational crossover. Indeed, grains tend to adopt a (002) orientation at low film thickness, which gradually changes to (111) as the thickness is further increased. This scenario has been confirmed by experimental studies aiming at characterizing the initial growth stages. Basically, the textural evolution of TiAlN films is explained based on thermodynamics and kinetics arguments. As such, there is a need for a model allowing us to understand the development of the structure and orientation of the TiAlN films. Many authors have observed that this microstructure and orientation is strongly influenced by the deposition conditions used. Some of them as well proposed a model in an attempt to understand the film growth. However, most of these models focused on the influence of one specific deposition parameter on the microstructure and/or the orientation, while neglecting or ignoring the possible influence of many other deposition parameters. Moreover, some models seem to be in contradiction to each other.

The morphology and texture (crystal orientation) of a film not only are the subjects of fundamental scientific interest but also of practical importance which have a direct control in many important physical properties. A recent example is the intense interest in creating biaxially oriented films. A particular technique to create a biaxial film on an arbitrary substrate (including amorphous surface) is by the inclined substrate deposition or oblique angle deposition technique. In this technique, the incident flux strikes the substrate at an angle with respect to the substrate normal. For a given material, when deposited within an appropriate substrate temperature range, a texture selection can occur to create a film with preferred out-of-plane and in-plane orientations, or a biaxially orientated film. There has been considerable effort in the past few decades focusing on the mechanism of the formation of biaxial films using oblique angle deposition techniques. It has been shown that often the competition between surface-atom mobility and shadowing effect can lead to a variety of nanostructured morphologies and a biaxially-textured film with preferred out-of-plane and in-plane crystal orientations. It is generally believed that to obtain a biaxially textured film, one needs to be in zone T region of the structure zone model (SZM).

In general, the texture evolution during the nitride film growth is very complex, and basic understanding of the phenomenon is still lacking. Many effects such as surface diffusion, surface energy-strain energy minimization, competitive growth and shadowing effect can play important roles in texture formation. On the theoretical side, there is still no computational tool which allows one to predict the formation of texture starting from initial to final stages of growth. One often starts with a seed of pre-assumed crystal orientation and builds a computational growth model based on this seed. On the experimental side, it is still a very challenging task to perform a detailed measurement of how the surface texture evolves at different growth stages. In summary, discussions about preferred orientation are not conclusive due to the lack of a comprehensive understanding of the texture determining process.

The aim of this research is to improve our understanding of the fundamental phenomena of structure formation during thin film growth, and would help to recognize mechanisms by which the off-axis texture is brought about in the nanostructured thin films.

1.2 Outline of the thesis

In this thesis, we describe the various orientations that can occur in polycrystalline films and present a comprehensive study regarding the origins of texture in reactive-sputter-deposited nitrides.

The body of thesis consists of ten chapters. Chapter 1 gives a brief introduction on texture in thin films. A review of the literature is given in chapter 2, focusing on progress made regarding the texture formation mechanism and microstructure in thin films. Chapter 3 provides a description of the experimental procedures used to synthesize and characterize the thin films. Texture evolution of $Ti_{0.5}Al_{0.5}N$ films at different thicknesses on various types of substrates is presented in chapter 4. We show that with increasing thickness (002) planes are tilted away to accommodate the fast growing (111) planes on glass and WC-Co, whereas no such off-axis tilt was seen for films on Si. The effect of this texture accommodation on the stress, microstructure and mechanical properties is investigated in chapter 5. In chapter 6, the formation of (113) texture for different film composition ($Ti_{0.67}Al_{0.33}N$) is examined. To clarify the role of deposition angle in the off-axis texture observed, $Ti_{0.5}Al_{0.5}N$ films were deposited under various incident angles at room temperature (chapter 7) and its effect on the crystallographic orientation, microstructure and mechanical properties was studied. Chapter 8 presents the effect of deposition temperature and other parameters on the texture and microstructure of films deposited under oblique angles. In chapter 9, we present a model explaining mechanism of off-axis tilt of (002) and (113) texture formation observed at higher thickness. In addition, we discuss the biaxial texture formation for films under oblique angle deposition. Finally, chapter 10 contains a summary of the results and an outlook of the possibilities for future work is given.

Chapter 2:

State of the art

2.1 Overview of the present chapter

This chapter presents an outline of the current knowledge and trends regarding various models on the growth texture mechanisms of physical vapour deposited (PVD) $Ti_{1-x}Al_xN$ films. The preferred orientation of conventional thin films can be described by a number of growth models like adatom mobility, surface energy minimization and evolutionary selection model. However, it is unclear which of the above-mentioned mechanisms dominate the texture formation in $Ti_{1-x}Al_xN$ layers. This also includes a lack of knowledge about the contribution of the different growth stages to texture formation. These facts of course limit highly accurate tailoring of film properties.

2.2 Crossover phenomena

Metal nitride thin films often exhibit a fibre texture, i.e., a crystallographic axis aligned parallel to the global growth direction, and such alignment has a profound effect on the anisotropy of physical properties obtained. For instance, some of these compounds (e.g. TiN, TiAlN, etc.) exhibit anisotropic mechanical properties and by modifying the fibre texture one may further improve their properties. Hence, great effort has been invested into describing and controlling the preferred orientation in metal nitride thin films, such as TiN, AlN, CrN, TiAlN, etc. [1].

Since the crystallographic texture can have a significant effect on the performance of the layer in certain applications, several models have been proposed to explain the mechanisms determining texture evolution in order to allow its control during deposition [2-4]. Fibre texture of transition-metal nitride films has been found to be determined by competitive columnar grain growth given by a complex interplay between thermodynamic and kinetic driving forces. From the thermodynamic point of view, texture is developed so that the film/substrate system minimizes its total free energy [5]; on the other hand, adatom surface diffusion determines the microstructural evolution if the kinetic restrictions overrule the thermodynamic effects [6].

2.2.1 Overall energy minimization model

In sputtered $Ti_{1-x}Al_xN$ films, a crossover phenomenon is frequently observed [7]: as the film thickens, a change in the crystallographic texture occurs. The evolving sequence with the increasing thickness is generally the following. At low thickness grains with (002) orientation are dominant, whereas at higher thickness the (111) orientation takes over, depending on the deposition conditions: substrate temperature [2,8-12], bias voltage [3,4,9-16], sputtering power [9,17], gas mixture [18-19], N_2 partial pressure [2,17], and energy and flux of bombarding particles [6,20-22]. The use of ion irradiation also results in the trapping of accelerated gas ions, defect incorporation, and the development of high compressive stresses [23-26]. The presence of high residual stress in TiAlN films may thus strongly affect the preferred orientation. This crossover in preferred orientation with increasing film thickness is often explained with the "minimization of the overall energy".

Pelleg and co-workers' [2] were the first to consider the overall energy of the films as the summation of the strain energy and the surface energy. By their theoretical calculation, the lowest surface energy plane is (002), while the lowest strain energy plane is (111). Accordingly, the (002) preferred orientation is predicted in the deposition conditions in which the strain energy is small and the surface energy is dominant. On the other hand, the (111) preferred orientation is predicted in the deposition conditions in which the strain energy was large and dominant. Later, Oh and Je [3] observed experimentally a critical thickness below which the TiN film had (002) preferred orientation and above which it had (111) preferred orientation (see Fig. 2.1), and considered the overall energy W of a film as the summation of the strain energy and the surface energy S and is expressed by:

$$W_{hkl} = S_{hkl} + \varepsilon^2(1-\upsilon)hE_{hkl} \tag{2.1}$$

where S_{hkl} is the surface energy per surface area and the second term is the strain energy per surface area. E_{hkl} is the Young's modulus, ε is the strain, ν is Poisson's ratio and h is the film thickness. Assuming no kinetic restrictions and considering that $S_{002} < S_{111}$ and $E_{111} > E_{002}$, TiN films will grow with (002) grains at small thicknesses, where the surface term dominates, while (111) grains appear at larger thicknesses, where in turn the strain energy dominates.

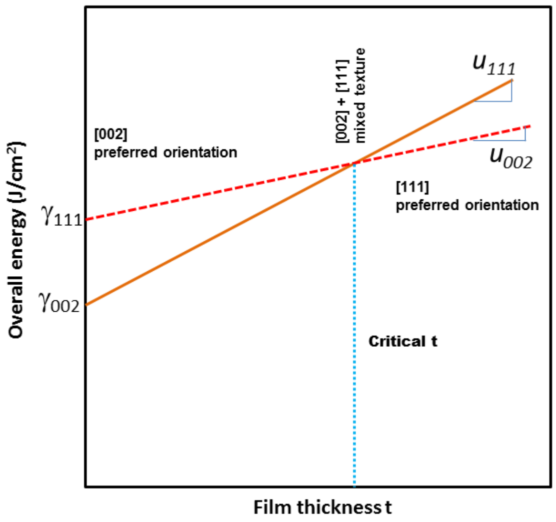

Fig. 2.1: *Variation of the overall energy of a TiN film with increasing thickness [27].*

Fig. 2.1 displays the schematic diagram illustrating the variations of the overall energies of TiN films with thickness at different levels of the strain energy per unit volume, for the planes (111) and (002). The slopes represent the strain energy per unit volume because the strain energy per unit area U_{hkl} is obtained from the product of the strain energy per unit volume u_{hkl} by the film thickness t.

Since the surface energy is dominant below the critical thickness, the overall energy of the (002) plane is lower than that of the (111). On the other hand, as the strain energy turns to be dominant above the critical thickness, the (111) plane has the lower overall energy. By the driving force to minimize the overall energy of the film, therefore, the (002) preferred orientation is developed below the critical thickness, while the (111) preferred orientation is developed above the critical thickness.

2.2.2 Contradictions to OEM model

Although this model has often been referred to, there is still discussion in the literature on its correctness since they implicitly assumed a similar strain level in (002) and (111) TiN grains which is in contradiction to results of other authors. The arguments below support the idea that the OEM model is not correct.

Abadias et al. [28] has shown by means of $\sin^2\psi$ XRD measurements using a triaxial stress model that the stress in [111]-oriented grains exceeds the stress in [002] grains. Because the OEM model explains the transition from a [002] to a [111] preferred orientation in order to minimize the strain energy, it is in contradiction with the results of Abadias et al. More precisely, according to Abadias et al. [29], changing to a [111] orientation would only increase the strain energy. Additionally, Petrov et al. [30] and Iordanova et al. [31] observed for a TiN film with mixed orientation that the [111] oriented grains are more stressed than the [002] oriented grains.

Patsalas et al.[16] showed by increasing the bias voltage during growth, the TiN films with a (002) texture exhibited a significantly higher compressive stress level than (111)-oriented TiN films. By changing the ion/metal flux ratio (J_i/J_{Ti}), Hultman and co-workers [32] demonstrated that the preferred orientation transitions do not require the presence of stress and/or do not result from changes in the stress state with the increasing film thickness. They concluded that the (111) preferred orientation developed gradually through a competitive growth under low-temperature, low ion irradiation deposition conditions, in agreement with observations of Li et al. [33] putting forward the prime role of kinetics and adatom mobilities.

2.2.3 Competitive growth model

Textured growth can also be understood as a result of growth competition between differently oriented grains. The model of evolutionary selection of specific crystallite orientations, as described by Van der Drift [34], is based on two assumptions: (i) the absence of secondary nucleation; (ii) a crystallite morphology which is independent of the crystallite orientation. The latter condition is fulfilled for large surface diffusion which ensures that growth on particular surfaces does not depend on the orientation of the surface relative to the incoming flux of growth species. Since the shape of isolated crystals at the beginning of the film growth process usually does not depend on the crystal orientation, the assumption of a large surface diffusion is very reasonable. The basic parameter which determines the film texture is the direction of fastest growth. The growth of a polycrystalline TiAlN film starts from distinct nucleation sites. As individual randomly oriented nuclei grow larger, their diameters equal the average distance between the nucleation sites and they begin to form a continuous film. The subsequent film growth is dominated by competitive growth between differently-oriented grains. With increasing film thickness, more and more grains are overgrown and buried by adjacent grains. Only those crystals with the direction of fastest growth perpendicular to the surface will survive (Fig. 2.2). The result is a pronounced fiber texture where the fiber axis equals the direction of fastest growth and the degree of texturing increases with increasing film thickness [35].

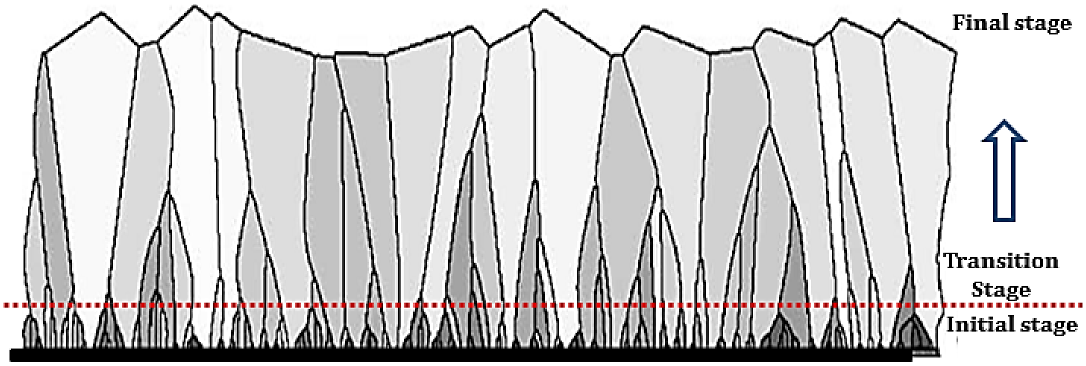

Fig. 2.2*: Schematic sketch of evolutionary selection: in the initial stage, nuclei have random orientation. During the transition stage, some grains are overgrown by their neighbors by a principle of evolutionary selection. At the final stage, only a narrow range of crystallite orientations will survive [36].*

Knuyt et al. [37-39] suggested a mechanism of texture formation that is very similar to the principle of evolutionary selection. While van der Drift concluded on the direction of fastest growth speed from typical shapes in crystal growth experiments, Knuyt suggested that there is a net preferred surface diffusion towards facets with lower surface free energies. Therefore, the principle of the minimization of the total surface free energy of the film was suggested as the driving force for evolutionary selection. As a simplification of the calculations, it was assumed that the surface free energy is a simple monotonous function of the crystallite tilt with respect to the substrate surface, which makes it quite similar to that of van der Drift who assumed orientation-dependent vertical growth speeds. However, Knuyt's model allows investigating the influence of parameters like temperature and attempting frequency, which govern surface diffusion. Very similar to the work of Knuyt is a model proposed by Smith [40], where the driving force for a net surface diffusion towards grains with specific orientations has been replaced by the surface binding energy. Both, the models from Knuyt and Smith, demonstrate the formation of a preferred orientation from an initially random distribution of crystallite orientations with increasing film thickness, while in addition Knuyt comprehensively discusses e.g. the evolution of the mean surface free energy and the angular orientation distribution as a function of time (i.e. film thickness).

2.2.4 Other texture growth models

Different mechanisms for the crossover, which is in play under different deposition conditions, were identified. Je et al. [18] observed a 'tilted-(002) surface' mechanism being responsible for the crossover. By real-time measurements with synchrotron radiation, they studied the preferred orientation in magnetron-sputtered TiN films and observed a crossover thickness, where the dominating growth direction switched from the <002> direction to the <111> direction. However, the (002) planes still constituted the surface but they were tilted away from the surface normal, so the (111) planes of the growing grains were parallel to the surface (Fig. 2.3). The surface became (002) faceted with a high surface roughness. Finally, using in-situ X-ray diffraction and reflectivity measurements at a synchrotron, Schell et al. [12] identified recrystallization as a mechanism, which was controlling the crossover in TiN films deposited by reactive magnetron sputtering.

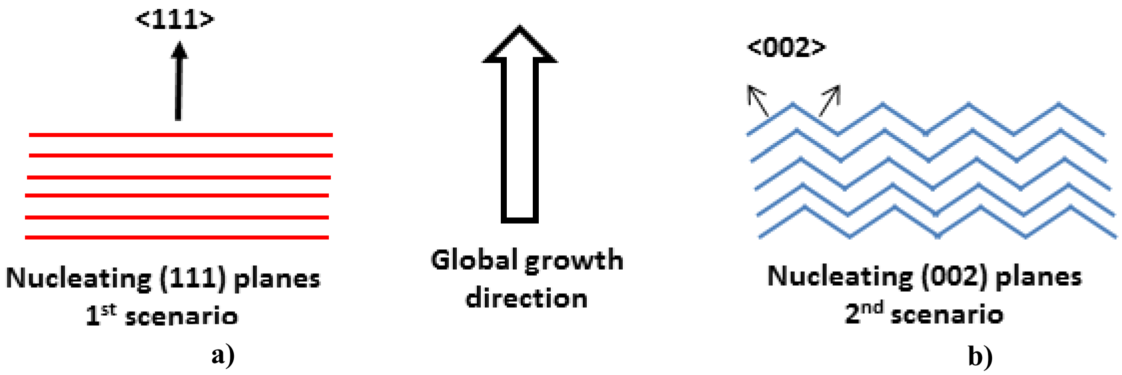

Fig. 2.3: *Schematic illustrations of the possible growth configurations of the late stage growth by Je et al.: a) nucleating the (111) microscopic planes, and b) nucleating the (002) microscopic planes [18].*

In summary, the following statements can be made which will be of great importance for the discussion and understanding of texture formation mechanisms in $Ti_{1-x}Al_xN$ films in this work:

- Texture growth can be divided into different stages: an initial stage, mainly describing nucleation and coalescence at the substrate interface (low thickness), the transition between the initial and final phase (intermediate thickness) and a final juncture describing the evolution of a thick layer (higher thickness).

- The formation of a preferred orientation (texture) can be induced by an interaction with the substrate surface (single crystal), i.e. by nucleation into a preferred orientation, during the initial growth stage.

However, despite extensive research, the physical mechanisms leading to the development of the preferred orientation in polycrystalline $Ti_{1-x}Al_xN$ layers are not yet understood. This is because the texture development in PVD films depends in a complex way on deposition conditions and process parameters, which explain why the reported results are scattered and discussions about the origin of the preferred orientation are conflicting.

2.3 Biaxial texture formation

Sputter deposited films exhibit polycrystallinity along in-plane directions (perpendicular to substrate normal) with strong preferred orientations in out-of-plane direction (parallel to substrate normal). This behavior is a natural consequence of thermodynamic restrictions. When kinetic effects appear to be dominating in a growing film, in-plane alignments (perpendicular to substrate normal) might be achieved as well [41]. Such alignments were reported for TiAlN [42,43] and TiN [44] films when they were deposited at off-normal angles or under oblique angle deposition (OAD). Such films have both out-of-plane and in-plane alignments and hence may become close to single crystalline materials. These are generally known as biaxially-textured films.

Under geometrical considerations, the columns are inclined from the film direction normal to the vapor source for oblique film deposition. The functional relation between the incidence angle, α, and the inclination angle of columns, β, known as a ‘‘tangent rule’’ was proposed empirically [45]. Previous studies have shown that increasing the deposition angle away from normal incidence typically causes a tilting of columnar grains. Dirks and Leamy [46] have reviewed the phenomenological tangent rule and its effectiveness in predicting columnar grain tilt. This relationship has been verified by a number of reports. The rule can be applied, however, only in case of limited mobility situation [47]. With respect to the crystallographic orientation, the texture axis is inclined from the substrate normal to the vapor source. There are basically three mechanisms proposed to explain the formation of textured surfaces produced by vacuum deposition at oblique angles.

These mechanisms are:

(i) evolutionary selection [34],
(ii) preferred growth [48],
(iii) self-shadowing [49]

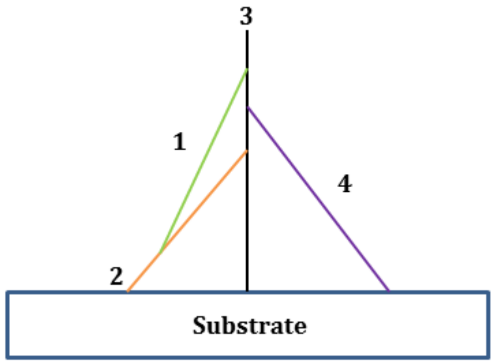

Fig. 2.4: *The evolutionary growth is shown. Although crystallites 1-4 are the same absolute length, crystallite 3 will be the only one to propagate; crystallites 1, 2 and 4 will terminate in the trunk of crystallite 3 [48].*

The concept of evolutionary selection as applied in vapor-deposited layers refers to the higher probability of survival associated with crystallites which have the greatest vertical growth rate [34]. As the layer becomes increasingly thick, orientations with nearly maximum vertical growth rate predominate as all other orientations have been eliminated through termination at adjacent crystallites (Fig. 2.4). Crystallites which are oriented most nearly normal to the substrate will usually manifest the greatest vertical growth rate. In contrast, crystallites oriented at angles other than 90° to the substrate will terminate in the shanks of the steeper crystallites. In preferred growth, one crystal direction will have a higher growth rate than other directions. The preferred growth direction is mainly dependent on the material’s self-diffusion and bonding properties [48].

Self-shadowing is a situation which occurs in vapor deposition when the growing surface is oriented at some oblique angle to the evaporation boat. Initially vapor atoms are uniformly condensed over the surface of the substrate. As the deposition proceeds, regularly distributed nuclei form and thicken under surface tension forces, resulting in deposit-free regions between the nuclei. Vapor atoms can now only condense on the upper portion of the nuclei, the interspaces between the nuclei being shadowed by the nuclei itself (Fig. 2.5). The spacing between crystallites is then a function of the angle described by the substrate and vapor beam and the deposition rate, as well as the self-diffusion and crystallographic properties of the deposited material. These three mechanisms appear to work in combination to control the texture of the resulting surface in obliquely-deposited thin films [49].

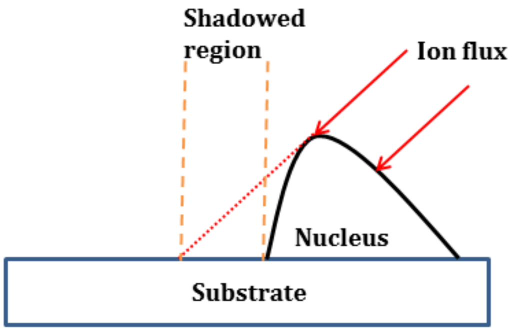

Fig. 2.5: *Schematic of self-shadowing mechanism. As the deposition proceeds, vapor atoms can only condense on the upper portion of the nucleus and the interspaces between nearest-neighbor nuclei are shadowed by the nucleus itself [48].*

Many efforts have been focused on understanding the mechanism of texture formation in OAD films. As reported by Chudzik et al. [49] for depositions under oblique angles, the (002) plane rotates toward the vapor flux and the MgO [111] direction rotates away from the vapor direction and substrate normal as well. As illustrated in Fig. 2.6, the MgO crystal habit is in fact cubic with (002) as its tile surface plane, indicating that the competition of (002) and (111) growth makes MgO columns prefer to grow with the [11n] direction perpendicular to the substrate surface while maintaining a minimization of surface free energy by maximizing the (002) surface area off the substrate normal. Accordingly, the higher packing density in this plane and the lower surface free energy drive the formation of (002) crystal facets that grow at an angle (β) to the substrate normal.

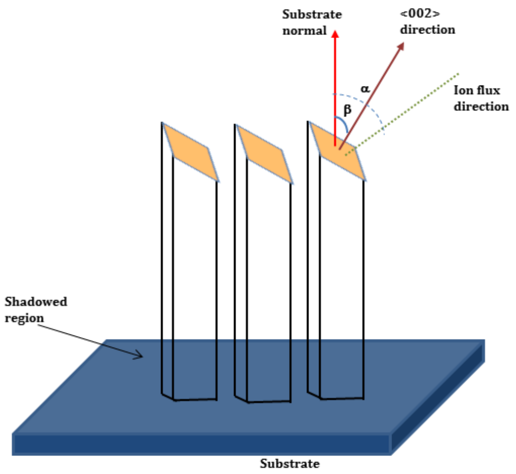

Fig. 2.6: *Schematic diagram of vapor and columnar growth directions for MgO deposited under oblique angles. The <002> directions rotate to face the vapor direction and not the (111) face. The <111> direction rotates to grow away from the vapor when the substrate is inclined [49].*

In a recent study, Deniz and Harper have shown that the TiN responds to the incident flux direction by developing a biaxial texture aligning its <100> crystallographic axis with the deposition direction and its <111> axis with the substrate normal. They explained this texture tilt by the low adatom mobilities of materials with high melting points, hence, high vertical growth rates of grains with different orientations and shadowing effects [41]. As for in-plane alignments, if there were a competition among the grains due to geometrical restrictions and mobility differences on different grains, then certain orientations would be favored at the expense of others. Adatom mobility differences cause the grains to have different vertical growth rates. As one orientation grows taller, it wins the competition and stops further growth of the other orientations due to shadowing effects [41]. One would normally expect the surface diffusion to be fastest on <002> and slowest on <111> planes of TiN due to the activation energy differences for diffusion on these planes [50]. However, surface diffusion rates might be strongly affected by the energy and flux of ion irradiation, the flux of atomic N, and N_2 partial pressure because these parameters will control the steady state nitrogen coverage [51,52]. Fig. 2.7 depicts the formation of a biaxial texture in TiN structure. They concluded that (002) planes of TiN win the competition among the TiN planes and respond to the deposition direction due to low adatom mobilities on these surfaces and shadowing effects as illustrated in Fig. 2.7. Then as the film thickens, the symmetry of the fcc B1-NaCl structure brings (111) planes almost parallel to the substrate surface as revealed in the figure, leading to the formation of a biaxial texture. The (111) TiN planes are tilted away from the ion direction as illustrated. They concluded that the lowering the surface mobilities, i.e., allowing kinetic effects to dominate, has an important role in forming the biaxial texture of the films as well as crystal habits in highly symmetric structures [41].

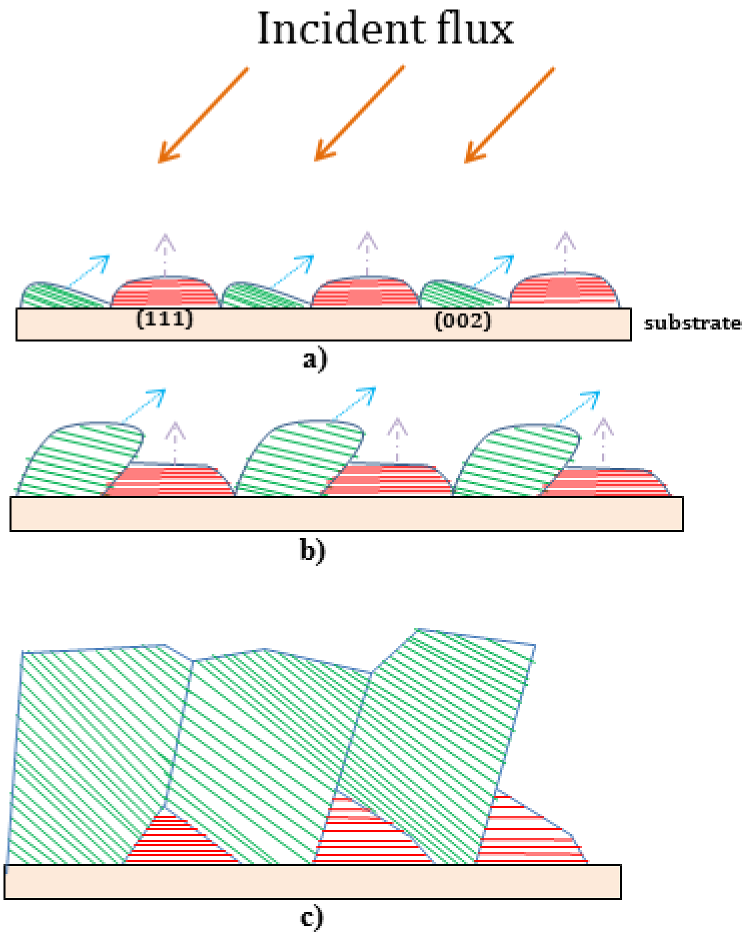

Fig. 2.7: *Sketch of biaxial texture evolution: a) early stages of the film growth, b) competition due to vertical growth rate differences and shadowing effects, and c) (002) planes win the competition along in-plane direction, red lines indicate TiN (111) planes corresponding to tilted (002) planes [41].*

Mahieu et al. [44] deposited TiN layer on a tilted substrate which revealed a zone T structure, with columns having an inclination towards the flux. The tilt angle of the (111) orientation and the tilt angle of the columns were not the same (tilted in the opposite direction). They concluded that the tilting the substrate with respect to the material flux mainly influences the microstructural and crystallographic in-plane alignment.

Mahieu et al. argued that this in-plane alignment is caused by an overgrowth mechanism in which the [111] out-of-plane oriented grains with a good in-plane alignment overgrow the other [111] out-of-plane oriented grains. This is based on anisotropy in growth rate caused by the shape of the grains. These grains grow mainly according to a specific crystal habit. A sketch of this specific crystal habit is drawn in Fig. 2.8. Evidently, the grains are terminated by planes of lowest energy ({001} planes). It can be calculated that the grains with a {001} plane facing the material flux will grow faster perpendicular to the substrate than the other in-plane oriented grains, because they catch more metallic adatoms. As such, the microstructural and crystallographic in-plane alignment are correlated due to the fact that both in-plane alignments are a direct consequence of the fact that all grains in zone T grow according to a specific crystal habit.

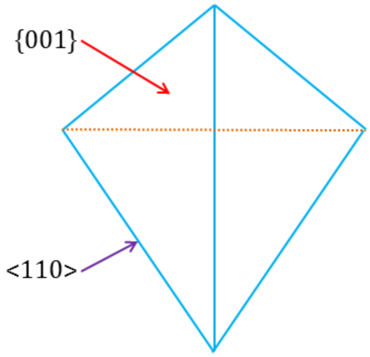

Fig. 2.8: *Sketch of the observed TiN crystal habit [44].*

2.4 Structure evolution of biaxially-textured films

It is well known that oblique angle deposition (OAD) results in tilting of columnar films, where the formation of the inclined columns is mainly governed by the self-shadowing effect. During OAD, the film already present on the substrate prevents any further film growth in the shadowed region. By restricting where incident atoms can bond to the substrate, the shadowing effect ensures that incident atoms will join with nuclei already formed on the surface. In fact, the incident atoms are more likely to hit the nuclei on the side facing the vapor source. Under oblique angle conditions, these nuclei will continue to grow in a slanted fashion; eventually, a series of slanted columns will emerge. This is an indication of film microstructure control through OAD [53].

The influence of several deposition parameters on the final film structure and morphology has been depicted in terms of structure zone models (SZM's) by many authors [54,55]. The SZM best known in sputter deposition community is the one published by Thornton [56], which shows microstructure and morphology as a function of deposition pressure and substrate temperature. Since the SZM classify films according to their microstructure, which is strongly influenced by the surface mobility or the temperature on the growing surface, they are often represented as a function of the homologous temperature T, i.e. the ratio between the substrate temperature T_s and the melting temperature of the deposited material T_m.

2.5 Extended structure zone model (ESZM)

Recently, Mahieu et al. [57], published an extended structure zone model (ESZM) which has the advantage that it not only summarizes the influence of deposition parameters on film microstructure, but also provides insight into sputter-deposited thin film growth. Hence film structure (microstructure and crystallographic orientation) is plotted as a function of adatom mobility. In this section, we will discuss ESZM.

2.5.1 Zone 1a

In zone Ia, the adatom diffusion is negligible. The adatom energy is too low to overcome the surface diffusion barriers. Consequently, arriving adatoms stick at the site of impingement. This is also called the hit-and-stick regime. This structure can be described by a ballistic model [57]. As simulated by Müller [58] and Leamy and Dirks [59], a columnar structure separated by voids will develop, mainly caused by statistical roughening and self-shadowing (see Fig. 2.9a). Because of the voided structure, the density of the deposited film is much smaller than the density of the bulk material.

At oblique incidence, the columns are tilted towards the in-coming material flux (Fig. 2.9b). The relation between the angle of incidence α and the columnar inclination angle β is given by the tangent rule: tan (β) = 1/2 tan (α) [45].

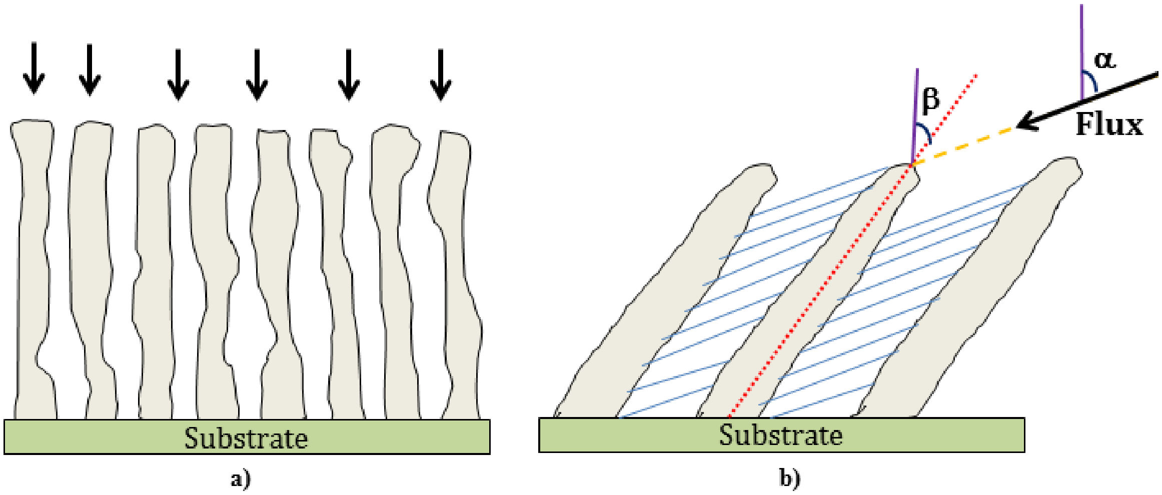

Fig. 2.9: a) Schematic drawing of the resulting structure of a film grown under zone Ia conditions. A voided structure, with the columns consisting of small grains develops. b) View of film growth at very low temperature (zone I) on an inclined substrate. The inclination of the substrate with respect to the material flux is given by α and the inclination of the columns by β. The dashed lines are the shadowed region [57].

2.5.2 Zone T

By increasing the energy of the incoming adatom or by increasing its energy thermally, adatoms will be able to overcome the surface diffusion barriers and will diffuse on the surface (Fig. 2.10). Since the mobility is high enough, the grains will again grow according to their kinetically determined crystal habit and faceting will be observed, in which again the planes of lowest perpendicular growth rate will form the resulting facets. Since no recrystallization or restructuring can happen, the competitive growth of neighbouring grains should occur in an evolutionary way.

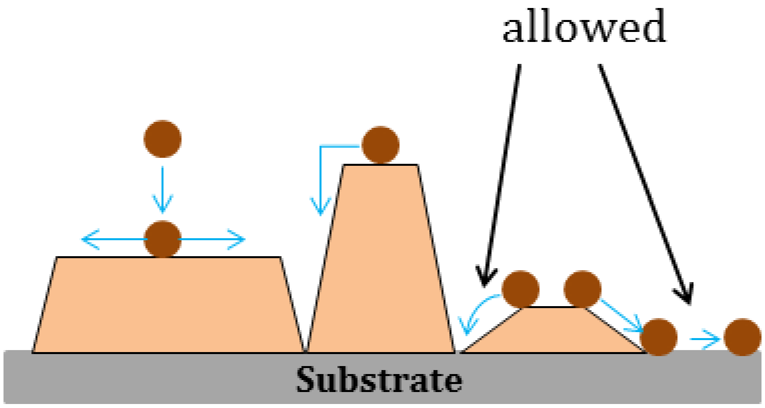

Fig. 2.10: *Schematic representation of the diffusion processes occurring in zone T conditions where the adparticles are able to diffuse from one grain to another [57].*

Initially, nucleation of crystalline islands on the substrate occurs. These islands have a random orientation distribution. As the adatoms are able to diffuse on the island, the island will grow according to the kinetically determined growth shape. As a result the substrate will be covered by grains which have all the same crystal habit but which have a different crystallographic orientation. The grains grow by the capture of diffusing adatoms or by the capture directly from the vapour flux. Growth on the crystal facets continues by local epitaxy because self-diffusion is considerable [60]. At the point of impingement, a grain boundary is formed. Because the activation energy for restructurative grain growth is too high in comparison to the adatom energy, the grain boundary is immobile throughout the complete film thickness. Although all facets have a similar growth rate, some grains will have a higher perpendicular growth rate with respect to the substrate. As can be seen in Fig. 2.11a, grains of which the facets have the highest tilt angle with respect to the substrate, will have the highest perpendicular growth rate and will overgrow the others. As a result, a preferential out-of-plane orientation evolves. The anisotropy in perpendicular growth rate is characteristic for zone T growth. The survival of the fastest is also referred to as evolutionary selection [34] and is illustrated in Fig. 2.11b.

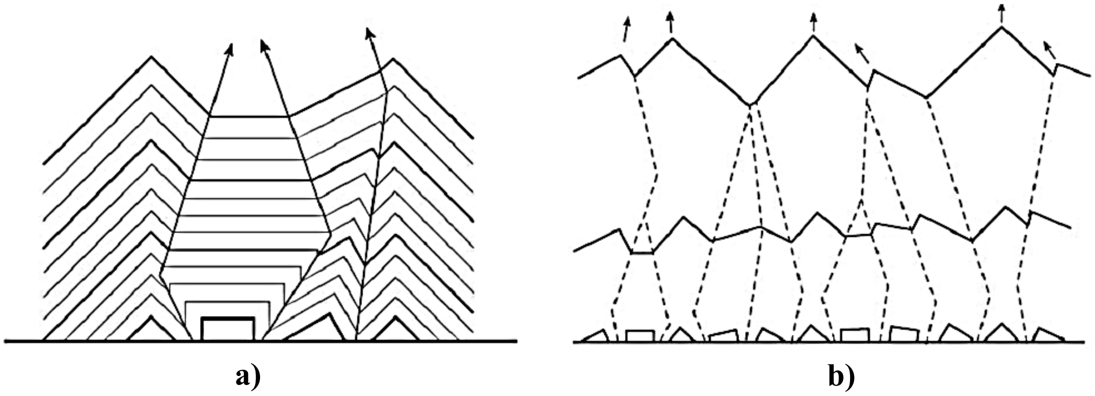

Fig. 2.11: *(a) Overgrowth mechanism of different oriented grains truncated by planes with lowest normal growth rate, (b) van der Drift construction for zone T growth, illustrating the V-shaped columnar growth [61].*

The out-of-plane alignment is completed at a certain film thickness. At higher film thickness, a columnar structure with faceted tops develops (Fig. 2.12) [62].

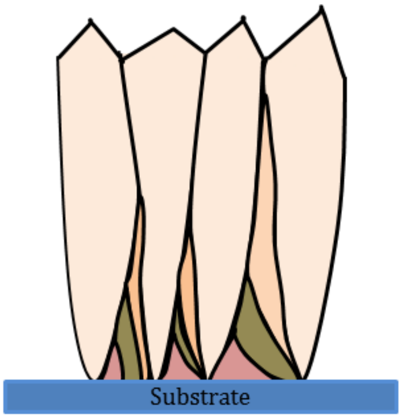

Fig. 2.12: *Schematic drawing of a zone T structure, characterized by V-shaped and faceted columns.*

If there is oblique material incidence, also V-shaped columns are observed. However, in contrast with zone I, the tilt angle of the columns does not obey the tangent rule because the adatoms are able to diffuse. Through this, the columns will be less tilted towards the flux.

2.5.3 Zone II

Up to zone T temperatures, atoms are immobile as soon as they are incorporated into the growing film. However, when further increasing the temperature *T*, already chemisorbed and thus stable atoms can become active, meaning that recrystallization or restructuring will happen. More exactly, former stable nuclei or islands can become unstable and get incorporated into other islands by ripening, cluster diffusion, or grain boundary migration. Since the unstable islands are dissolved in more stable islands, no evolutionary V-shaped overgrowth will be observed in the resulting film. A columnar structure with approximately straight columns throughout the whole film thickness will be formed, as shown in Fig. 2.13.

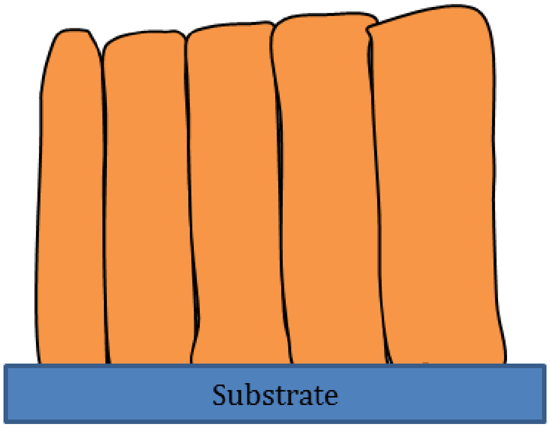

Fig. 2.13: *Typical microstructure of a zone II film.*

Generally, the whole film will aim for its thermodynamic most stable situation, causing all columns to be oriented with the plane of lowest surface energy parallel to the substrate. Due to rapid surface diffusion and the appearance of recrystallization, shadowing will have a minor influence on growth. Hence, tilting the substrate with respect to the incoming material flux will not cause an inclination of the columns ($\beta = 0°$). Further increasing the temperature increases the effect of recrystallization and restructuring, thus increasing the lateral size of the resulting columns. However, in this work, films which exhibit a zone II structure are not observed.

2.6 Aim of the thesis

Early works on texture change with film thickness were mainly focused over relatively thin films (less than 1.5 μm) for which the most commonly observed textures were reported to begin with (002) orientation and end with (111) with film thickness. To get a more complete picture on texture evolution with film thickness, we have extended this range in our study and investigated growth mechanism between thicknesses ranging from 100 nm to 6 μm. In addition, we used X-ray diffraction (XRD) with pole figure and θ–2θ geometries to provide better picture of texture change and a comparison with literature data based mostly on θ–2θ measurements. Scanning electron microscope (SEM), transmission electron microscope (TEM), and nanoindentation were used to explore the effect of film thickness on microstructural and mechanical properties of the films. Our aim is to provide fundamental knowledge in thin film growth and texture development, and to bring clarity to the texture controversies mentioned above. The objective is to show texture evolution with film thickness.

Furthermore, in this thesis, to explore the effects of deposition angle on the texture growth mechanism of thin films, $Ti_{1-x}Al_xN$ films were deposited by pulsed DC magnetron sputtering by changing incident angle of the sputtered particles from 0° (normal to substrate) to 60° systematically. Precise observations of the polycrystalline structure were carried out by X-ray diffraction (XRD) Bragg–Brentano θ–2θ configuration and, more systematically, by analyzing the pole figures. The film microstructures were studied by scanning electron microscopy (SEM) and transmission electron microscopy (TEM). The various columnar structures and their crystallographic orientations were investigated in detail. In this thesis, we explain the texture tilt by a combination of shadowing effect and competitive growth between grains of different orientations.

2.7 Reference

[1] C.V. Falub, A. Karimi, M. Ante, W. Kalss, Surf. Coat. Technol. 201 (2007) 5891.

[2] J. Pelleg, L.Z. Zevin, S. Lungo, N. Croitoru, Thin Solid Films 197 (1991) 117.

[3] U.C. Oh, J.H. Je, J. Appl. Phys. 74 (1993) 1692.

[4] J.P. Zhao, X. Wang, Z.Y. Chen, S.Q. Yang, T.S. Shi, X.H. Liu, J. Phys. D 30 (1997) 5.

[5] G. Knuyt, C. Quaeyhaegens, J. D'Haen, L.M. Stals, Surf. Coat. Technol. 76 (1995) 311.

[6] J.E. Greene, J.E. Sundgren, L. Hultman, I. Petrov, D.B. Bergstr, Appl. Phys. Lett. 67 (1995) 2928.

[7] A. R. Shetty, A. Karimi, Appl. Surf. Sci. 258 (2012) 1630.

[8] C. H. Ma, J. H. Huang, H. Chen, Thin Solid Films 446 (2004) 184.

[9] Y. M. Chen, G. P. Yu, J. H. Huang, Vacuum 66 (2002) 19.

[10] Y. H. Cheng, B. K. Tay, S. P. Lau, J. Vac. Sci. Technol. A 20 (2002) 1327.

[11] Y. H. Cheng, B. K. Tay, J. Cryst. Growth 252 (2003) 257.

[12] N. Schell, W. Matz, J. Bottiger, J. Chevallier, P. Kringhoj, J. Appl. Phys. 91 (2002) 2037.

[13] M. Kobayashi, Y. Doi, Thin Solid Films 54 (1978) 67.

[14] U. C. Oh, J. H. Je, and J. Y. Lee, J. Mater. Res. 13 (1998) 1225.

[15] P. Patsalas, C. Charitidis, S. Logothetidis, Surf. Coat. Technol. 125 (2000) 335.

[16] P. Patsalas, C. Gravalidis, S. Logothetidis, J. Appl. Phys. 96 (2004) 6234.

[17] T. Q. Li, S. Noda, Y. Tsuji, T. Ohsawa, H. Komiyama, J. Vac. Sci. Technol. A 20 (2002) 583.

[18] J. H. Je, D. Y. Noh, H. K. Kim, K. S. Liang, J. Appl. Phys. 81 (1997) 6126.

[19] R. Banerjee, R. Chandra, P. Ayyub, Thin Solid Films 405,64 2002.

[20] J. S. Chun, I. Petrov, J. E. Greene, J. Appl. Phys. 86 (1999) 3633.

[21] L. Hultman, J. E. Sundgren, J. E. Greene, D. B. Bergstrom, I. Petrov J. Appl. Phys. 78 (1995) 395.

[21] A. Bendavid, P. J. Martin, X. Wang, M. Wittling, T. J. Kinder, J. Vac. Sci. Technol. A 13 (1995) 1658.

[22] B. Rauschenbach, J. W. Gerlach, Cryst. Res. Technol. 35 (2000) 675.

[23] G. Q. Yu, B. K. Tay, S. P. Lau, K. Prasad, L. K. Pan, J. W. Chai, D. Lai, Chem. Phys. Lett. 374 (2003) 264.

[24] J. E. Sundgren, Thin Solid Films 128 (1985) 21.

[25] A. J. Perry, J. Vac. Sci. Technol. A 8 (1990) 1351.

[26] H. Windischmann, Crit. Rev. Solid State Mater. Sci. 17 (1992) 547.

[27] S. Mahieu, D. Depla, J. Phys. D: Appl. Phys. 42 (2009) 053002.

[28] G. Abadias, Y.Y. Tse, Ph. Guérin, V. Pelosin, J. Appl. Phys. 99 (2006) 113519.

[29] G. Abadias, Y.Y. Tse, J. Appl. Phys. 95 (2004) 2414.

[30] I. Petrov, L. Hultman, J. E. Sundgren, J. E. Greene, J. Vac. Sci. Technol. A 10 (1992) 265.

[31] I. Iordanova, P. J. Kelly, R. Mirchev, V. Antonov, Vacuum 81 (2007) 830.

[32] L. Hultman, J. E. Sundgren, J. E. Greene, D. B. Bergstrom, I. Petrov, J. Appl. Phys. 78 (1995) 5395.

[33] T. Q. Li, S. Noda, Y. Tsuji, T. Ohsawa, H. Komiyama, J. Vac. Sci. Technol. A 20 (2002) 583.

[34] A. van der Drift, Philips Res. Pep. 22 (1967) 267.

[35] V. Neto, PhD thesis, Universidade de Aveiro (2004),

[36] J. Thornton, Ann. Rev. Mater. Sci. 7 (1977) 239.

[37] G. Knuyt, C. Quaeyhaegens, J. D’Haen, L. M. Stals, Thin Solid Films 258 (1995) 159.

[38] G. Knuyt, C. Quaeyhaegens, J. D’Haen, L. M. Stals, Surf. Coat. Technol. 76-77 (1995) 311.

[39] G. Knuyt, C. Quaeyhaegens, J. D'Haen, L. M Stals, Phys. Stat. Sol. (b) 195 (1996) 179.

[40] R. W. Smith, J. Appl. Phy. 81 (1996) 1196.

[41] D. Deniz, J. M. E. Harper, J. Appl. Phys. 104 (2008) 063519.

[42] A.R. Shetty, A. Karimi, M. Cantoni, Thin Solid Films 519 (2011) 4262.

[43] A.R. Shetty, A. Karimi, Phys. Stat. Sol (b) 249 (2012) 1531.

[44] S. Mahieu, P. Ghekiere, G. De Winter, R. De Gryse, D. Depla, G. Van Tendeloo, O. I. Lebedev, Surf. Coat. Technol. 200 (2006) 2764.

[45] J. M. Nieuwenhuizen, H. B. Haanstra, Philips Tech. Rev. 27 (1996) 87.

[46] A. G. Dirks, H. J. Leamy, Thin Solid Films 47 (1977) 219.

[47] Y. E. Lee, S. G. Kim, Y. J. Kim, H. J. Kim, J. Vac. Sci. Technol. A 15 (1997) 1194.

[48] F. H. Cocks, M. J. Peterson, P. L. Jones, Thin Solid Films 70 (1980) 297.

[49] M. P. Chudzik, R. E. Koritala, L. P. Luo, D. J. Miller, U. Balachandran, IEEE Trans. Appl. Supercond. 11 (2001) 3469.

[50] D. Gall, S. Kodambaka, M. A. Wall, I. Petrov, J. E. Greene, J. Appl. Phys. 93 (2003) 9086.

[51] M. A. Wall, D. G. Cahill, I. Petrov, D. Gall, J. E. Greene, Phys. Rev. B 70 (2004) 035413.

[52] M. A. Wall, D. G. Cahill, I. Petrov, D. Gall, J. E. Greene, Surf. Sci. 581 (2005) L122.

[53] L.-C. Chen, C.-C. Chen, Y.-T. Sung, Y.-Y. Hsu, J. Electrochem. Soc. 156 (2009) H471.

[54] B. A. Movchan, A. V. Demchishin, Phys. Met. Metallogr. 28 (1969) 83.

[55] R. Messier, A.P. Giri, R.A. Roy, J. Vac. Sci. Technol., A 2 (1984) 500.

[56] J. A. Thornton, J. Vac. Sci. Technol. 4 (1974) 666.

[57] S. Mahieu, P. Ghekiere, D. Depla, R. De Gryse, Thin Solid Films, 515 (2006) 1229.

[58] K. H. Müller, J. Appl. Phys. 58 (1985) 2573.

[59] H. J. Leamy, A. G. Dirks, J. Appl. Phys. 49 (1978) 3430.

[60] J. A. Stroscio, D. T. Pierce, R. A. Dragoset, Phys. Rev. Lett. 70 (1993) 3615.

[61] P. Ghekiere, PhD thesis, Ghent University.

[62] S. Mahieu, PhD thesis, Ghent University.

Chapter 3:

Experimental setup and characterization methods

Before presenting the experimental results in the forthcoming chapters, we will review the practical techniques used to prepare and characterize the thin film samples. Basic principles of the characterization techniques, their resolution and the accuracy of each measure are also reported. The experimental methods are presented according to the properties they study: crystallographic (phase, texture, residual stress), structure and morphology, as well as the mechanical properties. All experimental procedures were aimed at minimizing the exposure of the film to contaminants, which can segregate to the film surface, interface, and grain boundaries, and influence grain growth.

3.1 Deposition of films by pulsed DC magnetron sputtering

3.1.1 Principle of magnetron sputtering

The sputtering process consists in the extraction of materials particles from a target which is bombarded with high energetic particles of inert gas, generally argon (Fig. 3.1). The pressure of inert gas in the chamber is between 10^{-1} and 10^{+1} Pa [1]. The expulsed atoms or ions condense and react on the surface of the substrates. In magnetron sputtering, a magnetic field in front of the target causes an extended path length for plasma electrons. This induces an increase in the sputtering as ionization and leads to higher deposition rate. The applied magnetic field parallel to the cathode concentrates the electrons near the target, minimizing the loss of energy. They collide mostly with gas atoms, hence the ionization efficiency is increased. The increased ion density results in higher ion current and higher sputtering rate. The magnetic field has a low strength, and thus it only influences the electrons but not the ions [2].

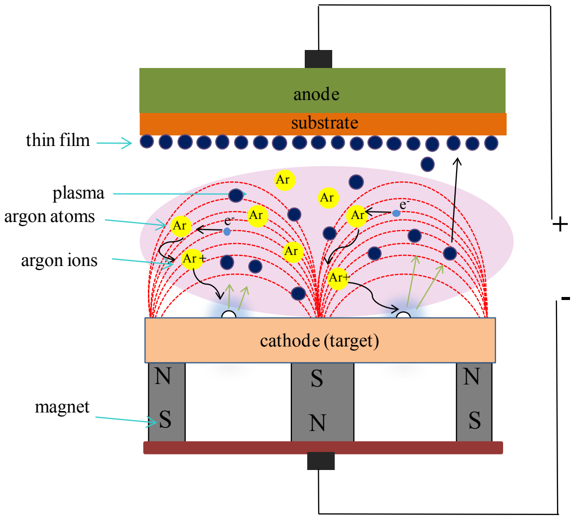

Fig. 3.1: *The basic components of magnetron system. Ionized argon bombards a target, releasing atoms which form layers on a substrate. Electrons and argon ions form plasma, which is located near the target due to magnetic field, resulting in greater efficiency and quality.*

If sputtering is done in atmosphere of inert gas (e.g. Ar) plus reactive gas (e.g. N_2, O_2) the method is called reactive sputtering. Deposition of metal nitrides films is often carried out by reactive magnetron sputtering (RMS). In the present work, RMS was used for the deposition of the $Ti_{1-x}Al_xN$ thin films.

3.1.2 Pulsed DC magnetron sputtering

In a direct current (DC) magnetron sputter deposition process, the cathode potential is always negative. During the deposition of dielectrics, all inside surfaces of the deposition chamber are eventually coated with non-conductive layers, on which electrical charges will accumulate. These charges create arcs, resulting in a highly non-uniform removal of material from the anode and in the formation of particulates. The presence of particles and their ultimate incorporation into the deposited films usually severely limits the use of such thin films in many practical applications [3]. In addition, arcing may damage the power supply. Pulsed modulation of the DC magnetron plasma solves most of the arcing problems as discussed in the literature [4].

Pulsed DC unbalanced magnetron sputtering is a well-developed deposition technique for coatings and is widely used in industry to deposit thin films [5]. Thin films deposited using pulsed DC reactive sputtering have a smooth surface structure as observed in cross-section SEM studies due to the absence of particles created by micro-arcs [6]. A typical pulsed power train used for pulsed DC reactive sputtering with a single magnetron is displayed in Fig. 3.2.

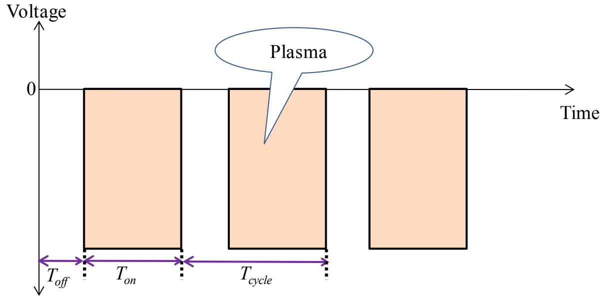

Fig. 3.2: *Schematic diagram of the pulsed DC voltage applied to a magnetron, depicting* T_{off}, T_{on}, *and* T_{cycle}. *The sputtering takes place during the* T_{on} *period. The voltage applied during off-time is either zero or slightly positive.*

A high negative voltage pulse of a few hundred volts is applied to the target during the 'on-time', T_{on}, for periods of microseconds to tens of microseconds. A short 'off-time', T_{off}, which is typically 1/5– 1/10 of the duration of T_{on}, separates subsequent negative pulses. The applied voltage during the off-time is either zero or slightly positive (up to approximately 20–50 V). Therefore, the off-time is often labeled ‘reverse time’, T_{off}. During the on-time, sputtering takes place and the surfaces are gradually charging up. To avoid arcing, the optimum pulsing frequency and reverse time are routinely determined empirically and are optimized for a particular application and magnetron device. Two requirements must be met: (i) the on-time must be sufficiently short to prevent arc formation due to the charge accumulation in a single on-time period and (ii) the duration of the reverse pulse must be sufficiently long, so that the surfaces can be fully discharged prior to re-establishing the plasma in order to avoid charge accumulation during sequential ‘on’ and ‘off’ cycles. The sum of the longest on-time and the shortest off-time also determines the lowest pulse repetition frequency ($f = 1/T_{cycle}$, where T_{cycle} is the sum of T_{on} and T_{off}) which is often referred to as the critical frequency, f_c, at which pulsed DC reactive sputtering can be accomplished arc free. From a practical point of view, the deposition rate in magnetron sputtering is linearly proportional to the power deposited into the plasma and (almost) linearly proportional to the duty cycle, which is defined as the ratio T_{on} / T_{cycle} in the frequency range from about 2 to 250 kHz [3].

3.2 Thin film preparation

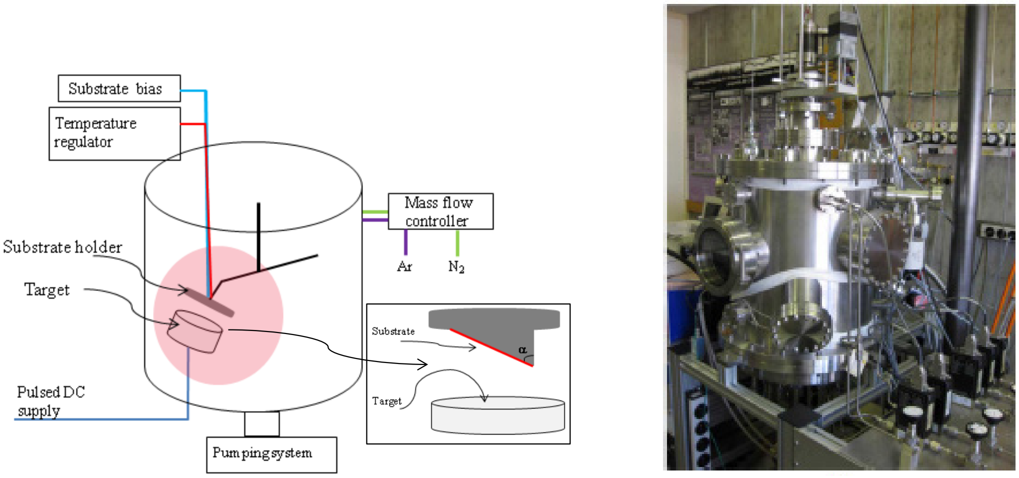

(a) **(b)**

Fig. 3.3: *a) Schematic description of the sputtering apparatus used for the film deposition. The angles of inclination of the incident sputtered particles were from* $\alpha = 0°$ *(normal incidence), 30°, 45° and 60°, which were adjusted by the angles of the substrate that was mounted on a specially-designed sample holder (Inset). b) Image of the pulsed DC magnetron sputtering system in our laboratory.*

The TiAlN films were deposited using pulsed DC (pulsation frequency f = 100 kHz, T_{off} = 2 μs) magnetron sputtering system as featured in Fig. 3.3. The sputtering process is conducted in a reactor, which had been pumped down by a turbomolecular pump coupled with a rotary pump to a pressure of 3×10^{-3} Pa before the gas mixture was introduced. To obtain high quality TiAlN films, we adjusted several deposition parameters such as N_2/Ar gas pressure, target-substrate distance, pulsed DC power and flow rate. Then the optimum conditions were chosen for the preparation of TiAlN films. The following parameters were fixed throughout this thesis. The substrate-to-target distance was fixed at 60 mm. The flow rates (sccm) of Ar and N_2 gases were kept to 14 and 6, respectively by mass flow controller (the partial pressures were 0.14 Pa for N_2 and 0.28 Pa for Ar). The working pressure and DC input power were kept at 4.2×10^{-1} Pa and 150 W, respectively. A thermocouple was fixed at the backside of the substrate, and the required temperature was obtained by adjusting the current and voltage. The thickness of all the films was measured by Tencor alpha-step 500 profilometer.

3.3 Oblique angle deposition setup

Thin films usually have one of the crystallographic axes in the out-of-plane direction and no in-plane alignment. In this case, the preferred orientation is known as fiber texture. If the adatoms landing on the surface have enough surface mobility, then they have a chance to reach minimum energy sites before they are buried by the following layers [7]. Therefore, adatom mobility is a crucial parameter determining the out-of-plane texture. The control of crystallographic orientation and microstructure is desirable, since the final properties of the film are strongly dependent on the orientation of crystal grain and texture. However, the mechanisms of controlling texture formation are generally not well understood. In this thesis, it is shown that by varying the range of impingement of particles of the flux, the degree of preferred orientation of TiAlN can be controlled.

Depending on the growth conditions, TiAlN can respond to the incident atoms by tilting its growth axis towards or away from the deposition direction [8]. In this thesis, we have showed that the fiber axis of a growing film is tilted in oblique angle deposition (OAD) conditions under the circumstances of low adatom mobility [9]. We notice that as the adatom mobility decreases, the fiber axis response to the deposition direction increases. Films deposited under OAD induce an alignment along the crystallographic direction. The as obtained films are known to possess biaxial texture that have both out-of-plane and in-plane alignments and hence may become close to single crystalline materials. In order to grow biaxially aligned layers, one has to either change the energetics of the incoming flux of a regular sputtering environment or include directional effects during sputtering; the former can be achieved using ion beam assisted deposition (IBAD) technique by adjusting the incidence angle and energy of the incident ion flux, and the latter is usually done by off-normal incidence deposition or OAD.

Films deposited under OAD not only modify texture but also the microstructure. When thin films are deposited onto stationary substrates with the flux arriving at a non-normal angle α under conditions of limited adatom diffusion, an inclined columnar microstructure β is produced (Fig. 3.4). The column inclination angle β lies between the film normal and the vapor incidence angle α and is dependent upon many factors including material and deposition conditions such as substrate and film temperature, angular distribution of the deposition flux, background gas pressure and composition, and flux energetics. However, it is observed experimentally that there is a relationship between the flux angle α and the column angle β for a given set of deposition conditions; the column angle β is uniquely determined by the choice of the deposition angle α. In such a type of growth, due to the self-shadowing effect, the porosity of the film increases with increasing deposition angle that results in large voided surface compared to normally deposited films.

The experimental setup for oblique angle deposition used in my thesis is very simple and displayed in Fig. 3.5a. The incident flux arrives at an angle α with respect to the substrate surface normal. The angles of inclination of the incident sputtered particles were from α = 0° (normal incidence, Fig. 3.5b), 30°, 45°, and 60°, which were adjusted by the angles of the substrate that was mounted on a specially-designed sample holder.

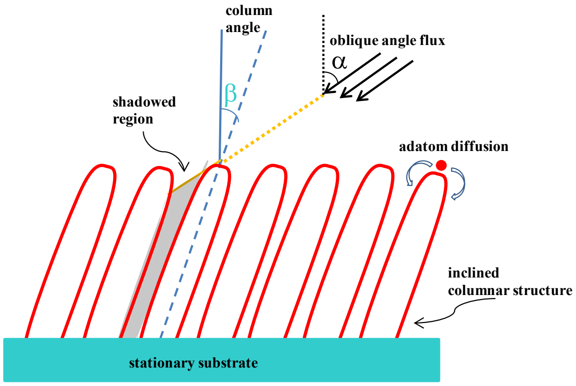

Fig. 3.4: *Schematic of deposition vapor flux and film orientation with angle definitions.* α *is the flux arrival angle measured from the substrate normal and* β *is the columnar microstructure inclination angle also measured from the substrate normal.*

The relationship between α and β is complex and poorly understood, although a number of attempts at understanding and quantifying this relationship have been presented. The empirical tangent rule [10], $\tan\beta = (1/2)\tan\alpha$ is a simple relationship based on near normal deposition and gives very poor results for α greater than about 50°. A relationship by Tait et al. [11] based on geometrical analysis $\beta = \alpha - \sin^{-1}[(1 - \cos\alpha) / 2]$ gives much better results for highly oblique angles (α large). Clearly, thin films deposited by oblique angle deposition have the following characteristics: the films are in general porous, possessing nanocolumnar structures. The nanocolumns are tilting away from the surface normal to the incident evaporation beam direction (Fig. 3.5a). The size and density of the nanocolumns change as function of the incident angle α.

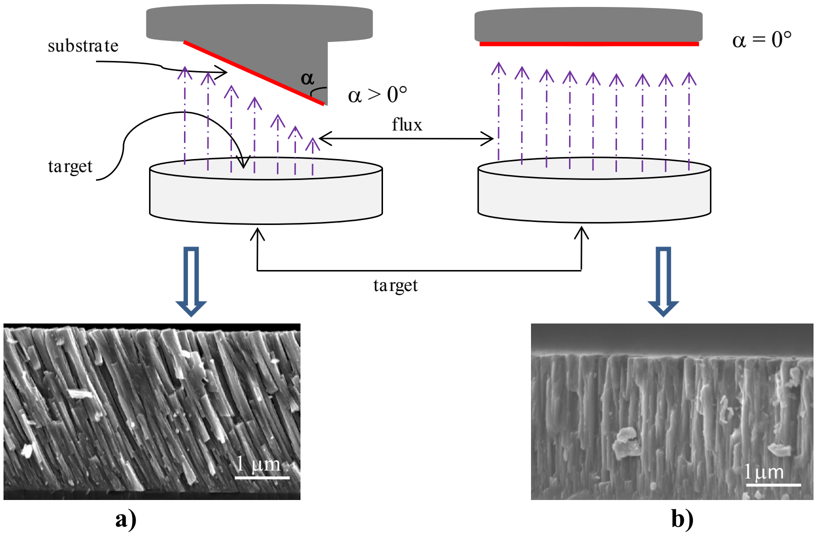

Fig. 3.5: *Experimental setup for (a) oblique angle deposition and (b) normal incidence deposition. Films deposited under oblique angle flux result in inclined columns towards the deposition source. No such tilting of columns was observed for films deposited under* $\alpha = 0°$.

3.4 Brief description of samples used in the study

The target compositions (Ti/Al) used for film depositions were 67/33, 60/40, and 50/50 (at. %). The dimensions of the target were 50.8 mm in diameter and 3.1 mm thick. Depositions were done on different types of substrates including single crystalline Si(100) wafers, amorphous glass and polycrystalline WC-Co for various texture studies. Prior to the insertion into the deposition chamber, the substrates were ultrasonically cleaned in acetone, alcohol and then dried with N_2 gas. The Si substrates were etched in HF solution (10%) to remove the native oxide. To study of effect of film thickness on the texture growth, the thickness was varied from about 100 nm to 5.8 µm. On the other hand, film thickness was kept around 2 µm to avoid any thickness-related effect on the formation of biaxial texture under oblique angle deposition. In order to understand the significance of deposition parameters on the inclination of columns and biaxial texture, the substrate temperature was kept at room temperature (RT), 400°C and 650°C. In addition to this, the bias (substrate grounded) was varied from 0 to -80V.

3.5 Characterization methods

To study thin film growth and processes involved in the building blocks of the film such as texture, we must know the state that the film is in. We need to know the phase(s), preferential orientation, the microstructure, and eventual nanostructure, and so on. This understanding is gleaned from the combination of several characterization techniques, as a single technique seldom gives the whole picture needed. In this chapter, the main characterization techniques used during this thesis are presented in Table 3.1.

Film property	**Characterization techniques**
Phase formation, texture, crystallite size, residual stress	X-ray diffraction (θ–2θ scans, texture by pole figures, residual stress by $\sin^2\psi$)
Microstructure, morphology, lattice defects	Transmission electron microscope, (TEM), scanning electron microscopy (SEM), atomic force microscopy (AFM)
Hardness and elastic modulus	Nanoindentation

Table 3.1: *Characterization techniques used for the evaluation of texture, coating morphology, microstructure, and mechanical properties.*

3.6 X-ray diffraction

In the course of this work, films were investigated with various X-ray techniques to conclude on the crystallographic features. The primary characterization technique used was X-ray texture analysis. The crystallographic phase was determined by using X-ray diffraction (XRD) at Bragg-Brentano (θ–2θ) configurations in a Rigaku diffractometer (40 kV and 30 mA). The texture of the coatings was characterized using a Seifert diffractometer (3003 PTS-HR) with a four-circle goniometer operating at 40 kV and 40 mA. Some of the pole figure measurements were also performed on PANalytical X'PERT PRO MRD diffractometer (40 kV and 40 mA) in collaboration with Dr. Antonia Neels and Professor Alex Dommann at CSEM, Neuchâtel. All the XRD measurements were performed on CuKα radiation (λ = 1.45 Å). The machines were typically operated with a line focus. In the following, the geometry of the various scans will be discussed with special emphasis on the type of information that can be deduced from each measurement, respectively.

3.6.1 θ–2θ scans

X-ray diffraction in Bragg-Brentano (also called θ-2θ) geometry has typically been utilized to determine the structural quality of sputtered TiAlN films. The basic geometrical features are displayed in Fig. 3.6. The prominent feature is that the incident and diffracted X-ray beams have identical inclinations with respect to the substrate surface (Fig. 3.6). As a consequence, the bisecting line of the angle between these beams (the "scan normal") is fixed and always parallel to the substrate normal. Therefore, only reflections from planes parallel to the substrate surface are detected. Statements about preferred orientation are therefore straightforward. As an example, typically sputter-deposited zinc oxide films reveal only a very pronounced (002) peak and higher orders in a θ-2θ diffraction pattern. This strongly suggests that only crystallites with the respective planes oriented parallel to the substrate surface are present in the film. Thus, there is a (002) preferred orientation. The conditions for a diffraction peak are also sketched in Fig. 3.6. Incoming X-rays are scattered at the electron shells of atoms which in a crystalline structure are regularly arranged along planes with inter-planar distance d_{hkl}. The relative phase retardation δ between X-rays scattered at adjacent planes is given by $\delta = 2d_{hkl}\sin\theta$. Constructive interference and therefore an intensity maximum at the detector requires that $\delta = n\lambda$, where λ is the wavelength of the utilized radiation and n is an integer value (n = 1, 2, 3, ...). This results in Bragg's law:

$$2\,d_{hkl}\sin\theta = n\,\lambda \qquad (3.1)$$

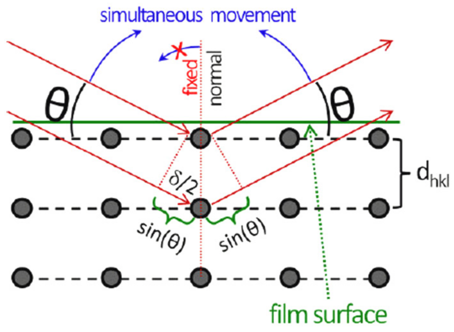

Fig. 3.6: *Geometry of XRD measurements in Bragg-Brentano geometry. Since the intersecting line (scan normal) between the incident and diffracted beams is always perpendicular to the sample surface, only diffraction peaks from planes oriented parallel to the surface contribute to the signal intensity [12].*

3.6.2 Grain size

Scherrer's formula:

In this work, Scherrer's formula was used to determine the average grain size diameter using θ-2θ XRD scans. The Scherrer equation is based upon the broadening effect of the X-ray intensity peak, due to the finite size of crystalline grains.

$$D = \frac{K\lambda}{\beta cos\theta} \tag{3.2}$$

Here β is the integral breadth and K a constant which depends on the crystallites shape (0.9 value is used in this work). Even if this method does not take into account the contribution of the strain, in the width of the XRD peak, it gives a good estimation of the grain size especially for small crystallite size [13].

Williamson-Hall method:

Besides the grain size, a distribution of residual microstrains in the crystals causes a strongly increasing peak broadening with increasing diffraction angle θ, which leads to an increasing underestimation of the vertical grain size with increasing angle. Therefore, higher diffraction orders are not suitable to give accurate grain size values. The microstrains are introduced into the crystals because of distortions (eg. interstitials and vacancies, dislocations, etc.), promoting local variations of the lattice parameter around its average value. Microstrains can also be caused by yield point anisotropy between grains, which may give rise to peak shift and line broadening if they vary from point to point in the coating. The Williamson-Hall method [13] can be applied to separate the peak broadening due to the averaged grain size and due to the mean square strain, as follows equation 3.3:

$$\beta \frac{cos\theta}{\lambda} = \frac{1}{D} + \frac{4\varepsilon}{\lambda} \sin\theta \tag{3.3}$$

where β is the line broadening (full width at half maximum), ε is the strain and D is the unknown grain size in the direction normal to diffracting planes. A plot of β cosθ/λ vs 2 sinθ/λ, the “Williamson-Hall plot”, is a straight line with a slope of 2ε and an intercept of l/D (Fig. 3.7) [13]. This method for the separation of microstrain and crystallite size depends on the fact that strain is a function of the order of reflection while crystallite size is not. The Williamson-Hall plot can thus be used as a first approximation to assess the relative importance of microstrain and grain-size broadening effects.

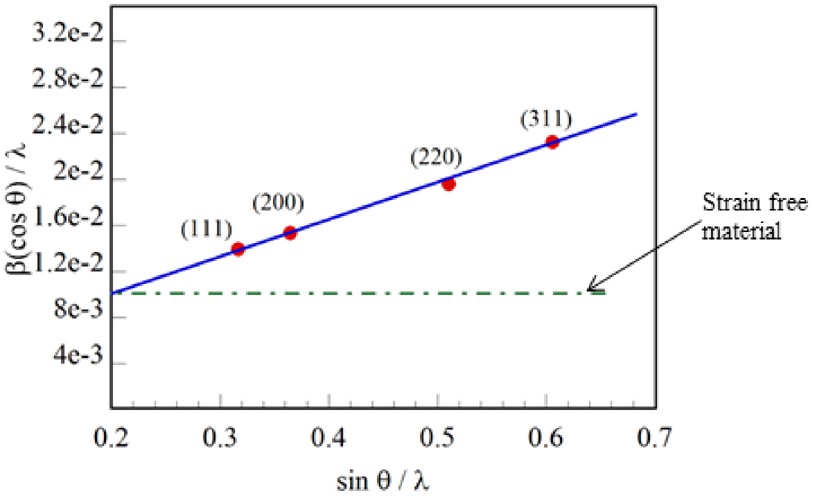

Fig. 3.7: *The Williamson-Hall plot of TiAlN thin film for calculating the crystallite size and lattice strain. The crystallite size is calculated from the intercept and the lattice strain is calculated from the slope of the fitted straight line. The horizontal straight line indicates a strain free material.*

3.6.3 Texture coefficient

To gain a comparative figure on which to base changes in texture from sample to sample, the relative peak heights of all of the (hkl) reflections compared with the random intensity values were used; the experimental intensity values for each (hkl) reflection were determined as peak heights above background. The measurements are made on the Rigaku goniometer. The standard intensity values should ideally be determined for a randomly oriented coating material but this was not possible so the JCPDS values of peak intensity were used as the standard. The form of the equation used is as follows:

$$T^{*}_{hkl} = \frac{I_{hkl} / I^{o}_{hkl}}{\left(\frac{1}{n}\right) \sum_{0}^{n} I_{hkl} / I^{o}_{hkl}} \tag{3.4}$$

where T^*_{hkl} is the so-called texture coefficient of the reflection (*hkl*), I_{hkl} is the measured peak intensity for the reflection (*hkl*), n is the number of diffraction reflections. The lattice planes considered for texture coefficient calculations were (111), (200), (311), and (222). I^{o}_{hkl} is the reference standard (random) peak intensity for the reflection (*hkl*), JCPDS values of peak intensity were used. The term in the denominator represents an average over all observed (*hkl*) reflection of the ratio of measured to standard peak intensity values [14].

3.6.4 Pole figure XRD

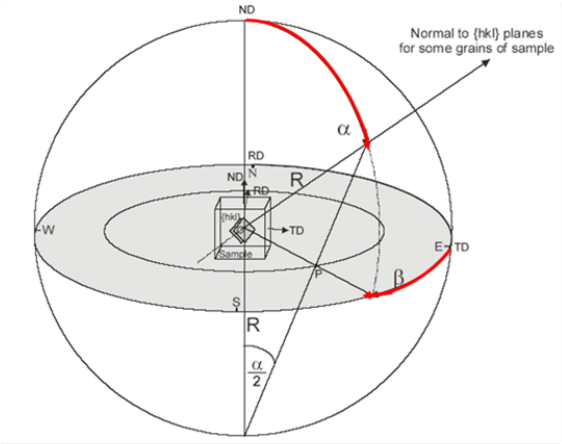

Fig. 3.8: *The principle of using a stereographic projection to create a pole figure. The pole figures are characterized by angles α and β, where α ranges (angular or radial) are from 0° at the center to 90° at the edge, and the β ranges (azimuthal) are from 0° to 360°. The definition of α and β are shown in figure. The point where (hkl) plane normal intersects the sphere (the point defined by α and β angles) is projected in the pole figure in point P, hence $OP = R\,tg\left(\frac{\alpha}{2}\right)$.*

Despite the valuable texture information that can be extracted from the θ-2θ scans, the method outlined above has its inherent limitations. Symmetric θ-2θ scans record intensity at zero tilt angle, $\psi = 0°$, i.e. only from (hkl) planes parallel to the sample surface [15]. In contrast, when grains are aligned along an axis inclined to the surface normal, the θ-2θ scans may not reveal the true orientation or even gives a misleading result. In those cases, pole figure measurements using a 4-circle diffractometer is necessary to reveal spatial orientation distribution of crystallites.

A pole figure is measured at a fixed Bragg diffraction angle to examine the distribution of that specific orientation. The measurement consists of a series of β-scans, which analyses the in-plane orientation around the center of the sample, at different tilt angles α, also called the azimuthal angle. These angles are indicated in Fig. 3.8. The angle β can be varied between 0° and 360°, while α can be varied between 0° and 90°. The diffraction intensity at a given β and α is proportional to the number of (hkl) planes in Bragg condition.

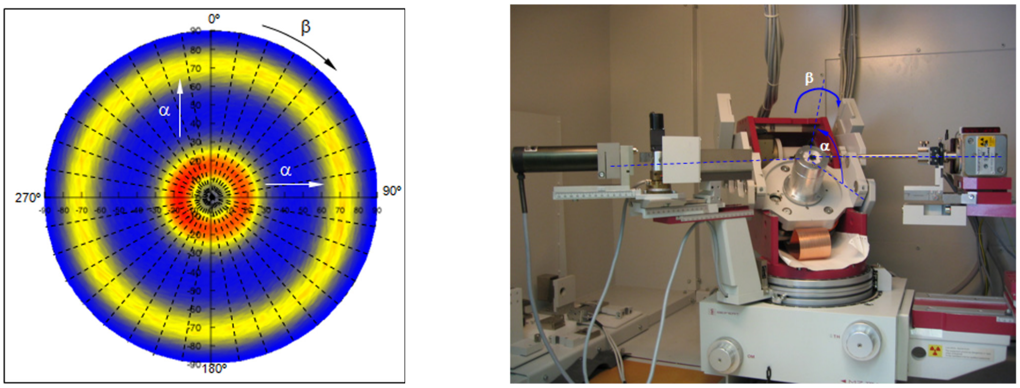

(a) **(b)**

Fig. 3.9: *a) Texture plotting example illustrating how the crystal plane orientations are mapped to texture data plots. b) Geometry for X-ray texture analysis. The source and detector are in symmetric θ-2θ geometry. The film is tilted by an amount α and rotated by an amount β, bringing (hkl) planes of other grains in diffraction condition.*

The pole figure data is displayed as a contour plot with the zero in the center (Fig. 3.9a). Hence, the pole figure gives the probability of finding a given (hkl) plane normal as a function of the thin film orientation. The systematic change in angular direction of the sample is normally achieved by utilizing a four-circle goniometer as displayed in Fig. 3.9b. The pole figure for each (hkl) reflection performed in this thesis took 10 hours.

Types of texture

A classification of the type of textures reported for films is given and various terminologies are discussed (random, fibre texture, and biaxial texture) [16].

Random: A homogeneous distribution of the diffracted intensity across pole figures is observed in the case of a random texture, since no restrictions are imposed on grain orientation. It can be expected that, for a sample with a fully random grain orientation, the intensity ratios of the different peaks observed in a θ-2θ XRD measurement correspond to ratios found in the powder diffraction database (Fig. 3.10a).

Fibre texture: In the case of a typical fibre texture, a particular (hkl) plane is preferentially aligned parallel to the film surface. The direction normal to the surface is generally referred to as the fibre axis. A very dominating intense peak is present at a θ-2θ XRD measurement, as result of the diffraction from the lattice plane that is preferentially parallel to the surface of the film and, in pole figure measurements, a spot in the centre of the pole. When the thin film has a [uvw] out-of-plane orientation, but a random in-plane orientation, then the (hkl) pole figure will exhibit a ring pattern at a tilt angle ψ which corresponds to the angle between the [uvw] direction and the normal of the (hkl) planes as depicted in Fig. 3.10b.

Biaxial texture: Also known as in-plane texture for films deposited under oblique angle deposition. A preferential out-of-plane and in-plane orientation, the ring pattern is transformed into intensity spots, which indicates that a second crystallographic orientation of the grains is aligned to certain direction. A measure for the orientation distribution of grains which are aligned according to a certain direction is the FWHM of the pole in the ϕ direction (Fig. 3.10c).

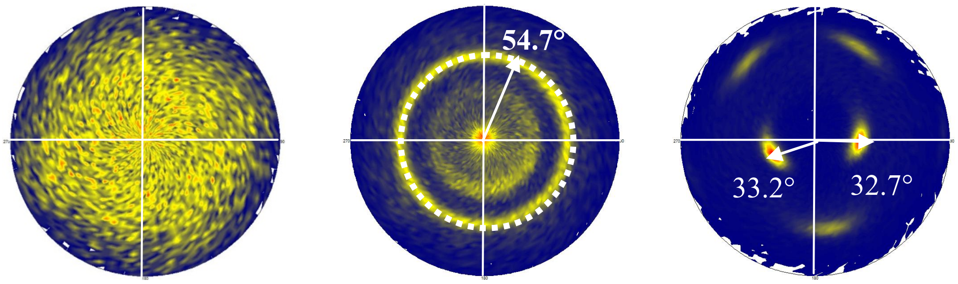

(a) **(b)** **(c)**

Fig. 3.10: *(a) (022) XRD pole figure displaying homogeneous distribution of the diffracted intensity, (b) (111) pole figure illustrating a typical fiber texture with (111) orientation at the center ψ = 0° and random (002) in-plane alignment at ψ = 54.7°, (c) (022) pole figure depicting biaxial texture with preferred in-plane alignment of two (111) poles.*

3.6.5 Stress measurement by x-ray diffraction ($\sin^2\psi$ method)

One important property of thin films, which has been studied extensively in recent years, is their stress state. Advances in thin film technology therefore have been accompanied by efforts to measure the stress and even to control the stress in thin films. PVD coatings contain high levels of residual stress that can have the beneficial effect of increasing the hardness of the coating [17]. In many cases, high compressive stresses are an unwanted side effect of deposited PVD coatings, because they are known to reduce the adhesive strength of the coating on the substrate.

In general, the residual stress in a PVD coating consists of two main components, thermal termed extrinsic) and intrinsic.

a) Thermal stress: When a coated substrate is at a temperature that is different from its temperature during deposition, a thermal stress will be present as a result of the differences in the film and substrate thermal expansion coefficients. For a one-dimensional approximation, the thermal stress is given as [18]:

$$\sigma_{thermal} = \frac{E_f}{1-\upsilon_f}\left(\alpha_f - \alpha_s\right)(T_r - T_s) \tag{3.5}$$

where E_f is Young's modulus in Pa, α_f and α_s are the coefficients of thermal expansion for the film and substrate, respectively, in 1/°C, T_r is the room temperature, and T_s is the deposition temperature. A positive value of $\sigma_{thermal}$ corresponds to tensile stress whereas a negative one corresponds to compressive stress.

b) Intrinsic stress: Intrinsic stress is less well understood. It can be defined as the component of the total measured stress that cannot be attributed to external or thermal stress. The intrinsic stress can depend on such variables as the substrate temperature, deposition rate, film thickness, and background chamber ambient. Intrinsic stress develops in films during the growth process. The magnitude of intrinsic stress is related to the microstructure of the film which, in turn, depends on the kinetic energy of atoms condensing on the substrate or other energetic species impinging on the surface during film growth [19].

Sin$^2\psi$ method

The XRD sin$^2\psi$ technique can be used to selectively measure the lattice spacing of only those crystals of a selected phase, which have a specific orientation relative to the sample surface, by measuring θ and calculating *d* from Bragg's law. To calculate the lattice spacing (d_ψ) of other orientations relative to the sample surface, the sample is tilted in ψ directions. The stress (σ) can be expressed in terms of the crystal lattice spacing in the form of equation 3.6.

$$\sigma = \frac{E_f}{(1+\upsilon_f)sin^2\psi}\left(\frac{d_\psi - d_0}{d_0}\right) \tag{3.6}$$

Rearranging the above equation we obtain,

$$d_0\sigma(1+\upsilon_f)sin^2\psi = E_f(d_\psi - d_0) \tag{3.7}$$

$$d_\psi = \left(\frac{1+\upsilon_f}{E_f}\right) d_0 \sigma \sin^2\psi + d_0 \qquad (3.8)$$

Where E_f and ν_f are the elastic modulus and the Poisson's ratio of the film under investigation, respectively, and d_0 is the stress-free lattice spacing.

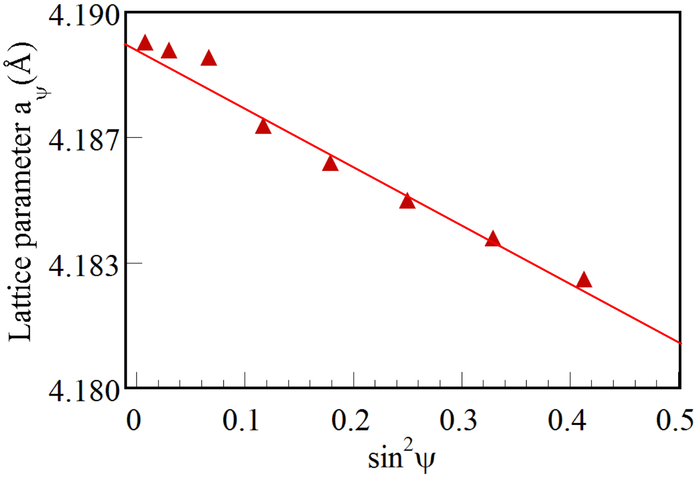

Fig. 3.11: *Lattice spacing of (002) planes* a_ψ *versus* $\sin^2\psi$ *of a TiAlN thin film determined by conventional XRD for different tilt angles* ψ*. The film exhibits compressive stress due to the negative slope of the plot.*

The lattice spacing a_ψ plotted against $\sin^2\psi$ yields a straight line. The stress is determined from the slope, if the elastic constants and the unstressed lattice spacing are known. A positive slope indicates tensile stress while a negative slope corresponds to compressive stress. This is illustrated in Fig. 3.11 which depicts compressive stress of a TiAlN film determined using this technique [20]. For textured materials, the X-ray elastic constants S_1 and $S_2/2$ are used instead of E and υ. S_1 and $S_2/2$ may be obtained from the literature for a given material and reflection combination. If experimental values are not available, they may be calculated from single crystal elastic constants using various approximations described in [20].

3.7 Structural characterization of the coatings

3.7.1 Scanning electron microscopy

Scanning electron microscopy (SEM) has been used to characterize the surface morphology and fractured cross-section of the films. In SEM, an electron beam is focused in to a small probe and scanned in a raster pattern across the surface of a sample. The electron beam interacts with the sample, generating different signals. By detecting these signals, and correlating signal intensity with probe position, images of the sample surface are generated. The nature of the image depends on the type of signal collected. The most commonly detected signals are: secondary electrons for imaging surface morphology; backscattered electrons for compositional imaging; and X-rays for compositional analysis. For our purpose, high resolution SEM (FEI XL30 SFEG) was used to obtain information on the surface and cross-section morphology of the coatings.

For the cross-sectional view of the samples deposited under oblique angles, the samples were cleaved in the direction of the flux. Adobe Photoshop CS2 was used to measure the tilt angle of the nano columns from the cross-sectional view. Additionally, a plasma cleaner was used for the removal of hydrocarbon-based contaminants in SEM samples.

3.7.2 Transmission electron microscopy

The conventional transmission electron microscopy (TEM) involves the illumination of a transparent object by a beam of electrons, and the formation of a magnified image of the electron waves emerging from the object using an objective lens and two or more projector lenses. TEM is a versatile technique capable of characterizing the internal structure of a large variety of materials. This characterization includes not only the imaging of the microstructure directly but, at the same time, the identification of the phases present in the specimen by either electron diffraction or spectroscopic chemical analysis [21]. The results obtained from a typical TEM characterization of materials allow a better understanding of the relation between microstructure and properties (Fig. 3.12). There are a rich variety of operation modes of the electron microscope. The bright field (BF) mode is commonly used to image grain and defect structures within materials. It can also reveal second phases such as precipitates and inclusions. The dark field (DF) imaging mode makes use of the specific Bragg diffracted electrons to image the region from which they originate. The DF mode enables the link between the crystallographic information and specific regions or phases in the sample. The primary purpose of the electron diffraction technique is to identify the crystal structure of the materials under investigation. By placing an aperture in the image plane, then projecting the diffraction pattern of that image onto the recording plate, one obtains the selected area electron diffraction (SAED) technique. TEM observations were carried out on a Philips CM12 microscope with a LaB_6 filament and at 200 keV (without intentional heating of the sample). In addition, high resolution-transmission electron microscopy (HR-TEM), FEI Tecnai Osiris working at 200 kV, was used to obtain the bright field image and selected area electron diffraction patterns (SAED) at various regions of film thickness. Moreover, high resolution images were taken. Gatan Digital Micrograph software was used for fast Fourier transform (FFT) analysis of the corresponding HR-TEM images.

To prepare suitable cross-section samples for TEM, films were prepared by mechanically polishing down to a thickness of few μm. Further reduction of the thickness of a small region to roughly 20 nm was achieved by ion milling in a Gatan PIPS at 6-8° incident angle with Ar^+ ions at 2.5 kV. TEM sample was also prepared using Zeiss NVision 40 CrossBeam with focused ion beam (FIB) technique. A specific TEM lamella preparation (lift-out in situ) is used. The region of interest is first covered by a protecting material (carbon or platinum). Holes are milled on each side of the lamella. This last one is lifted-out by a micromanipulator and glued on a support where the final thinning takes place.

The preparation of TEM specimens involves polishing. As a result, artifacts can originate at different stages of sample preparation. Sometimes, it may be difficult to distinguish the artifacts from the actual microstructure, especially in nanomaterials. In this context, a correlation with the results obtained through other tools may be used to identify them. Also, a prior knowledge of the material system may help in identifying the artifacts. In addition, the commonly-used ion milling technique can also create artifacts resulting from the interaction of the energetic ions with the material unless extreme care is taken to use very low ion energies and very shallow angles of incidence.

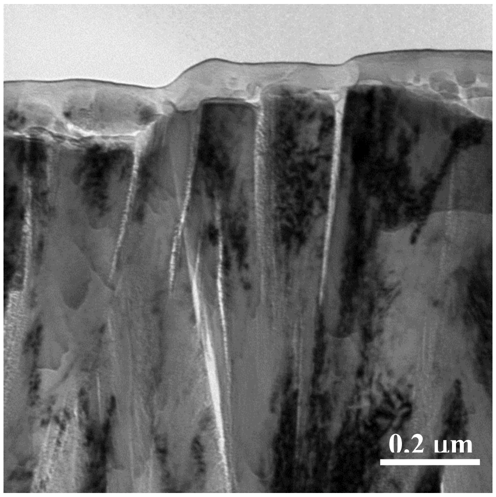

Fig. 3.12: *Sample bright field TEM image of a TiAlN film deposited under oblique angle incidence. Such kind of voided and porous columnar structure can only be seen in a conventional TEM, which makes them more preferred than SEM for viewing such intracolumnar voids .*

3.8 Mechanical properties by nanoindentation

The special interest in nanoindentation comes from its uniqueness in measuring mechanical properties of small volume materials and thin films. This technique is completely different from the conventional tensile or compression testing used to derive elastic modulus or hardness [22]. The relation between stress and strain in nanoindentation is quite complicated since the contact area between the indenter and the material under load during indentation is not constant for most of the indentation cases. Therefore, the classical relation of Hooke’s law cannot be directly used to derive modulus using indentation. In this chapter, the basic theory of nanoindentation will be introduced and review of the development of indentation theories will be given.

3.8.1 Experimental aspects

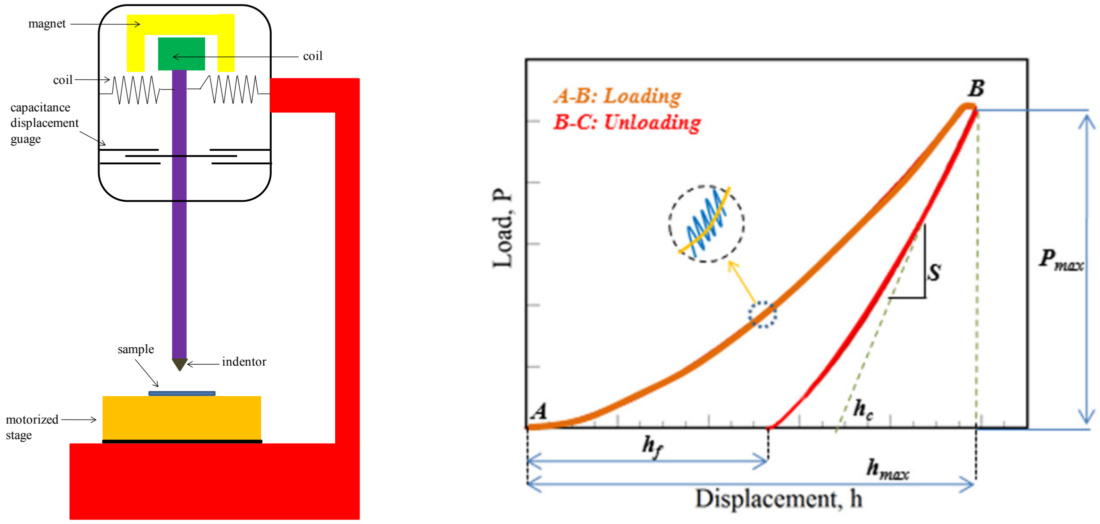

a) **b)**

Fig. 3.13: *a) Schematic of MTS Nanoindentor XP. b) Load-unload curve from a sample with elasto-plastic behavior. The stiffness, S, is determined from the initial slope of the unloading curve. The nanoindenter system applies a load to the indenter tip to force the tip into the surface while simultaneously superimposing an oscillating force with force amplitude generally several orders of magnitude smaller than the nominal load.*

The nanoindentation was performed on MTS Nanoindentor XP (Fig. 3.13a). Berkovich indentor is used to produce indentation. A particular aspect of this machine is the possibility of indenting in a continuous stuffiness mode (CSM) where the tip oscillates with a frequency of about 70 Hz and 2 nm of amplitude which superposes to the overall motion of the indenter. Such an operating mode provides a quasi-continuous series of calculated elastic modulus and hardness as it is displayed in Fig. 3.13b. The CSM technique makes the continuous measurement of mechanical properties of materials possible in one sample experiment without the need for discrete unloading cycles, and with a time constant that is at least three orders of magnitude smaller than the time constant of the more conventional method of determining stiffness from the slope of an unloading curve. The measurements can be made at exceedingly small penetration depths. Thus this technique is ideal for mechanical property measurements of nanometer-thick films. As a first approach, the hardness values were taken at a depth between 100 - 200 nm to avoid influence of the surface roughness and from the substrate.

3.8.2 Measurement of elastic modulus

The most common method for measuring hardness and modulus using nanoindentation methods involves making a small indentation in the film, while continuously recording the indentation load, *P*, and displacement h, during one complete cycle of loading and unloading [23]. Stiffness of the contact between the indenter and the material being tested is required to determine the mechanical properties of interest. The stiffness, *S*, is determined from the initial slope of the unloading curve. The loading and unloading portion can be seen in Fig. 3.13b. Once the stiffness is measured using equation $S = dP/dh$, the reduced modulus can be determined as:

$$E_r = \beta \frac{\sqrt{\pi}}{2} \frac{S}{\sqrt{A}} \qquad (3.9)$$

where β is the constant that depends on the geometry of the indentor (β = 1.034 for a Berkovich indentor) and E_r is the reduced modulus, which accounts for the measured elastic displacement contributing from both the sample and the indenter tip. The reduced modulus can be used to calculate the actual modulus of the sample, which is given by:

$$\frac{1}{E_r} = \frac{1-\upsilon_f^2}{E_f} + \frac{1-\upsilon_{tip}^2}{E_{tip}} \qquad (3.10)$$

where $E_{tip} = 1140$ GPa and $\upsilon_{tip} = 0.07$ are the elastic modulus and Poisson's ratio for diamond tip, respectively. From this equation, we can calculate the E_f for the given sample [24].

3.8.3 Hardness

Hardness is the resistance to the plastic deformation and it is given by [24]:

$$H = \frac{P_{max}}{A} \qquad (3.11)$$

where P_{max} is the peak indentation load and *A* is the projected area of the hardness impression using the depth of contact, h_c. Fig. 3.13b is the schematic representation of load versus displacement during nanoindentation. The contact depth h_c is calculated using Oliver and Pharr's method as expressed in the following equation:

$$h_c = h_{max} - \varepsilon \frac{P_{max}}{S} \qquad (3.12)$$

where ε is the geometric constant (0.75 for a Berkovich indenter tip). The contact depth h_c can be solved by using appropriate ε for equation 3.12. Therefore the projected contact area can be calculated using the area function:

$$A = 24.5h_c^2 + C_1 h_c + C_2 h_c^{1/2} + \cdots + C_8 h_c^{1/128} \qquad (3.13)$$

Where C_1, $C_2, \ldots C_8$ are constants which can be obtained by least square method [24].

3.9 Reference

[1] F.R. Bunshah, Deposition Technologies of Films and Coatings, Noyes, Park Ridge, NJ (1982).

[2] H. Köstenbauer, Phd Thesis, Leoben University.

[3] J. Lopez, W. Zhu, A. Freilich, A. Belkind, K. Becker, J. Phys. D: Appl. Phys. 38 (2005) 1769.

[4] A. Belkind, A. Freilich, R. Scholl, Surf. Coat. Technol. 108–109 (1998) 558.

[5] S. M. Rossnagel, Handbook of Plasma Processing Technology ed S M Rossnagel et al, Park Ridge, NJ: Noyes, 160.

[6] R. Cremer, K. Reichert, D. Neusch¨utz, G. Erkens, T. Leyendecker, Surf. Coat. Technol. 163–164 (2003) 157.

[7] D. Deniz, T. Karabacak, J. M. E. Harper, J. Appl. Phys. 103 (2008) 083553.

[8] A. R. Shetty, A. Karimi, M. Cantoni, Thin Solid Films 519 (2011) 4262.

[9] A. R. Shetty, A. Karimi, Phys. Stat. Sol (b) 249 (2012) 1531.

[10] J. M. Nieuwenhuizen, H. B. Haanstra, Philips Tech. Rev. 27 (1996) 87.

[11] R. N. Tait, T. Smy, J. M. Brett, J Vac. Sci. Technol. A 10 (1992) 1518.

[12] D. Kohl, PhD thesis, University of Aachen.

[13] B. D. Cutliy, Elements of X-ray Diffraction, Addison-Wesley Publishing Company, Inc, US (1964).

[14] D. S. Rickerby, A. M. Jones, B. A. Bellamy, Surf. Coat. Technol. 37 (1989) 111.

[15] B. C. Okolo, PhD thesis, University of Stuttgart (2003).

[16] C. Detavernier, C. Lavoie, ICOTOM14 (2005).

[17] A. C. Vlasvelda, S. G. Harrisa, E. D. Doylea, D. B Lewis, W. D. Munz, Surf. Coat. Technol. 149 (2002) 217.

[18] R. Machunze, A. P. Ehiasarian, F. D. Tichelaar , G.C.A.M. Janssen, Thin Solid Films 518 (2009) 1561.

[19] J. L. Perry, PhD thesis, Rochester Institute of Technology (2005).

[20] I. C. Noyan, J. B. Cohen, Residual Stress, Measurement by Diffraction and Interpretation Springer-Verlag, New York (1987).

[21] R. Martins, PhD thesis, University of Libson (2008).

[22] S. Yang, M.Sc thesis, National University of Singapore (2003).

[23] J. Reddy, M.Sc thesis, University of South Florida (2007).

[24] W. C. Oliver, G. M. Pharr, J. Mater. Res. 19 (2004) 3.

Chapter 4:

Texture change and off-axis accommodation through film thickness

4.1 Overview of the present chapter

In this chapter, to gain an overall picture for the evolution of texture with film thickness and substrate material, analytical x-ray diffraction (XRD) techniques like θ–2θ scans and pole figure XRD were utilized. The $Ti_{0.5}Al_{0.5}N$ coatings were deposited on amorphous glass, polycrystalline WC-Co and single crystal Si (100) substrates at 650°C. No substrate bias was applied. Based on the results obtained, the growth texture mechanism is discussed in two parts: tilted <002> away from film normal on WC-Co and glass, and <002> nearly parallel to film normal on Si at higher thickness. Furthermore, we also try to study the effect of substrate temperature on the off-axis of (002) at higher thickness.

4.2 Texture evolution through film thickness on amorphous substrate

4.2.1 Texture study by θ–2θ scans

Fig. 4.1 displays the θ–2θ scans of $Ti_{0.5}Al_{0.5}N$ films on glass deposited at various thicknesses. It can be seen that low thickness TiAlN film on glass substrate reveals a (002) preferred orientation (288 nm, Fig. 4.1a). For a 900 nm thick film, a strong (002) texture is observed with a weak contribution from the (111) peak. As the thickness increases (2.32 μm), the intensity of (111) gradually increases while that of (002) peak decreases. The resulting XRD pattern for a 4.09 μm thick film exhibits a strong (111) orientation with only a very small peak at the (002) position. Some minor presence of (113) is also seen at higher thickness.

In most of the texture studies [1], it has been reported that the (002) diffracted intensity saturates and the intensity of the (111) reflection gradually increases with film thickness. For instance, Schell et al. [2] found that the volume of the (111) grains [their (111) planes are parallel to the film surface seen in vertical Bragg–Brentano geometry steadily increases with thickness, while the volume of the (002) grains levels off and then remains nearly constant with thickness. However, in our case the intensity of (002) reflection decreases with film thickness. Moreover, the (111) out-of-plane orientation gradually increases with film thickness.

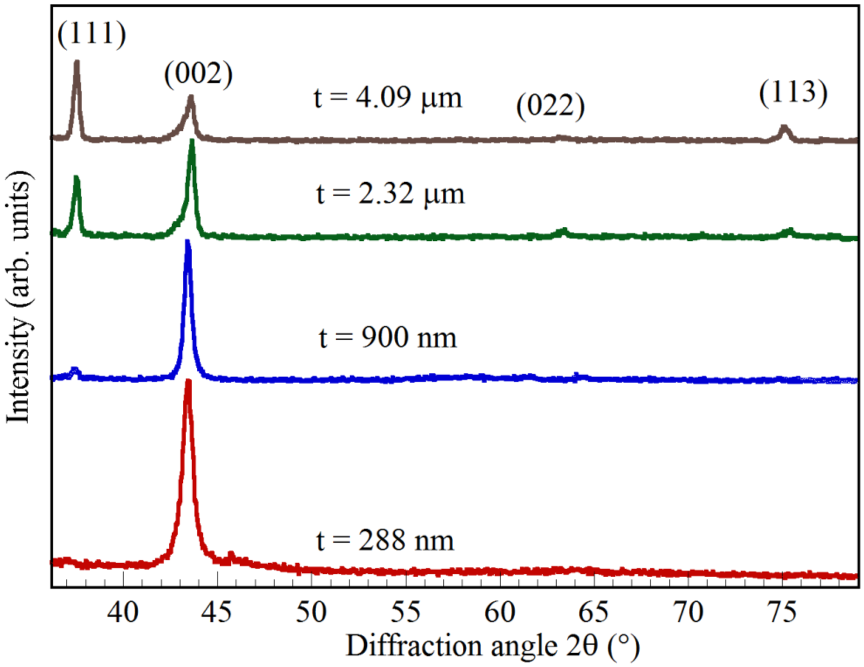

(a)

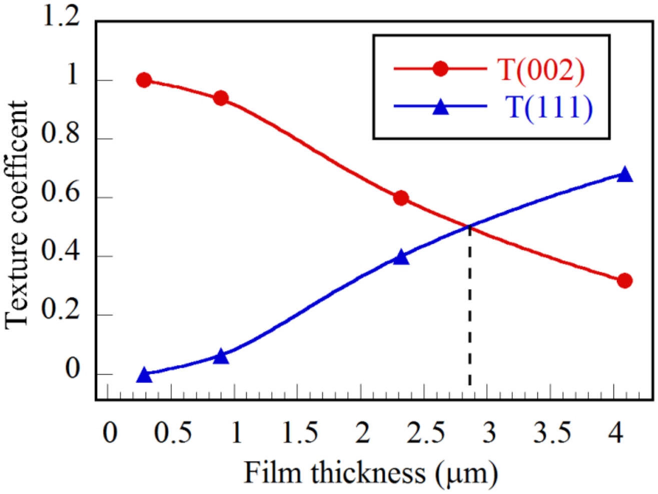

(b)

Fig. 4.1: *a) Bragg–Brentano XRD patterns of $Ti_{0.5}Al_{0.5}N$ coatings deposited on glass at various thicknesses. b) Variation of texture coefficients* T*(002) and* T*(111) with film thickness estimated from θ–2θ scans featuring the crossover from (002) to (111) at 2.8 μm.*

To follow the texture evolution with film thickness, the plot of (002) and (111) texture coefficient obtained by *θ*–2*θ* scans with film thickness is displayed in Fig. 4.1b. The *T*(002) texture coefficient is nearly constant for thickness around up to 900 nm, which then drastically decreases when film thickness is increased from 2.32 μm to 4.09 μm. On the other hand, the *T*(111) texture coefficient increases with the thickness from 288 nm to 4.09 µm. From the plot of Fig. 4.1b, one can consider that the crossover from (002) to (111) occurs at around 2.8 µm.

Unfortunately, the Williamson-Hall plot could not be applied for thinner samples since the intensities for (222) and (004) reflections were too low for a reliable analysis. Thus for the purpose of comparing grain size relative to different orientations, Scherrer's formula, which neglects the contribution of the microstrain, may be used. Fig. 4.2 displays the evolution of (111)- and (002)-oriented grains with film thickness. It can be clearly seen from the figure that (111)-oriented grains are larger and the size of (002) grains decreases for the thickest film along the growth direction for films deposited on glass. While the (002)-oriented grains dominate at low thickness, the size of (111) grains increases significantly with thickness. An important conclusion that can be drawn is that when a mixed texture exist at low thickness, the (111) grains grow faster than (002) ones.

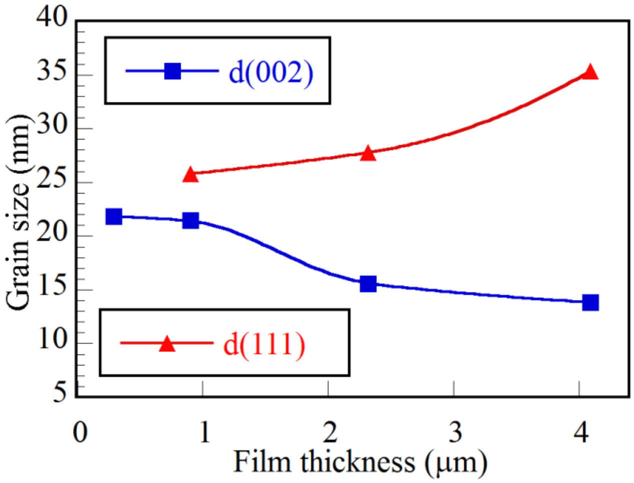

Fig. 4.2: *Variation of grain size relative to (111) and (002) orientations with film thickness on glass substrates.*

Combining θ–2θ scans and texture coefficient plot (Figs. 4.1a and b) reveal that the texture at low thickness is dominated by (002) crystallographic planes parallel to the substrate surface. At later stages, the growth of grains with <111> crystallographic orientation parallel to the substrate normal surpasses with minor presence of (002) orientation. However, from analysing the pole figure results (section 4.2.2), it appears that this is not the case, and that the (002) planes still constitute the surface but are tilted away from the surface normal. This will be discussed further in the next section.

4.2.2 Fibre texture study by pole figure XRD

The pole figures of $Ti_{0.5}Al_{0.5}N$ films for various (hkl) reflections deposited on glass substrates are featured in Fig. 4.3. For a 288 nm thick film, the (002) pole figure displays strong reflections at the center of the pole with some random intensity distributions (Fig. 4.3a). The (111) pole figure reveals reflections in a ring pattern at $\psi = 54.7°$ which are diffracted from (002) grains. For the (022) pole figure, a weak ring of reflections at around $\psi = 45.5°$ belonging to the family of (002) planes is seen. The (113) pole figure is characterized by ring type intensity pattern at $\psi = 22.3°$ diffracted from (002) grains.

The (002) pole figure observed for a 900 nm thick film reveals an improved (002) texture with most the reflections concentrated at the center of the pole (Fig. 4.3b). The (111) pole figure exhibits the presence of (002) reflection in the form of a strong ring at a diffraction angle of $\psi = 54.3°$. Similarly, a ring type intensity at around $\psi = 45.1°$ diffracted from in-plane (002) grains is observed in the (022) pole figure (Fig. 4.3b). Meanwhile, a cylindrical diffracted pattern at $\psi = 23.1°$indicating (002) planes is seen in the (113) pole figure.

When the film thickness is reached at around 2.32 μm, the (002) planes are still parallel to the substrate surface (Fig. 4.3c). However, some weak reflections are seen at diffraction angles between $\psi = 16°$-$19°$, which indicates the tilting of some (002) planes. Other weak reflections are also seen at around $\psi = 72.1°$. The (111) pole figure demonstrates that majority of the diffracted intensity maxima is now concentrated at the center of the pole with few scattered reflections around it. These few reflections might correspond to the tilted (002) crystallites observed in the (002) pole figure (Fig. 4.3c). A ring pattern of reflections at around $\psi = 55.2°$ is seen in the (111) pole figure which are diffracted from (002) planes. In case of (022) pole figure, the diffracted intensity is in the form of a broad ring that can be considered as consisting of 2 rings at a diffraction angle of $\psi = 35.3°$ and 45.4° indicating (111) and (002) planes, respectively. The (113) pole figure now shows a very weak texture formation at the origin along with a ring at $\psi = 30.4°$ diffracted from randomly in-plane orientated (111) crystallites. Thus from the pole figure analysis, we can assume that films deposited at 2.32 μm on glass feature a mixed (111) and (002) texture.

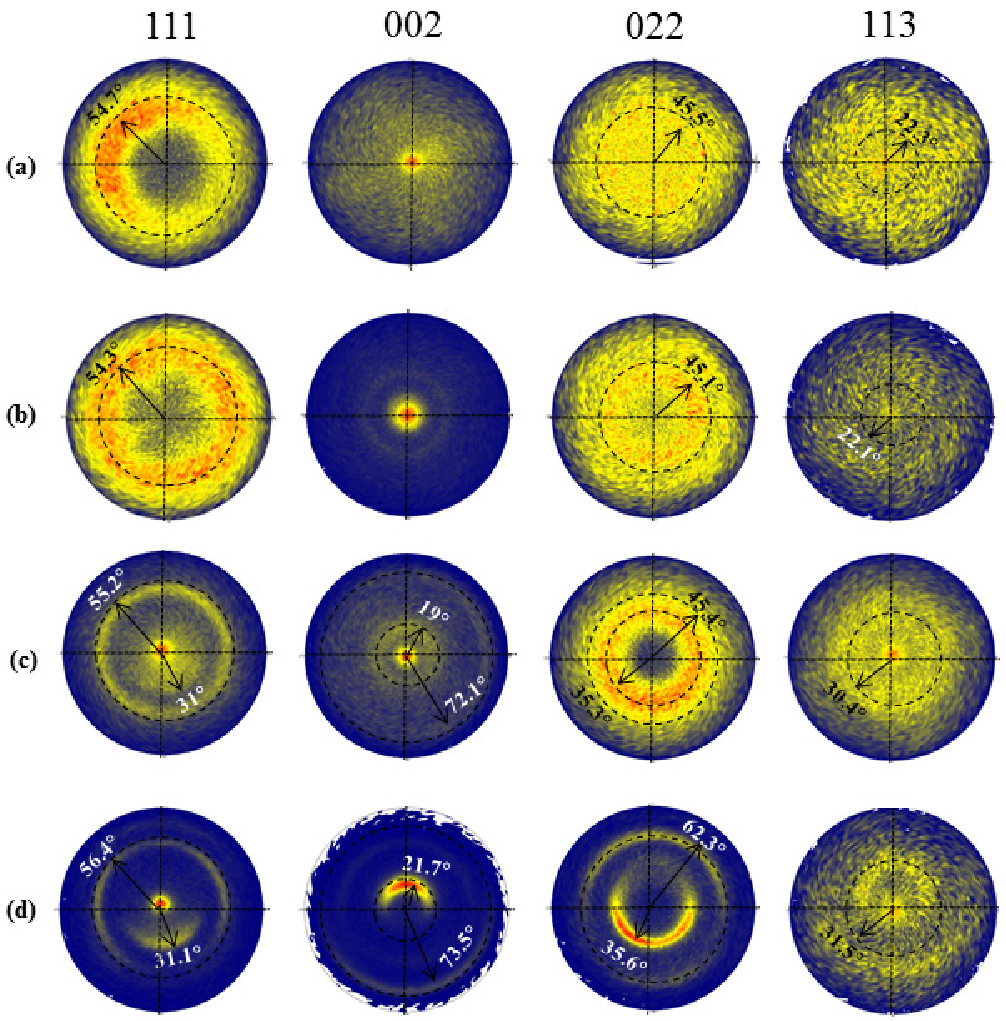

Fig. 4.3: *Pole figures from (111), (002), (022) and (113) reflections of $Ti_{0.5}Al_{0.5}N$ films deposited on glass at different thicknesses; (a) thickness t = 288 nm, (b) t = 900 nm, (c) t = 2.32 µm, and (d) t = 4.09 µm. The pole figures reveal that the (111) planes are parallel to substrate surface while the direction of <002> is tilted away at higher thickness.*

Finally, for a 4.09 µm thick film, the (002) planes are no longer parallel to the substrate surface but tilted away from the surface normal at $\psi = 21.7°$. In addition, some diffraction intensities are observed at $\psi = 73.5°$. There is some controversy as to whether the inclined texture observed here is due to the tilted (002) or diffraction of grains having (113) planes parallel to surface. As far as a cubic system is concerned, the interplanar angle between (113) and (002) is 25.1°. The θ-2θ scan for made for the same film reveals a minor presence of (113) out-of-plane orientation at higher thickness (4.09 µm, Fig. 4.1a). With such negligible presence of (113), we assume that the (113) orientation is too weak to form a fibre texture for thicker films. Thus we can conclude that the inclined texture observed in the (002) pole figure originates from the (002) crystallites. This off-axis tilt results in the reduction of (002) peak intensity observed in the θ–2θ scan in comparison to previous thicknesses (Fig. 4.1a). The (111) pole figure depicts a strong (111) texture with the majority of intensity maxima concentrated at the center of the pole. Some weak scattered reflections at ψ = 31.1° are seen. Additionally, a ring at ψ = 56.7°diffracted from (002) planes is seen (Fig. 4.3d). The (022) pole figure exhibits 2 rings, a strong ring of diffracted intensity at around ψ = 35.6° belonging to the (111) planes and a weak incomplete ring at around ψ = 62.3° diffracted from in-plane (002) crystallites. The θ–2θ scans and (113) pole figures reveal a negligible presence of (113) orientation for this thickness regime.

Similar kind of inclined texture has also been reported by other authors. For example Falub et al. [3] reported the preferred orientation of the crystallites is tilted with respect to the surface of the samples. They concluded that the inclination of the (002) diffracting planes increased with increasing residual compressive stress in the coating and suggested that there is an interdependence between intrinsic stress and fiber texture. Rajafa et al. [4] also observed a texture tilt for TiAlN coatings and showed that this inclination depends on the deposition geometry. However, the texture revealed by these authors did not have a fiber texture and this was ascribed to the non-rotating substrate. Correspondingly, Shetty and Karimi [5] found a tilted texture in TiAlN deposited by pulsed DC magnetron sputtering. They explained this tilted preferred orientation by the oblique paths between the substrate and incident flux. One could explain the obtained tilted texture by using the evolutionary selection model of Van der Drift [6]. In this model, the difference in growth rates between several crystal planes at the surface of the film causes the fiber texture, i.e. crystal grains oriented with their slower growing direction normal to the surface are terminated, while those with the highest component of the growth rate perpendicular to the substrate are selected.

4.3 Influence of substrate on texture evolution during film growth

So far we have seen that the texture growth behaviour changes with film thickness for $Ti_{0.5}Al_{0.5}N$ films grown on amorphous glass substrate. In order to understand the influence of substrate in choosing the final orientation of the film, we have deposited $Ti_{0.5}Al_{0.5}N$ under same deposition conditions on single crystal Si(100) and polycrystalline WC-Co substrates. In the following sections, we show that films deposited on Si(100) do not display any off-axis tilt of (002) at higher thickness. Rather, the θ–2θ scans and pole figure XRD results reveal that films show a dominant

<002> orientation nearly parallel to film normal through the film thickness. On the other hand, films deposited on WC-Co feature an inclined (002) texture similar to films on glass at higher thickness.

4.3.1 Development of (002) orientation with film thickness on single crystal substrate

a) Out-of plane orientation study by θ–2θ scans

The θ–2θ XRD scans observation is in stark contrast for the films deposited on Si(100). The main texture is (002), but a small amount of (111) can also be detected. The films do not depict any kind of crossover with increasing thickness (Fig. 4.4a), and the intensity of both (002) and (111) diffraction peaks increase with film thickness. The θ–2θ scans also show signals from (113) planes, but their intensity is negligible when compared to (002) peak intensity. Fig. 4.4b corresponds to the plot of texture coefficient T(111) and T(002) with increasing film thickness. For films on Si, the T(111) did not reveal any major change in values with film thickness. On the other hand, the T(002) remained nearly constant through the film thickness, which indicates that the films have a dominant (002) orientation on Si substrates.

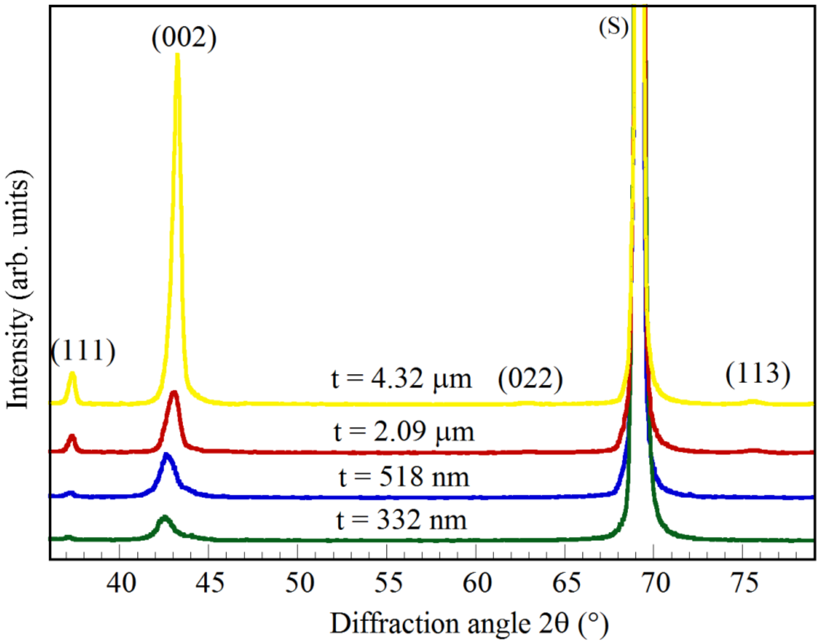

(a)

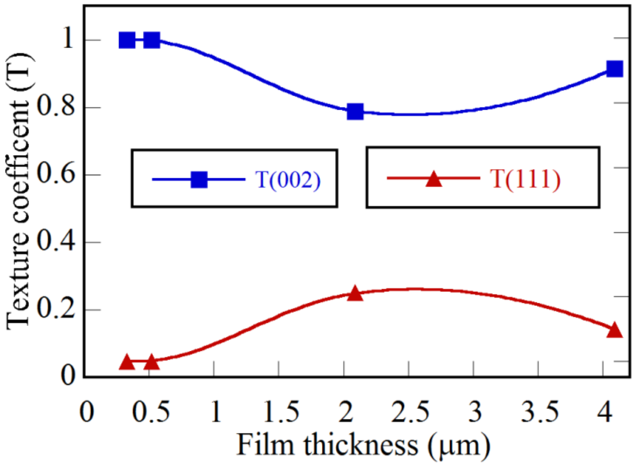

(b)

Fig. 4.4: *a) θ–2θ scans of* $Ti_{0.5}Al_{0.5}N$ *coatings deposited at various thicknesses on Si substrates showing the emergence of dominant (002) orientation with film thickness. b) Texture coefficients T(002) and T(111) obtained from θ–2θ scans as a function of film thickness. The symbol S in a) corresponds to Si(400) peak.*

Fig. 4.5 exhibits the growth of (111)- and (002)-oriented grains with film thickness on Si substrates. The size of (002)-oriented grain increases with film thickness, whereas (111) grains did not show any significant change.

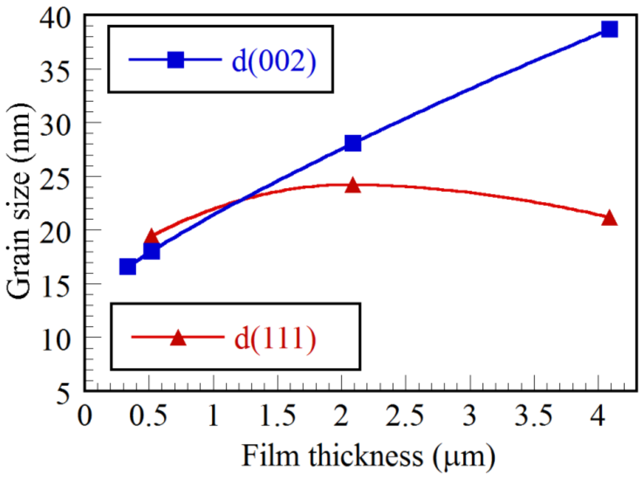

Fig. 4.5: *Grain size obtained from (111) and (002) reflections on Si substrates.*

b) Study of texture evolution by pole figure XRD

Fig. 4.6 displays the pole figure data of $Ti_{0.5}Al_{0.5}N$ films for (111), (002), (022), and (113) reflections deposited on Si substrates at various thicknesses. The presence of symmetric intense poles observed in the (113) pole figures for all the samples emerges as an effect of the substrate. The (113) peak of TiAlN (2θ ~ 75°) lies at the tail of the Si(400) peak (2θ = 69.13°) that makes the measurement of (113) pole figure very troublesome. A dominant (002) texture is seen during the film growth, with presence of a weak (111) at higher thickness. For a 332 nm and 518 nm thick film, the (002) reflections are concentrated close to the center of the pole but with a slight inclination (around 5°-7°). This tilt is to release the strain developed at the substrate-growing layer interface [7]. The (111) pole figure for both the film thicknesses displays a ring pattern of reflections diffracted from (002) grains at a Bragg angle around ψ = 54°. Similarly a weak ring of reflections belonging to (002) planes is also seen at ψ ~ 45° in the (022) pole figure. The (002) planes continue to grow with this slight off-normal deviation for a 2.09 μm thick film on Si. The presence of a weak (111) texture is seen at the center of the pole along with a diffracted intensity in the form of a ring at around ψ = 54.3°. The (022) pole figure also illustrates a ring pattern belonging to a family of (002) planes at ψ = 45°. This is in contrast to the (022) pole figure for films around the same thickness range on glass which displayed a broad ring consisting of both (111) and (002) reflections. The (113) pole figure now reveals the formation of a weak (113) texture at the center of the pole (Fig. 4.6c). Finally for a 4.32 μm thick film, the (002) pole figure did not demonstrate any major change in texture development in comparison to previous thickness range films. The film retained its (002) texture. Note that this behaviour of (002) is completely different to the tilted <002> observed on glass (Fig. 4.3d) at higher thickness. The (111) pole figure exhibits some weak (111) reflections at the center of the pole along with a ring pattern at ψ = 54.4° belonging to the family of (002) reflections. The (022) pole figure for a 4.32 μm thick film features a diffracted ring pattern at ψ = 45.1° belonging to (002) planes. On the other hand for the same thickness range, the (022) pole figures on glass displayed two distinct group reflections, one at ψ ~ 35° associated with (111) reflections and other around ψ ~ 62° attributed to tilted (002) crystallites. Meanwhile, the (113) pole figure is characterized by a weak <113> orientation at the origin along with a ring at ψ = 23.5° which are diffracted from (002) grains.

Thus the obtained results are in contrast to the films deposited on glass. The films deposited on Si demonstrate that (002) is the dominant orientation throughout the film growth and not (111).

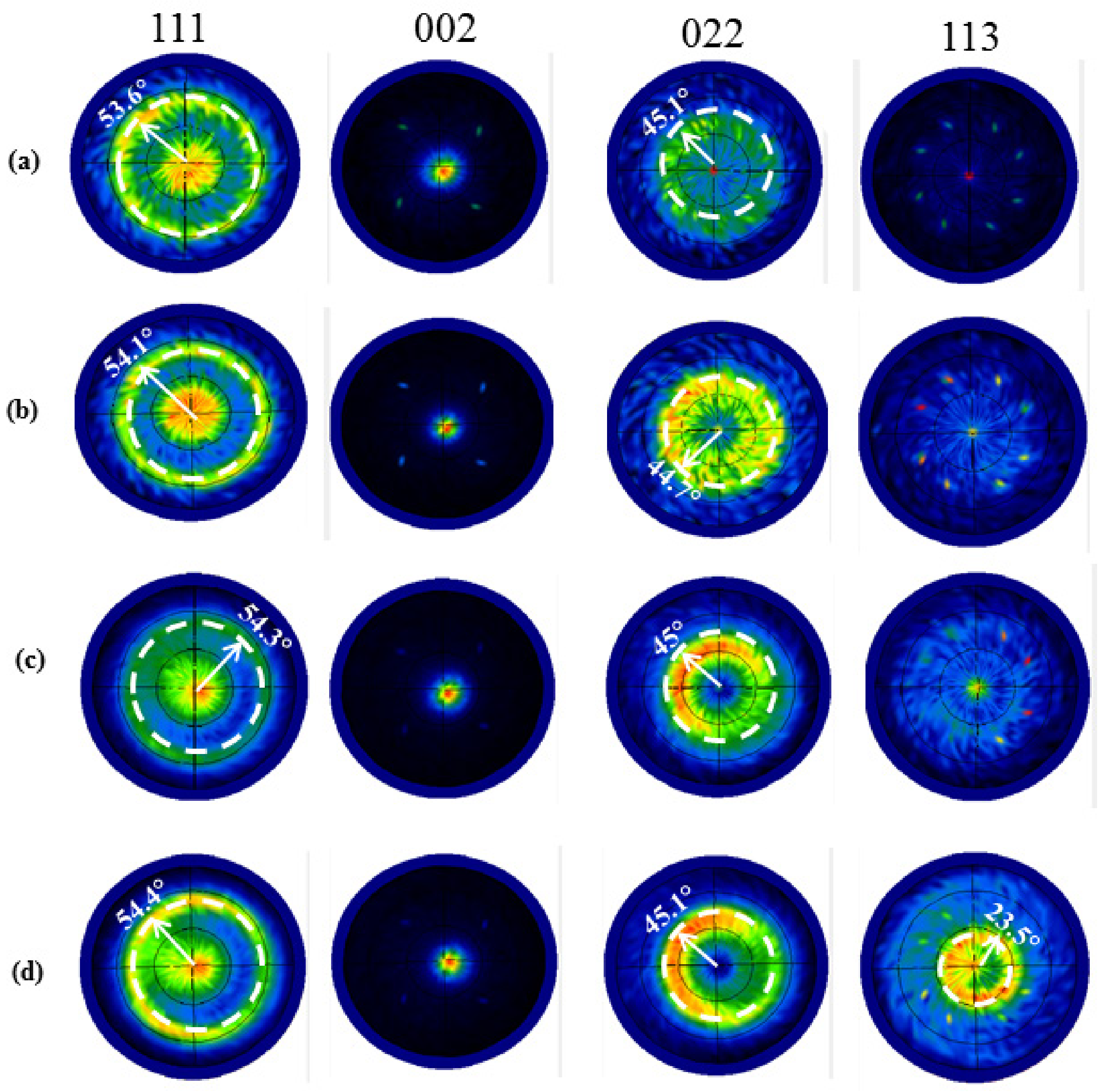

Fig. 4.6: *Pole figures from (111), (002), (022) and (113) reflections of films deposited on Si(100) at different thicknesses; a) t = 332 nm, b) t = 518 nm, c) t = 2.09 µm, and d) t = 4.32 µm. The films display a dominant (002) texture with film thickness.*

4.3.2 Texture study on polycrystalline substrate

a) Out-of plane orientation study by *θ–2θ* scans

The evolution of *θ–2θ* XRD scans for $Ti_{0.5}Al_{0.5}N$ films on WC-Co with increasing thickness is depicted in Fig. 4.7a. The XRD profiles are similar to those obtained on glass substrates (Fig. 4.1a). The deposition is started by predominant growth of (002) crystallographic planes parallel to film surface for a 104 nm thin film. At 860 nm, a weak (111) peak began to appear besides the strong (002) peak. For a 1.92 µm thick film, the (002) peak still remained dominant, but the (111) became significant also. However, for a 4.49 µm thick film, the (111) peak became prevalent, but the (002) peak is no longer seen. This indicates that growth of the grains with <111> crystallographic orientation parallel to the substrate normal becomes dominant at later stages. Moreover, the diffraction peak of (113) at the Bragg angle of 2θ = 76.1°, if present, cannot be seen due to the overlap of film and substrate peak (Fig. 4.7a).

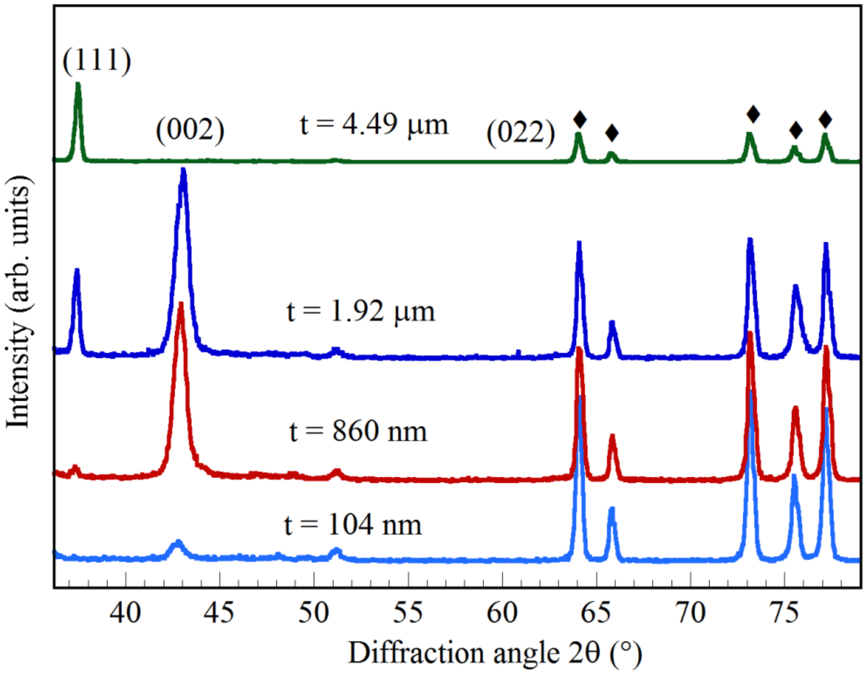

(a)

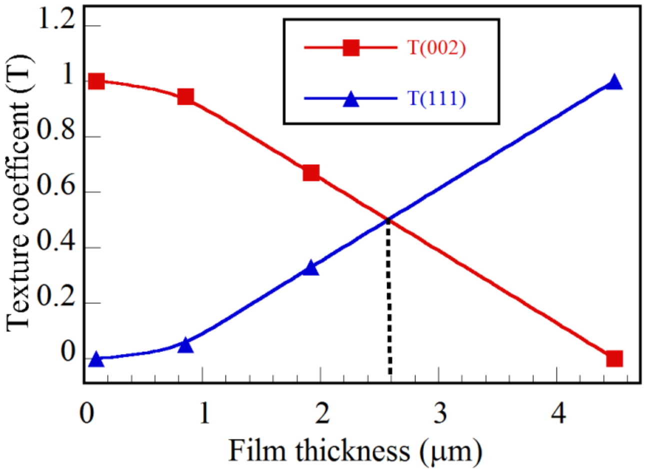

(b)

Fig. 4.7: *a) Bragg–Brentano XRD patterns of* $Ti_{0.5}Al_{0.5}N$ *coatings deposited at various thicknesses. The scans reveal that films at low thickness are dominated by (002) plane parallel to the surface, and at higher thickness the (111) orientation takes over. Symbol ♦corresponds to WC-Co substrate. The scans are similar to films on glass. b) Variation of texture coefficients T(002) and T(111) with film thickness estimated from θ–2θ scans showing the crossover from (002) to (111) occurs at 2.6 μm.*

Fig. 4.7b features the plot of texture coefficient T(111) and T(002) with film thickness. For films on WC-Co, the T(111) increases through film thickness which indicates that thick films have strong (111) preferred orientation. On the other hand the T(002) is seen to decrease with film thickness. For films deposited on WC-Co, the size of (111)-oriented grain increases with film thickness, whereas the (002) grains are seen to decrease for thicker films as displayed in Fig. 4.8.

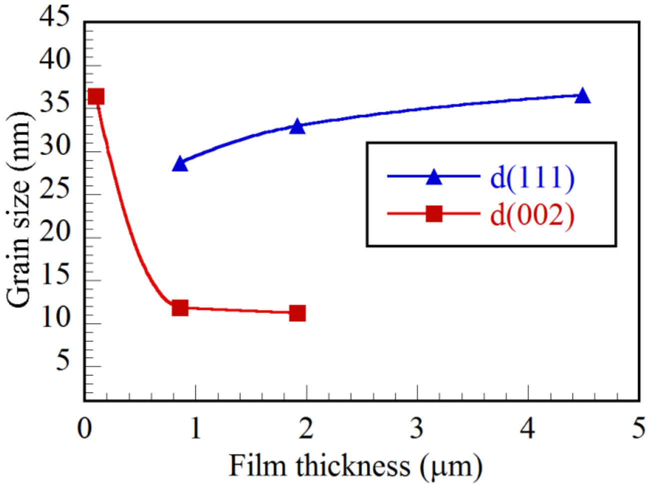

Fig. 4.8: *Comparison of grain size between (111) and (002) orientations. The plot displays an increase in (111) grains along with decrease in (002) grains during film thickening.*

b) Texture evolution study by pole figure XRD

The X-ray pole figures for samples deposited at various thicknesses are shown in Fig. 4.9. The pole figures for (111), (002), and (022) reflections of 104 nm thick film are displayed in Fig. 4.9a. For the (002) pole figure, most of the reflections are concentrated close to the center of the pole but with a few degrees of off-axis tilt. That means the (002) planes are nearly parallel to the substrate surface. This tilt is due to the lattice mismatch at the interface between the substrate and the growing film. This off-axis tilt could also be considered as the result of slightly oblique angle flux. However, in our case, the angle of incidence flux was fixed at $\alpha = 90°$. If we indeed had an oblique angle flux then with increasing thickness one should observe the same off-axis tilt effect which would result in the formation of a strong biaxial texture [8]. However, in our observation, the (002) planes again become parallel to the substrate surface (Fig. 4.9b) with increasing thickness, which confirms that this off-normal tilt is due to the lattice mismatch at the interface. The off-axis tilt observation will be explained in more detail in the Discussion section. However, no such off-axis tilt is detected for films on glass around this thickness range (Fig. 4.3a), whereas on Si this tilt is noticed (Fig. 4.6a). In case of the (111) pole figure, the diffracted intensity is not located at the center of the pole, but forms a ring at a diffraction angle around $\psi = 55.6°$ (Fig. 4.9a). This broad ring corresponds to the (002) as the interplanar angle between the (111) and (002) is 54.7° for a cubic system. This means that the (111) planes are not parallel to the substrate surface. Similarly in the case of (022) pole figure, the diffracted intensity displays a ring pattern around $\psi = 44°$, which corresponds to the interplanar angle between (022) and (002) being 45° (Fig. 4.9a).

The pole figures of the film deposited at a thickness of 860 nm are displayed in Fig. 4.9b. The (002) reflections are concentrated at the center of the pole indicating that the (002) planes are now parallel to the substrate surface. That means the lattice mismatch which caused the tilting of (002) planes at low thickness is now no longer seen with increasing thickness. This is due to the stress relaxation and control of surface energy over interface energy with increasing thickness. In contrast for films on Si, the (002) continues to growth with off-axis direction with film thickness (Figs. 4.6c and d). The (111) pole figure depicts the diffraction intensity in the form of a ring at around $\psi = 54.4°$ corresponding to (002). Similarly, the (022) pole figure features a diffraction intensity in a ring pattern at around 43.8° corresponding to (002).

As we further increase the thickness to 1.92 μm, the (002) pole figure reveals that majority of the reflections are at the center of the pole, but some reflections are tilted at a wide range of diffraction angles up to 23°, which means that at this stage some of the (002) planes starts to tilt away from the surface normal and some weak reflections are also seen at around $\psi = 73.1°$ (Fig. 4.9c). This is also confirmed by the decrease in (002) texture coefficient values (Fig. 4.7b) for the same film thickness. At this thickness, the presence of (111) diffraction intensity maxima is also at the center of the pole, indicating that the (111) planes are now parallel to the substrate surface, though there are also some weak reflections scattered around 30°. These weak reflections correspond to the tilted (002) crystallites.

One can also observe from the (111) pole figure that the diffracted intensity at around $\psi = 55.0°$, corresponding to (002), is much lesser compared to previous two thicknesses. The (022) pole figures can be considered of consisting of 2 rings, a strong ring of diffracted intensity at around $\psi = 35.3°$, which corresponds to (111) and a weak ring at around $\psi = 45.7°$ corresponding to (002). Thus from the pole figure analysis, we can assume that films deposited at 1.92 μm feature a mixed (111) and (002) texture. Similar kind of texture is also seen for films on glass around the same thickness range (Fig. 4.3c)

In case of the 4.49 μm thick $Ti_{0.5}Al_{0.5}N$ film (Fig. 4.9d), the (002) reflections are not at the center of the pole but are tilted away from the substrate normal at about $\psi = 21.2°$ (Fig. 4.9d). Because of this tilt, the (002) peak is not seen in θ-2θ scan for the same sample (Fig. 4.7a). The (111) pole figure reveals that most of the diffraction intensity is concentrated at the center of the pole, indicating that (111) planes are parallel to the film surface. Few reflections are seen at around $\psi = 30°$ and 57°. The (022) pole figure is composed of 2 rings, a strong ring of diffracted intensity at around $\psi = 34.2°$, which corresponds to (111), and a weak ring at around $\psi = 61.6°$ corresponding to (002). The off-normal tilt of the (002) pole to 21.2° results in the interplanar angle between (002) and (022), being shifted by 61.6° instead of being at a standard value of 45°. Thus the θ–2θ scans and pole figure XRD demonstrate different aspects of texture growth at higher thickness for films on WC-Co .

The crystallographic results thus point out that the texture mechanism is similar for $Ti_{0.5}Al_{0.5}N$ films deposited on WC-Co and glass substrates.

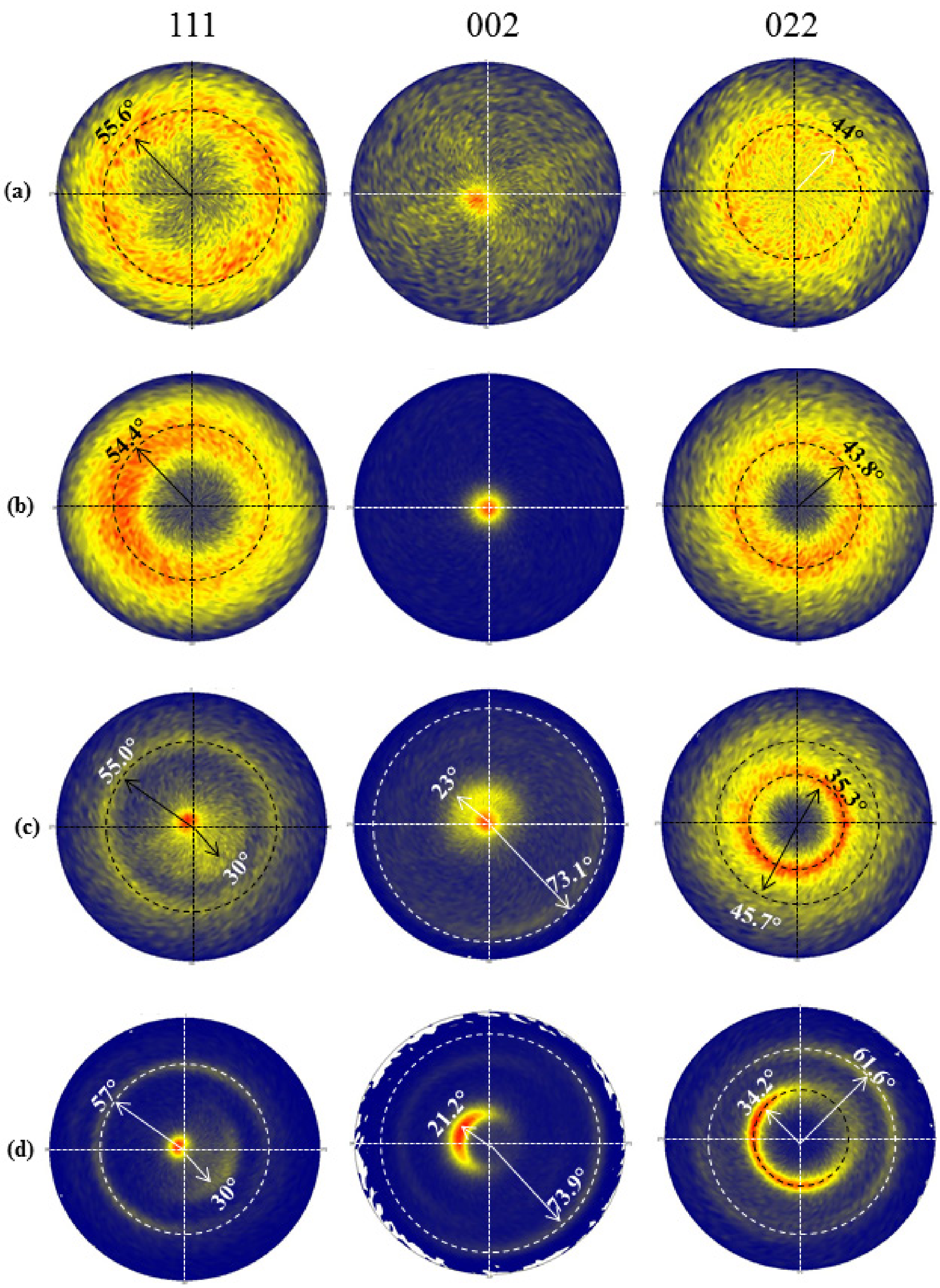

Fig. 4.9: *Pole figures from (111), (002) and (022) reflections of* $Ti_{0.5}Al_{0.5}N$ *films deposited at different thicknesses; (a) thickness* t = *104 nm, (b)* t = *860 nm, (c)* t = *1.92 µm, and (d)* t = *4.49 µm. The (002) planes, which initially parallel to the surface at low thickness, are tilted away from the film normal at higher thickness. On the other hand, the <111> direction is parallel to film normal at higher thickness. The growth behavior is similar to films on glass.*

4.4 Evolution of texture under low adatom mobility conditions

In previous sections, we have seen that on polycrystalline and amorphous substrates, the (002) grains are tilted away from the film normal with film thickness for $Ti_{0.5}Al_{0.5}N$ films. However, the texture growth mechanisms reported were performed at higher substrate temperature conditions (650°C) i.e. increased adatom mobility. Hence it was found interesting to understand this off-axis tilting behaviour of (002) under the conditions of low mobility. For this purpose, we have prepared a series of films under similar conditions at higher thickness range (~ 4 µm) deposited at various substrate temperature extending from room temperature to 650°C on WC-Co substrates.

4.4.1 Influence of substrate temperature on off-axis tilt of (002)

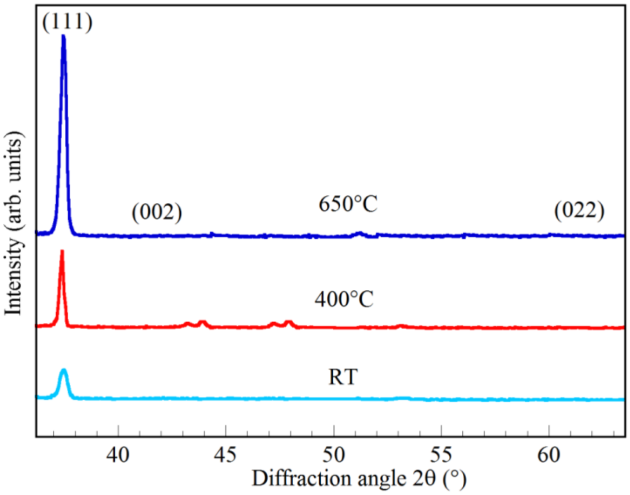

Fig. 4.10: *θ–2θ scans of 4 µm thick films deposited at various substrate temperatures. The scans exhibit that the (002) planes are not parallel to surface while the (111) orientation increases with deposition temperature.*

The θ–2θ scans of 4 µm thick films deposited at various temperatures are exhibited in Fig. 4.10. The scans reveal the presence of (111) out-of-plane orientation, but no signal from (002) planes. This indicates that (002) planes are not parallel to the film surface for thick films on WC-Co substrates. Meanwhile, the (111) peak intensity increases when substrate temperature is varied from RT to 650°C. It is well known that increase in substrate temperature allows the coatings to grow their most dense planes parallel to the substrate surface [9]. Because in a TiAlN crystal the (111) is the densest, hence we observe an increase in (111) orientation with deposition temperature.

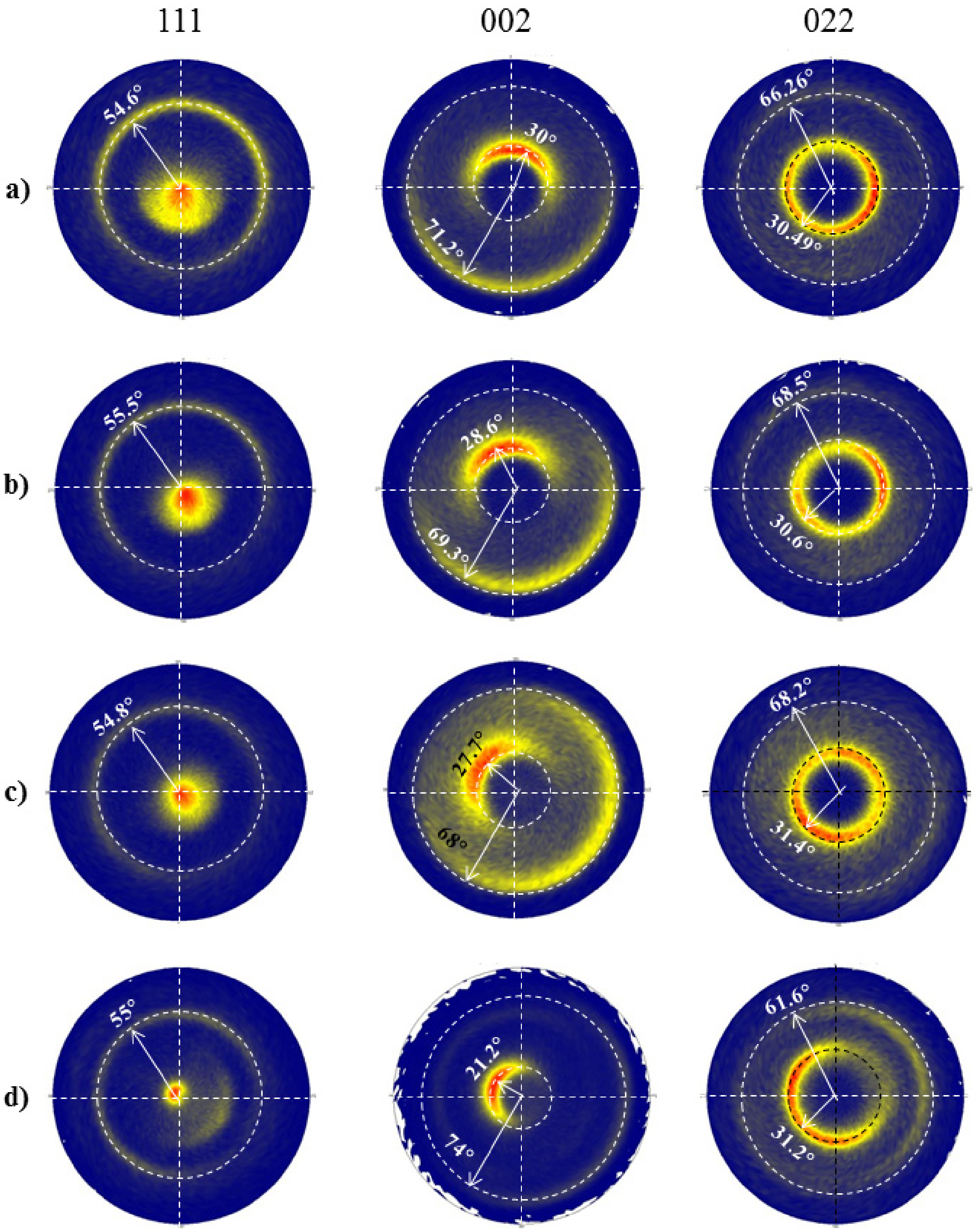

Fig. 4.11: *Pole figures from (111), (002) and (022) reflections of 4 μm thick* $Ti_{0.5}Al_{0.5}N$ *films deposited at various temperatures: a) RT, b) 200°C, c) 400°C, and d) 650°C. The (002) tilt is present in all the films, and it seen to decrease with deposition temperature, whereas the (111) pole intensities become more concentrated at* $\psi = 0°$ *at higher substrate temperature.*

Fig. 4.11 displays the pole figures for (111), (002), and (022) reflections for ~4 μm thick films deposited at various substrate temperatures. It can be seen that for all the films, irrespective of the deposition temperature, the off-axis tilt of (002) is observed. This explains the absence of (002) peak in the θ–2θ scans (Fig. 4.10). However, this off-axis tilt of (002) at higher thicknesses is slightly dependent on the deposition temperature as shown in Figs. 4.11 and 4.12. This can be explained by the increased mobility of the adatoms at higher temperature, which promotes diffusion across grain boundaries and then these (002)-oriented grains try to anchor close to the film normal. Hence we observe a decrease in (002) tilt with increase in deposition temperature. On the other hand, the (111) pole figure shows the (111) pole intensities, which were more scattered at room temperature, are now concentrated at the center of the pole at higher substrate temperature. This means that films show a strong (111) out-of-plane orientation with increase in substrate temperature, as also confirmed by the θ–2θ scans (Fig. 4.10). Thus we can conclude that the off-axis tilting of (002) crystallites is observed for any given deposition temperature.

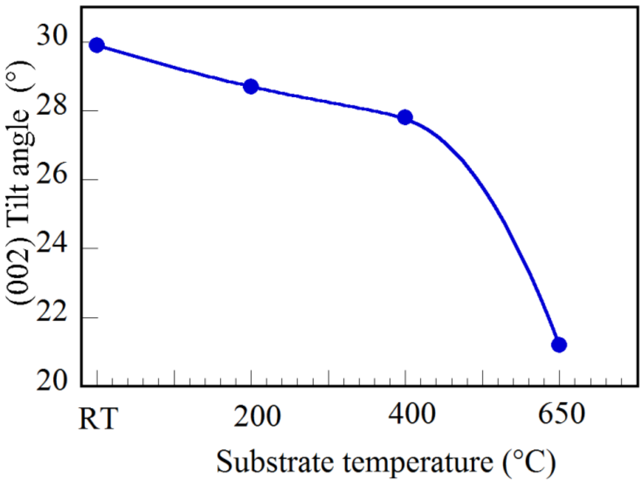

Fig.4.12: *Dependence of off-axis tilt of (002) on substrate temperature at higher thicknesses.*

4.4.2 Change in surface morphology with substrate temperature for thick films

Fig. 4.13 corresponds to the change in top surface morphology with increasing substrate temperature for above discussed thick films. At room temperature and 200°C, layers are made up of grains with pyramidal shape (Figs. 4.13a and b). However, with increase of substrate temperature large sized grains are obtained (Fig. 4.13c). This can be understood with the help of availability of thermal energy at different substrate temperatures. At lower temperatures, the available thermal energy is less for nucleation of atoms and leads to less surface mobility of the deposited atoms [10]. At higher temperatures, the availability of thermal energy is more; which provides sufficient energy to combine (coalescence) the grains on the surface and form larger grains and thus rougher surface.

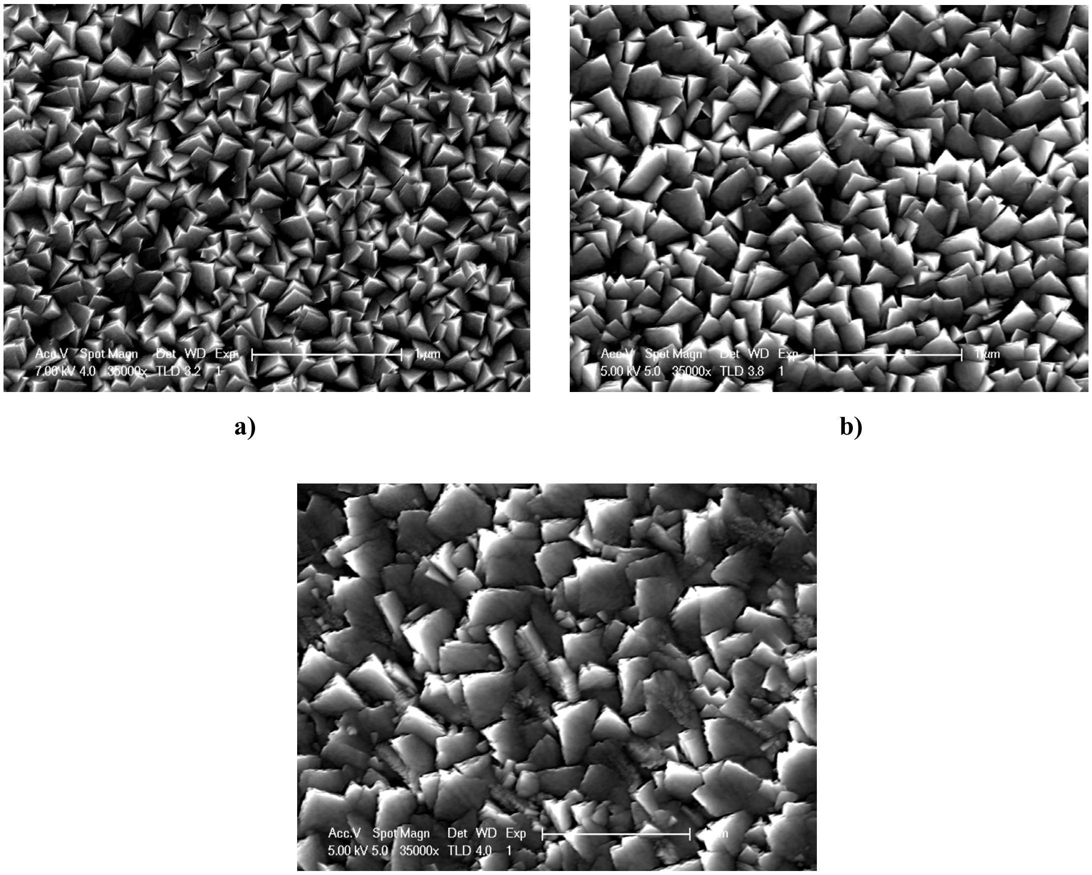

a) **b)**

c)

Fig. 4.13: *SEM surface micrographs of* $Ti_{0.5}Al_{0.5}N$ *films demonstrating the influence of temperature on the surface morphology a) RT, b) 200°C, and c) 650°C.*

4.5 Summary of results obtained from this chapter

The texture behaviour of these films was studied using XRD techniques. It was found that the direction of <002> was thickness dependent on WC-Co and glass, but thickness independent on Si (001). For films on WC-Co and glass, the (002) grains are tilted away at higher thickness. In contrast on Si substrates, a dominant (002) texture develops and always remains nearly parallel to film substrate surface in all thickness.

4.6 Reference

[1] G. Abadias, Y. Y. Tse, J. Appl. Phys. 95 (2004) 2414.

[2] N. Schell, W. Matz, J. Bøttiger, J. Chevallier, P. Kringhoj, J. Appl. Phys. 91 (2002) 2037.

[3] C. V. Falub, A. Karimi, M. Ante, W. Kalss, Surf. Coat. Technol. 201 (2007) 5891.

[4] D. Rafaja, M. Sima, V. Klemm, G. Schreiber, D. Heger, L. Havela, R. Kuzel, J. Alloys Compd. 378 (2004) 107.

[5] A. R. Shetty, A. Karimi, Phys. Stat. Sol (b) 249 (2012) 1531.

[6] A. van der Drift, Philips Res. Pep. 22 (1967) 267.

[7] F. Riesz, Vacuum 46 (1995) 1021.

[8] A. R. Shetty, A. Karimi, M. Cantoni, Thin Solid Films 519 (2011) 4262.

[9] R. Wuhrer, W. Y. Yeung, J. Mater. Sci. 37 (2002) 1993.

[10] M. Devika, N. Reddy, K. Ramesh, V. Ganesan, E. S. R. Gopal, K. T. Reddy, Appl. Surf. Sci. 253 (2006) 1673.

Chapter 5:

Effect of texture change on microstructure, stress and mechanical properties

5.1 Overview of the present chapter

In the previous chapter, we have studied the texture buildup mechanism with film thickness. $Ti_{0.5}Al_{0.5}N$ films deposited on WC-Co and glass showed the off-axis tilting of (002) grains while the <111> direction is parallel to film normal at higher thickness. We also noticed that this texture change is dependent on the nature of substrate especially on Si(100) where no off-axis tilt of (002) planes is observed. The films exhibited a dominant (002) out-of-plane orientation with film thickness. In this chapter, we make an attempt to connect this different texture growth behavior with properties like stress, microstructure and mechanical properties. We observe that intrinsic stress along (111) and (002) displays a strong dependence with preferred orientation. The microstructures of these films were studied by SEM, TEM and AFM. In addition, a correlation between (111) texture, stress, hardness and the type of substrate is obtained.

5.2 Relation between intrinsic stress and preferred orientation

Assuming an equal biaxial stress state, the residual stresses in the coatings were determined by applying the traditional $\sin^2\psi$ method (i.e. by linear fitting the a_ψ versus $\sin^2\psi$ curves for (111) and (002) peaks). The residual stress was measured by monitoring the shift of the maximum position of (111) and (002) reflections at different tilt angles (ψ). Considering that thermal stress of films deposited is independent of layer thickness [1], the intrinsic stress is then obtained by subtracting the thermal stress contribution to the residual stress obtained. The X-ray elastic constants (XECs) for (111) and (002) were obtained from fiber textured cubic TiN films using the Hill hypothesis [2] (Table 5.1).

XECs (x 10^{-3} [GPa]$^{-1}$)	**[111]**	**[002]**
S_1	-0.654	-0.5
$\frac{1}{2}S_2$	3.007	2.561

***Table* 5.1:** *XECs of titanium nitride along [111] and [002]. The XECs for the thin film where calculated as Hill averages, taking into account texture [2].*

5.2.1 Affiliation between $\sigma_{int}^{<002>}$ and off-axis tilt for films on WC-Co

Fig. 5.1 depicts the plot of intrinsic stress $\sigma_{int}^{<111>}$ and $\sigma_{int}^{<002>}$ relative to (111) and (002) orientation for various thicknesses, respectively. Initially the grains having (002) orientation are compressively stressed (-2.8 GPa) for the sample with thickness of around 860 nm. As the film thickness is reached to 4.49 µm, the stress level along the (002) orientation becomes tensile (0.42 GPa). Whereas the stress state of grains having (111) orientation seems to be highly compressive with -4.2 GPa and -3.5 GPa for 1.92 µm and 4.49 µm thick film, respectively.

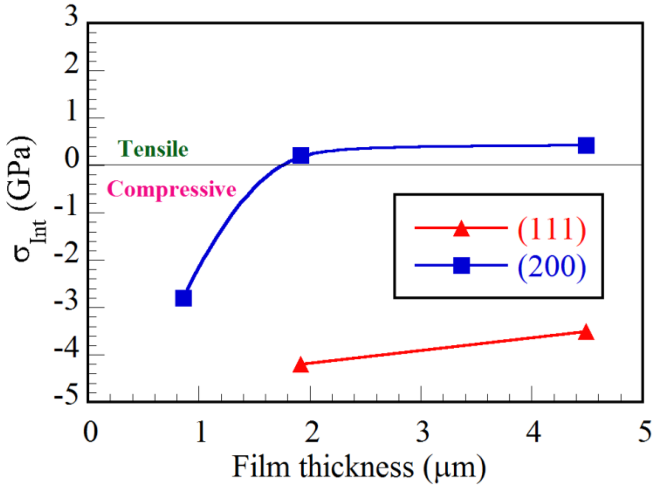

Fig. 5.1: *Intrinsic stress* σ_{int} *relative to (111) and (002) orientation at different thicknesses. With increasing thickness, the* $\sigma_{(002)}$ *changes from compressive to tensile due to the inclination of (002) diffracting planes whereas the* $\sigma_{(111)}$ *remains compressive throughout.*

A closer inspection for $\sin^2\psi$ curves along the (002) reveals a deviation from linearity at higher film thickness (Fig. 5.2). A slight oscillatory behavior along the (002) is seen for a 4.49 µm thick film. We observe that stress along the (002) changes from compressive to tensile through film thickening (Fig. 5.1). As the (111) grains develop with film thickness and since (111) planes sustain more compressive stress (Fig. 5.1), the overall energy of the film gets higher. Earlier results of Oh et al. have also demonstrated that (111) fiber texture arises from significant stress state [3]. Similarly Abadias et al. [4] demonstrated that larger expansion of (111) grains is correlated to higher compressive stress along (111). This energy can be reduced by the tilting of more compliant (002) planes (Fig. 4.9d). We assume that in fcc nitrides, (111) planes are more close-packed than (002) planes for ion bombardment at normal incidence. As a result, the (111) planes suffer greater ion damage while the N^+ ions are channeled through open (002) planes, leaving them relatively undisturbed during growth and thus enabling the (002) planes to tilt away during film thickening [5].

Thus, in order to promote the growth of <111> orientation parallel to film normal at higher thickness, the (002) planes are tilted off-axis resulting in tensile stress along <002>. This causes a deviation from linearity in the a_ψ versus $\sin^2\psi$ plot along (002) at higher thickness (Fig. 5.2b).

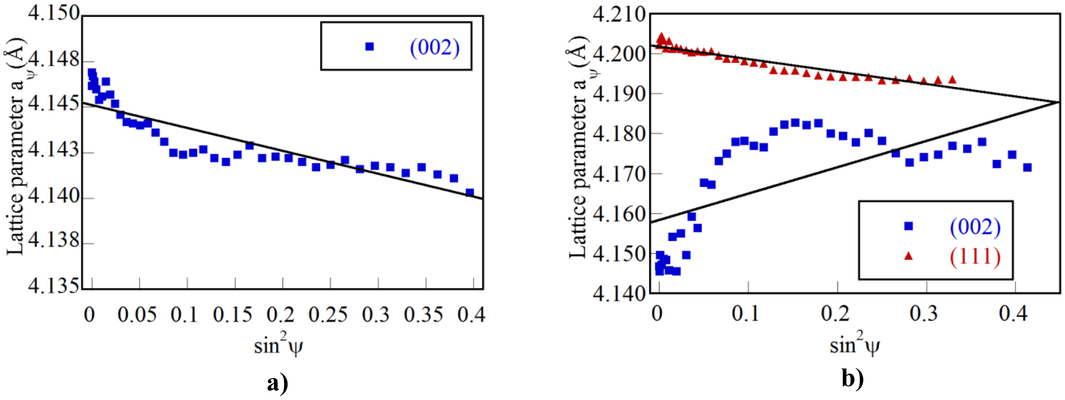

Fig. 5.2: *Lattice spacing a_ψ versus $\sin^2\psi$ plot for a) 860 nm and b) 4.49μm thick film. The stress curves for (002) deviated from linearity at higher thickness due to the off-axis tilting of (002) crystallites.*

According to Falub et al.[6], the inclination of (002) diffracting planes increases with increasing residual stress in the coating.They reported that for a residual stress of ~−3.1 GPa the tilt angle of the (002) is ~14.5°, whereas for a residual stress of ~−9.1 GPa the tilt angle is ~54.4° that corresponds to the (111) fiber texture. The obtained results in our case suggest a correlation between stress and texture in the sputtered $Ti_{1-x}Al_xN$ coatings, such that tilted (002) texture is favoured in films with lower residual stress. Similarly, Je et al. [7] in their studies of tilted (002) texture also reported that stress level along (002) is tensile.

5.2.2 Stress studies for films on Si(100)

Contrasting stress results were obtained for films deposited on Si. The intrinsic stress along (002) remained compressive through the film thickness, unlike for films on WC-Co where the intrinsic stress along (002) changed from compressive to tensile (Fig. 5.1). Meanwhile the $\sigma_{Int}^{<111>}$ along (111) on Si did not reveal any major change in stress values as summarized in Table 5.2.

Thickness	$\sigma_{Int}^{<111>}$ (GPa)	$\sigma_{Int}^{<002>}$ (GPa)
518 nm	---	-3.5
2.09 μm	1.49	-2.9
4.32 μm	1.1	-2.1

***Table 5.2:** Intrinsic stress values along (002) and (111) at various thickness for films on Si.*

The $\sin^2\psi$ plot for 518 nm and 4.32 μm thick films on Si display a linear behavior along (002) with film thickness (Fig. 5.3). Unlike on WC-Co where the stress plot for (002) differed from linearity at higher thickness (Fig. 5.2b). We have observed in chapter 4 that films deposited on Si did not exhibit any texture change to (111) nor any off-axis tilting of (002) occurs at higher thickness. The films reveal a dominant (002) orientation through the film thickness. Thus the film texture mechanism on Si explains the compressive stress behavior along the (002).

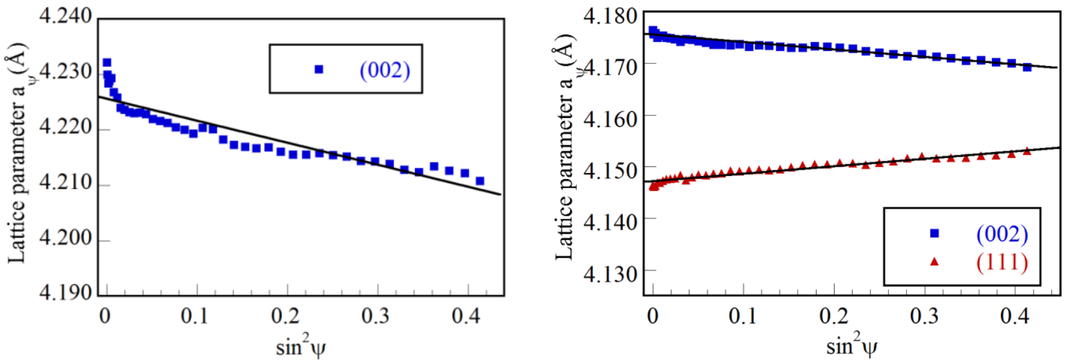

a) **b)**

***Fig. 5.3:** Lattice spacing a_ψ versus $\sin^2\psi$ plot for a) 518 nm and b) 4.32μm thick film. The stress curves for (002) remained linear during film growth.*

5.3 Change in surface morphology with film thickness

The surface texture and morphology play an essential role in determining their properties. In this section, the local features in the film surface of $Ti_{0.5}Al_{0.5}N$ films with a thickness gradient are investigated by means of SEM. A strong dependence of morphology and texture on the film thickness and the nature of substrate is observed, mainly (i) for films on WC-Co which revealed a continuous change in topography with thickness, and (ii) whereas on Si(100) no variation in morphology during film growth was observed.

5.3.1 SEM studies for films on WC-Co

The surface morphology of films with increasing thickness is featured in Figs. 5.4a-c. It can be seen that surface topography changes with film thickness. The surface morphology of an 860 nm film, which consists of round granular surface (corresponding to (002)-oriented grains), is shown in Fig. 5.4a. As the thickness is increased to 1.92 µm, one can see the presence of mixed round and faceted grains (Fig. 5.4b) (indicating the presence of mixed (111)- and (002)-oriented grains). For a 4.49 µm thick film, the surface is dominated by a faceted hill and valley structure (Fig. 5.4c). The pole figure analysis of the same sample reveal that the growth direction of <111> planes is parallel to the substrate normal. However, the (002) planes are tilted away from the film normal at around 21.22° (section 4.3.2, Fig. 4.9d). The facets seen in Fig. 5.4c correspond to (002). Similar kind of morphology is also reported by other authors [7].

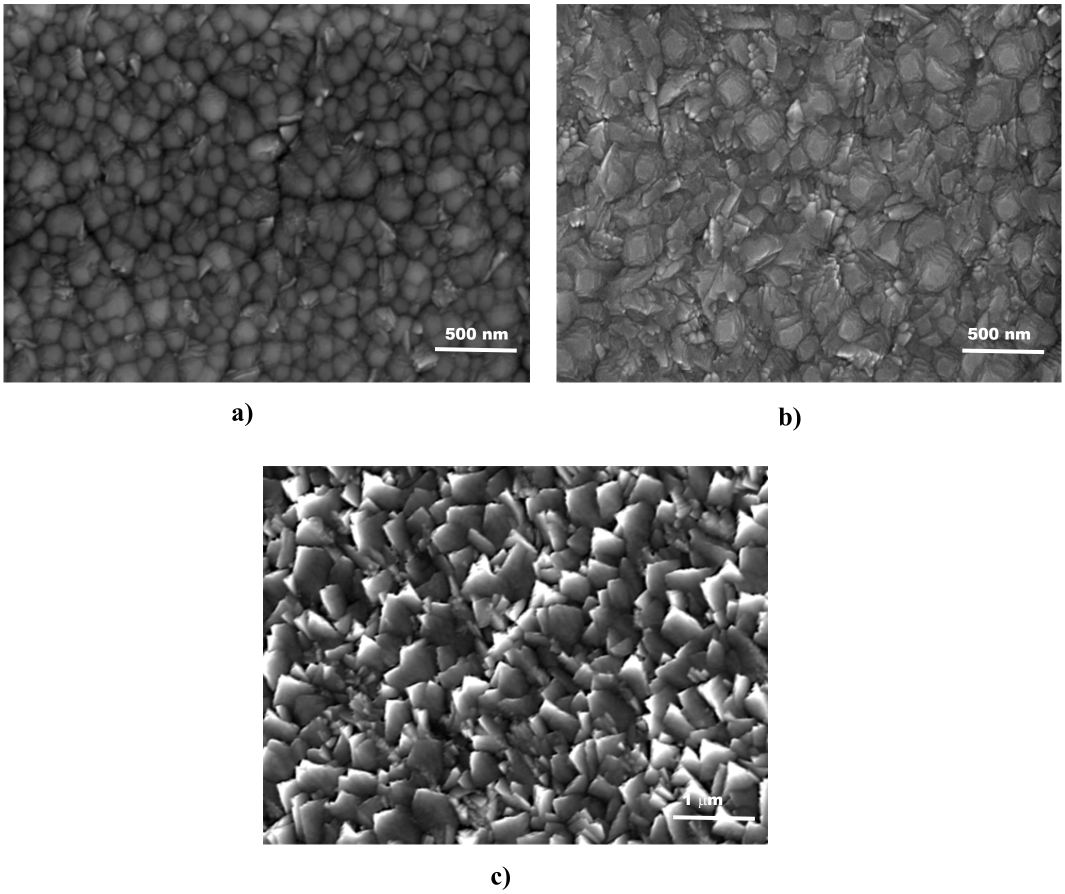

a) b)

c)

Fig. 5.4: *Surface morphology of $Ti_{0.5}Al_{0.5}N$ films deposited at different thicknesses. SEM plane view for (a) thickness* t *= 860 nm, (b)* t *= 1.92 µm, and (c)* t *= 4.49 µm. The morphology is seen to change greatly with deposition time.*

To better understand the relation of the grain size with the thickness of $Ti_{0.5}Al_{0.5}N$ films, we also studied the dependence of the mean surface roughness on film thickness. The variations of the root mean square roughness (R_a) and T(111) as a function of the film thickness are displayed in Fig. 5.5. Both R_a and T(111) increase with film thickness. The surfaces are rougher due to increase in size of (111)-oriented grains (section 4.3.2, Fig. 4.8). Increase in T(111) is mainly related to the onset of competitive growth of crystals with preferred orientation and this also leads to an increase in roughness [8,9].

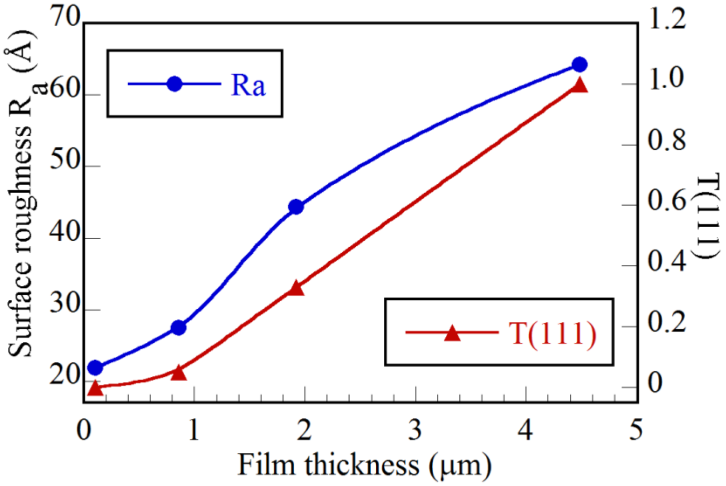

Fig. 5.5: *Correlation between root mean square roughness (R_a) and (111) texture coefficient on film thickness. At higher thickness, films having a dominant (111) orientation will exhibit rougher surface morphology.*

5.3.2 Morphological study for films on Si using SEM

In contrast to films on WC-Co which showed a continuous change in morphology with thickness, films on Si did not exhibit any such changes (Figs. 5.6a-c). The micrographs only reveal the size of grains increases with film thickness. Thus the absence of any major morphological change for films on Si with thickness is in accordance with crystallography results which showed that films have dominant (002) texture through the film thickness (section 4.3.1, Figs. 4.4 and 4.6).

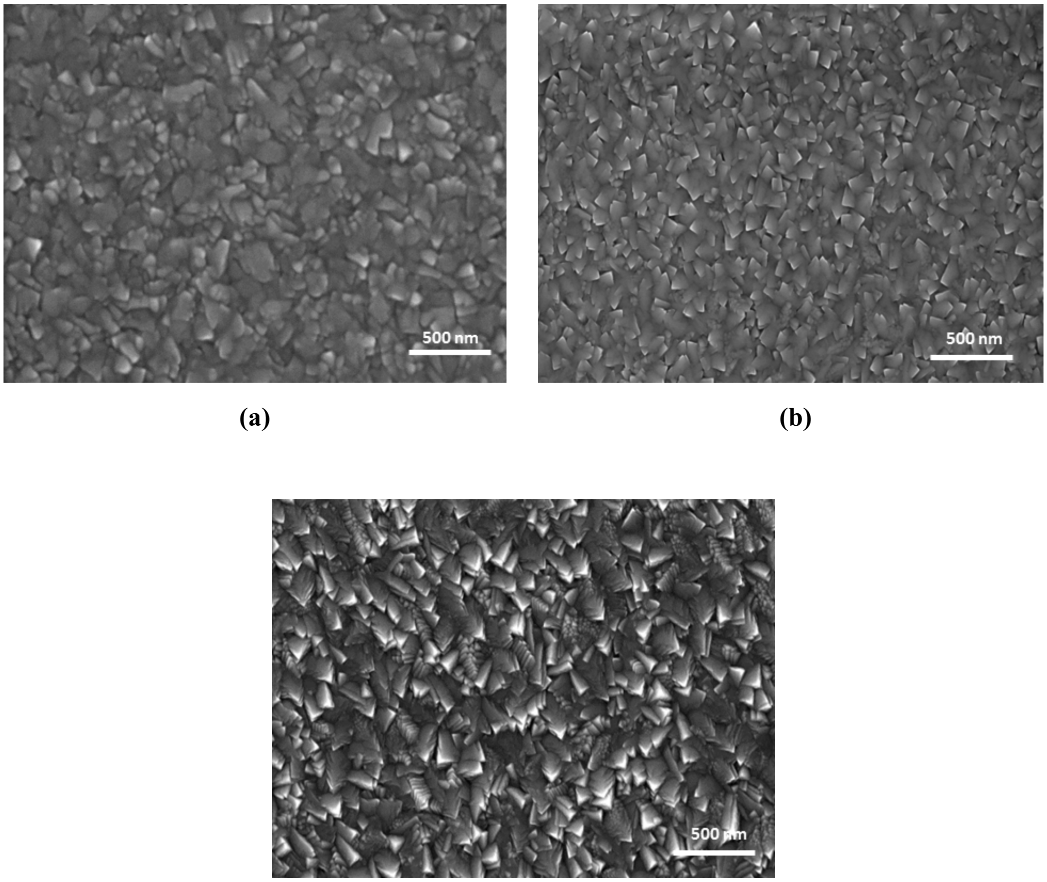

(a) (b)

(c)

Fig. 5.6: *SEM surface topography of $Ti_{0.5}Al_{0.5}N$ films on Si deposited at different thicknesses. SEM plane view for (a) thickness* t = *518 nm, (b)* t = *2.09 µm, and (c)* t = *4.32 µm. The morphology does reveal not any drastic change with film thickness.*

Obviously, the growth exponent and roughness exponent of films deposited on WC-Co substrates are different from those of films on Si(100) substrates. In general, the crystal structure of the substrate has a certain influence on the film nucleation and the relevant film structure, for example, orientation [10]. Okolo et al. [11] noted that the substrate type has marked influences on the texture of as-deposited Cu films. Similar results were also obtained in our present work as well. For polycrystalline films, surface evolution is often correlative with the texture. Several theoretical and experimental works have been devoted to this field. Paritosh and Srolovitz [12] applied simulation methods to demonstrate surface evolution such as roughness evolution is dependent on film texture. Therefore, surface evolution of thin films is influenced by the film microstructure which results from the effect of substrate type.

5.3.3 Correlation between surface roughness and texture coefficient for thicker films on various substrates

The micrographs of Figs. 5.7a-c compare the three-dimensional AFM surface image of thicker films (~4 µm) deposited on WC-Co, glass and silicon. The films deposited on WC-Co and glass are seen to be rougher than those deposited on Si substrates.

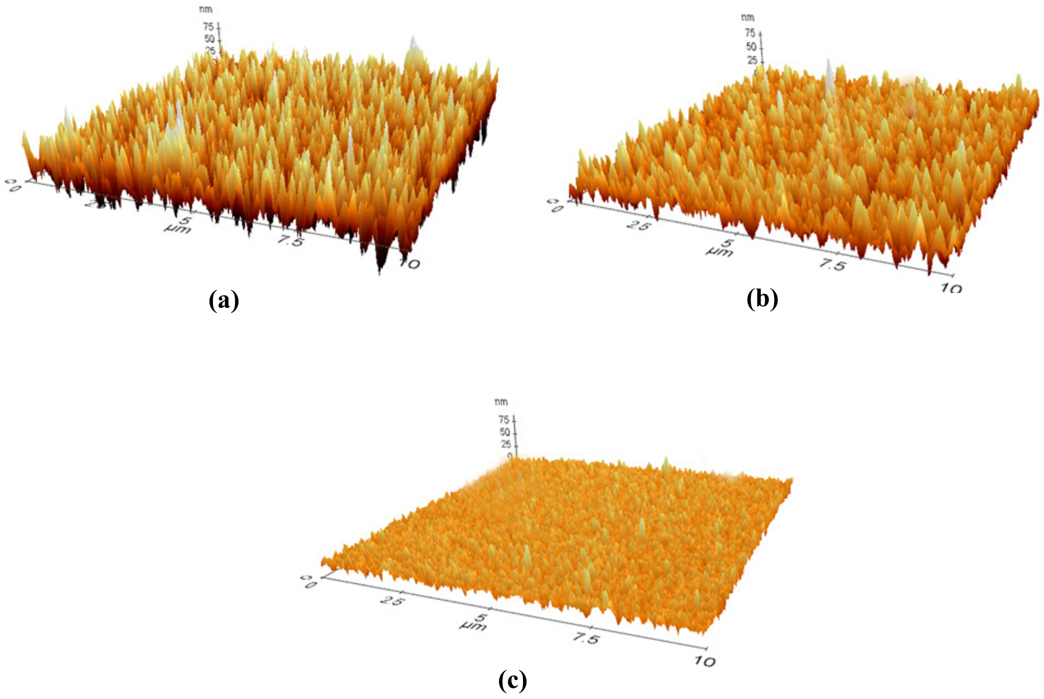

(a) (b)

(c)

Fig. 5.7: *AFM images of the surface morphology of $Ti_{0.5}Al_{0.5}N$ films deposited on various substrates at higher thicknesses t. a) t = 4.49 µm on WC-Co, b) t = 4.09 µm on glass and c) t = 4.32 µm on Si.*

The variations of the root mean square roughness (R_a) as a function of the film thickness are displayed shown in Fig. 5.8a. The roughness increases with film thickness on all three substrates, but it is higher on WC-Co and glass than on Si. Film roughness is strongly related to the preferred orientation. The relation between T(111) and R_a on all three substrates is depicted in Fig. 5.8b. It can be seen that increase in (111) texture coefficient on WC-Co and glass is accompanied by an increase in surface roughness. Thus the film roughness is in excellent correlation with film texture, indicating that it is determined by the crystal habit. Increase in T(111) is mainly related to the onset of competitive growth of crystals with preferred orientation [8]. Due to the competitive growth a considerable surface roughness develops. This results in the continuous change in morphology (Fig. 5.4) and texture as a function of film thickness.

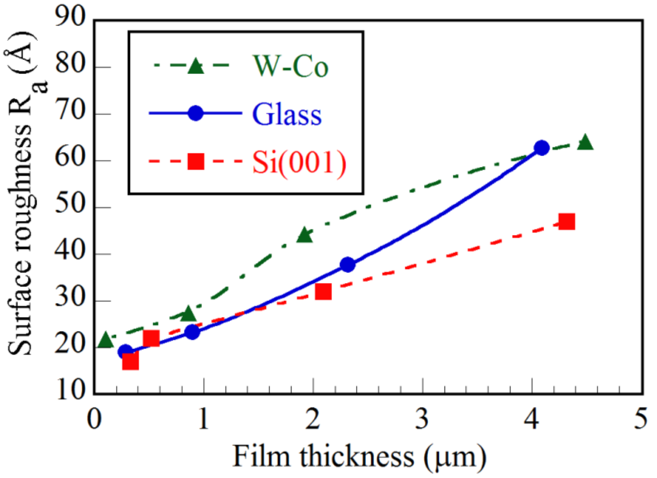

(a)

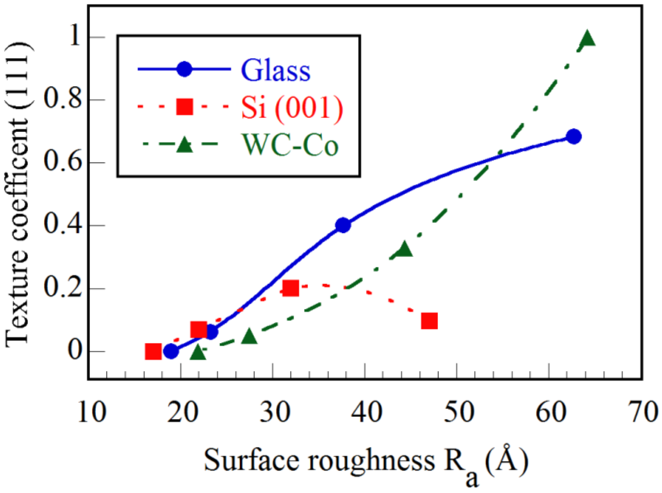

(b)

Fig. 5.8: *a) Variation of root mean squared roughness (R_a) with film thickness. b) Relation between film roughness and texture coefficients on various substrates.*

5.4 Microstructure and crystallite orientation study by TEM for $Ti_{0.5}Al_{0.5}N$ deposited on various substrates

5.4.1 Films on WC-Co

Fig. 5.9a corresponds to the bright field TEM image for a 4.49 µm thick film on WC-Co. One can clearly see a dense columnar structure, which agrees well with the zone T of the Thornton structure zone model [13]. There is no indication of extensive void networks along the column boundaries, although such voids have often been observed in films grown at relatively low temperatures [14]. The average column diameter increases with layer thickness. This indicates a continuous competition for growth among evolving columns [15].

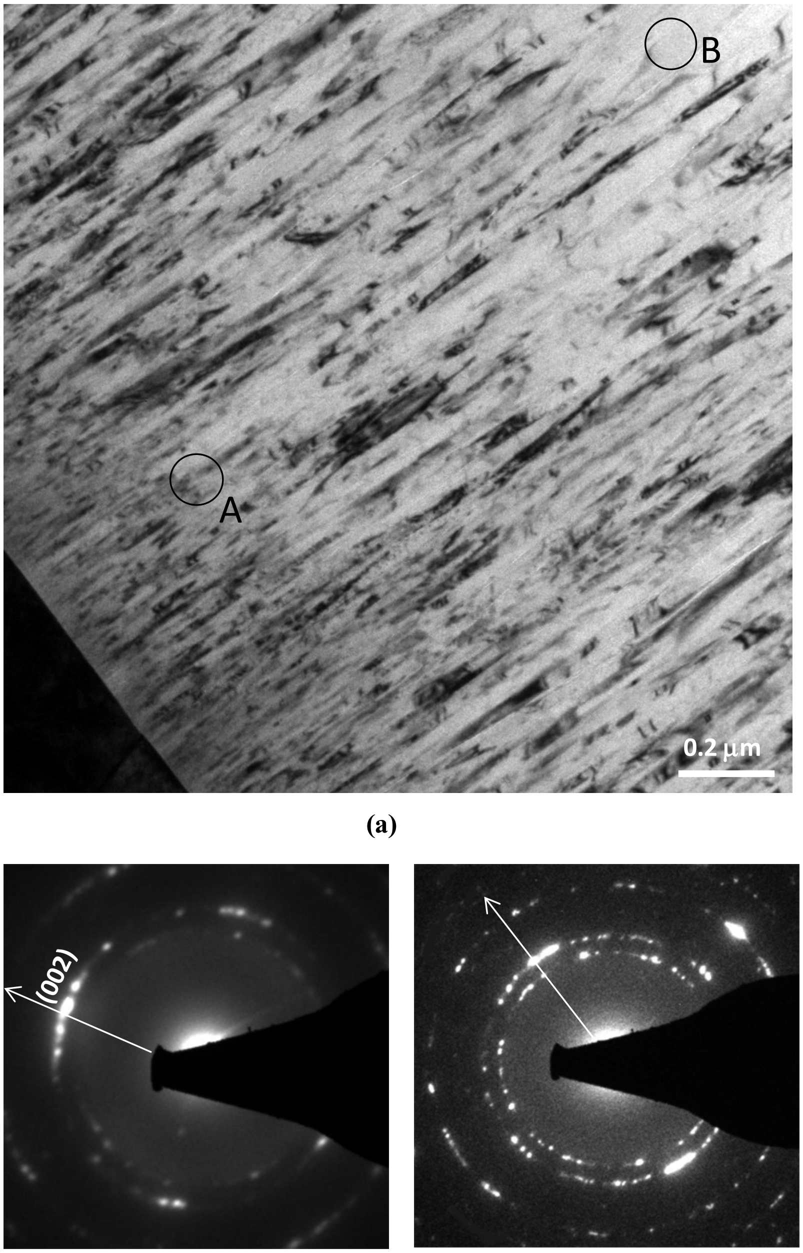

(a)

(b) **(c)**

Fig. 5.9: *Cross sectional TEM micrographs of a 4.9 µm thick film, (a) bright field image of* $Ti_{0.5}Al_{0.5}N$ *film showing the straight columnar structure, (b) SAED at low thickness featuring only (002) present, and (c) SAED at high thickness displaying both (002) and (111) present from region A and B, respectively. The arrows in the diffraction pattern indicate the direction of substrate normal corresponding to figure a.*

Figs. 5.9b and c display the selected area electron diffraction (SAED) patterns corresponding to low thickness (800 nm) and high thickness, respectively (2 µm). The SAED patterns resemble to B1 NaCl type $Ti_{1-x}Al_xN$ crystal with (111) and (002) reflections. The diffraction results obtained from region A demonstrate that only grains with (002) orientation are present during early stages of film growth. The (111) orientation develops gradually with increasing film thickness as shown in SAED patterns in Fig. 5.9c, region B (see also the XRD results in section 4.3.2, Fig. 4.7a). The discrete spots corresponding to the (002) reflection indicate that films at low thickness are (002) textured. The SAED pattern at higher thickness shows the presence of (111) reflections in addition to (002) reflections confirming the existence of mixed (111) and (002) orientations. These results are in complete agreement with the Bragg Brentano and pole figure XRD study (Figs. 4.7 and 4.9).

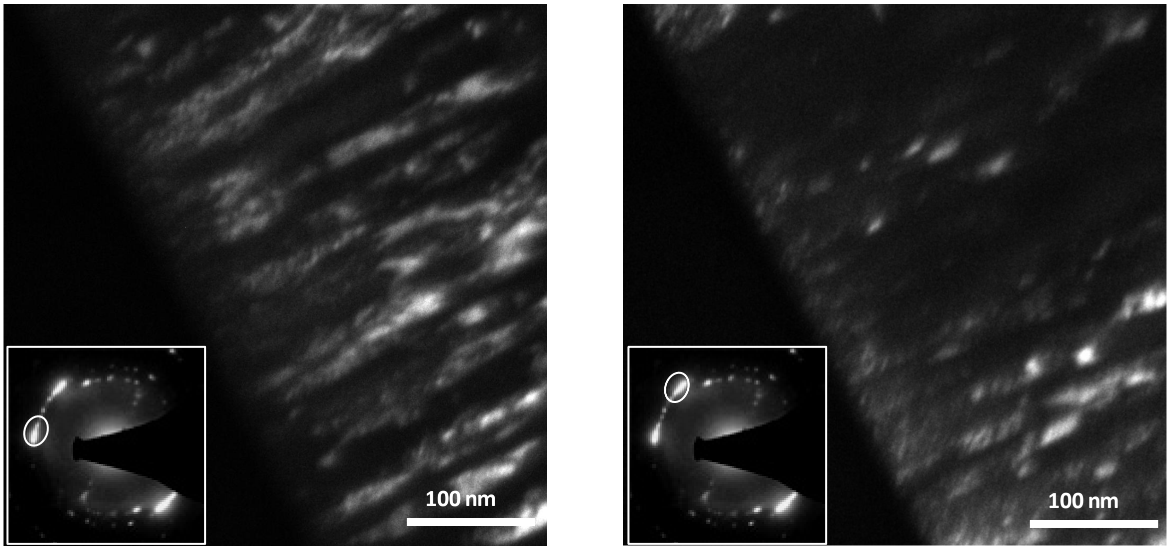

a) **b)**

Fig. 5.10: *Cross sectional dark field TEM images indicating film structures at low thickness close to the substrate. SAED patterns in (a) and (b) showing in-plane orientation of (002) crystallites.*

Depositions at higher substrate temperature leads to an increase in adatom mobility and hence larger initial nuclei with more homogenous size and with a higher probability of forming low energy boundary planes like (002). This is precisely what we have observed in the present experiments and in previous published results [14]. The SAED and dark field images at low thickness indicate that (002) orientation forms very early during nucleation and coalescence stages (Fig. 5.10)

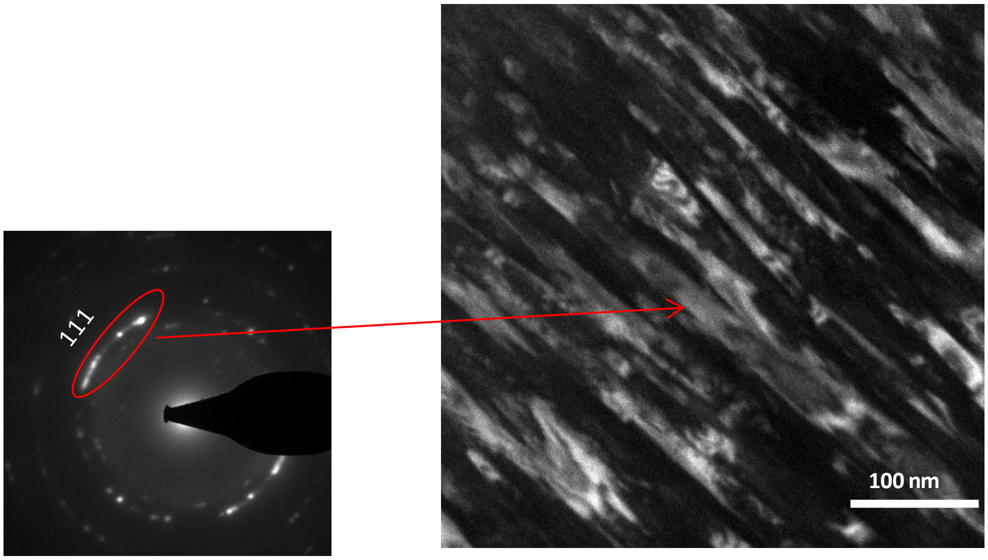

c)

Fig. 5.11: *Cross sectional dark field TEM images illustrating that the competitive growth is responsible for the gradual development of (111) orientation at higher thickness.*

The present TEM and diffraction results demonstrate that development of (111) orientation occurs after nucleation and island growth stages of film deposition. The TEM studies of microstructure evolution show that (111) orientation develops gradually through competitive growth. Thus the eventual emergence of higher-energy (111) surface is due to kinetic limitations rather than thermodynamic driving forces (Fig. 5.11).

5.4.2 Films on Si

TEM was employed to analyze the microstructure and crystallite evolution through the film thickness. The micrographs of Fig. 5.12 correspond to 4.32 μm thick film on Si. One can clearly notice a dense columnar structure, which agrees well with the zone T of the Thornton's structure zone model [13]. In addition, the average column diameter seems to be constant with film thickness (~40 nm). The film surface is rather smooth and the top region does not exhibit a faceted structure (Fig. 5.12).

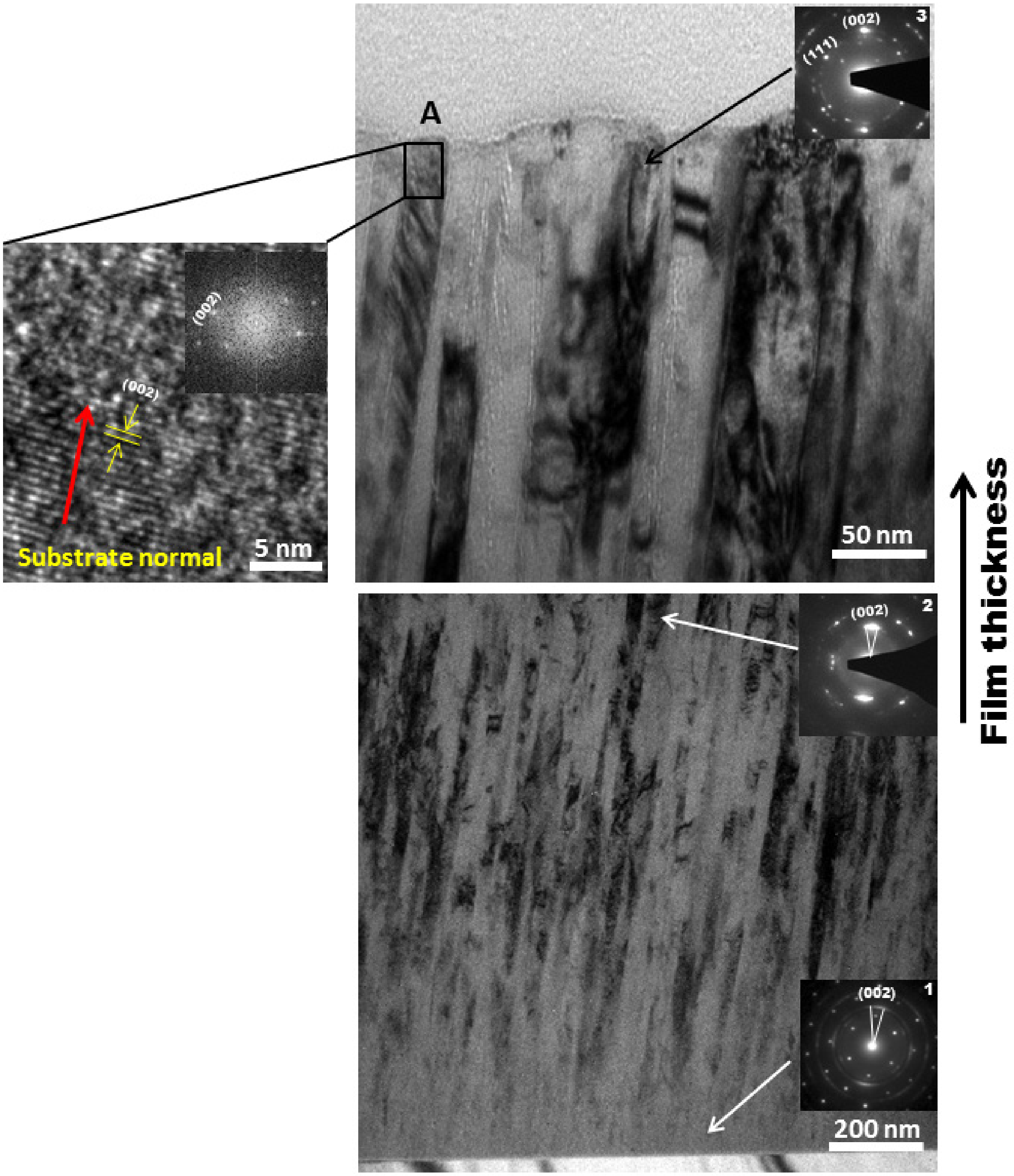

Fig. 5.12: *Cross-sectional TEM micrographs of 4.32 μm thick film on Si(100). Insets featuring the diffraction patterns corresponding to the evolution of (002) texture at various regions of film growth. HR image and FFT (inlay) from region (A) at the near surface region depicting the (002) planes are titled 8°-9° away from the film surface.*

The SAED patterns were taken at various thicknesses (interface, mid, top--see insets in Figs. 5.12). The first pattern (inset 1) is obtained from the interface giving superimposition of the typical pattern from the Si single crystal as well as the reflection of film displaying the (002), with a misalignment angle of about 8°. The second pattern (inset 2) corresponds to the center of the film, exhibiting an enhanced (002) reflections with a misalignment angle of around 5° which is indicative of improved crystallinity. Finally, the SAED pattern obtained at the surface of the film (inset 3) presents that the diffraction pattern approaches to that of a strongly textured TiAlN(002) along with some minor presence of (111). Consequently, although only the (002) orientation is present from the film-substrate interface up to the film surface, the texture and the crystalline quality become markedly improved as the films grew thicker. In order to better understand the growth process, high resolution TEM was used. The HR-TEM image near the film surface indicates that the (002) planes are tilted 8°-9° away from the surface which is in good agreement with the results obtained by the pole figure XRD (Fig. 4.6).

These observations confirm that the preferred orientation of $Ti_{0.5}Al_{0.5}N$ deposited on Si(100) at 650°C is mainly (002) with some off-axis orientation of around 8°-9°.

5.5 Variation of hardness with film thickness on different substrates

Although the chemical compositions and microstructures (crystal structure, crystalline size, orientation, and defects, etc.) are the determining factors of the mechanical properties, the mechanical performance of hard coatings is also strongly influenced by the thickness of coatings and the properties of the substrates on which the coatings are deposited. This influence has been theoretically acknowledged, but accurate and reliable data for quantitative analysis are still lacking because the high hardness and the micron-level thickness of coatings make the measurement of mechanical properties very difficult [16]. For instance, the reported hardness of TiAlN coatings ranges from 21–35 GPa and it is very difficult to distinguish the various influences on the mechanical properties of hard coatings [17-20]. This presents a great deal of trouble for the evaluation of mechanical properties and the control of the product quality of hard coating [16].

To obtain the hardness of the coating alone from the experimental measurements, several models exist in the literature [21-23].To separate the substrate effect from the measured hardness of composite (film + substrate) and estimate film only hardness, an analytical method proposed by Korsunsky et al. [23] was used in our study and expressed as follows:

$$H_c = H_s + \frac{H_f - H_s}{1 + k\beta^2} \qquad (5.1)$$

here, β is the relative indentation depth, H_f and H_s represent hardness of the film alone and the substrate respectively, parameters k is a dimensionless transition parameter.

5.5.1 Hardness studies for films on WC-Co

Fig. 5.13 displays the plot of film only hardness (H_f) and measured composite hardness (H_c) with film thickness. The film only H_f is greater than H_c because of the substrate being softer than the films. The difference between H_f and H_c decreases with increasing film thickness. The H_f is apparently close to measured H_c for thicker films due to the negligible substrate effect. Usually it is considered that when the film thickness is increased, stress relaxation takes place which causes a decrease in hardness [24]. However, contradictory results are obtained in our study. We attribute this enhancement of hardness with film thickness to the appearance of (111) texture for thicker films. The mechanical properties of the film are strongly related to its preferred orientation. The relation between hardness of the film and the texture of the film has been widely considered [25-27]. It has been reported that films with (111) orientation possess maximum hardness compared to films with other orientation [25,28]. Ljungcrantz et al. [29] in their studies on single crystal films showed that (111) is the hardest orientation in TiN due to the geometrical factor on the slip systems. In addition, Chou et al. [25] showed that the hardness does increase with increasing (111) texture coefficient in polycrystalline TiN films with (111) fiber texture. Fig. 5.14 features the plot of film only hardness (H_f) against (111) texture coefficient. From the figure, it can be seen that as the (111) texture coefficient is increased, H_f increases as well. Thus, one can consider that the trends of hardness and texture coefficient T(111) with respect to thickness are in very good agreement.

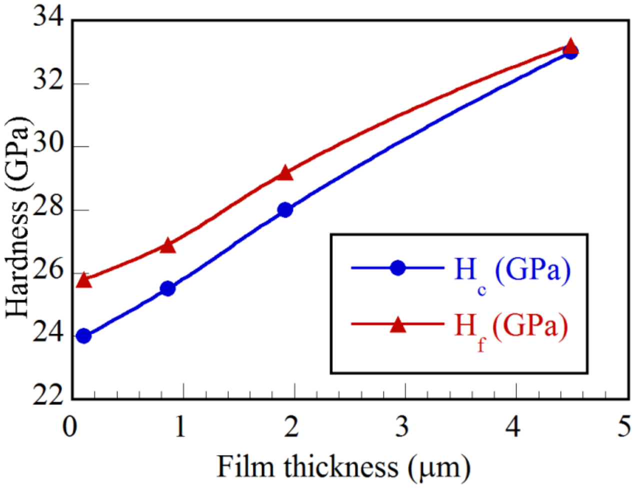

Fig. 5.13: *Variation of hardness with film thickness: measured H_c and H_f with film thickness. The effect of substrate was minimal for thicker films.*

Hardness increases from 25.8 to 33.2 GPa as the film thickness increases from 100 nm to 4.49 μm. This is related to the fact that (111) planes store more compressive stress, as shown in Fig. 5.1, as well as to the appearance of (111) texture. Several authors have reported that (111)-oriented films have higher levels of intrinsic stress and show enhanced hardness as measured by nanoindentation test [30,31]. In nitride thin films, <111> is the hardness orientation [32]. This increase in hardness can be explained by the relationship between (111) preferred orientation and the resolved shear stress on the slip systems of TiAlN. Since TiAlN has a NaCl-type structure, the active slip system of TiAlN is {110}<111>. If the external force is perpendicular to the (111) plane, the resolved shear stress on all the slip systems is zero. Consequently, it is very difficult to induce plastic deformation, and thus higher hardness is measured. Therefore, if the film possesses a highly (111) preferred orientation, its hardness is higher than those of other orientations.

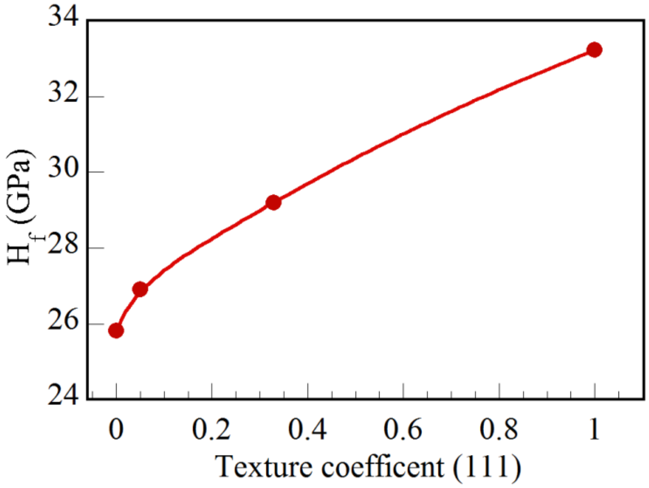

Fig. 5.14: *Correlation between* H$_f$ *versus* T*(111) texture coefficient.*

5.5.2 Hardness versus film thickness on Si

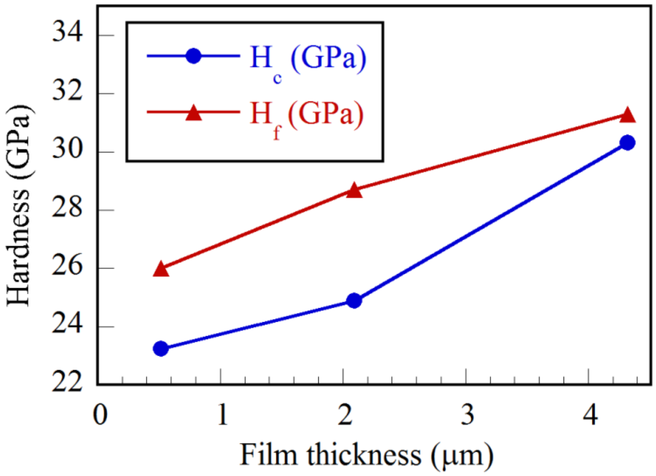

Fig. 5.15: *Composite hardness (H_c) and film only hardness (H_f) as a function of film thickness on Si.*

Similar trends for hardness values with thickness were also obtained from films on Si (Fig. 5.15). However, films deposited on WC-Co showed better hardness than on Si. We attribute this to the appearance of (111) texture and high compressive stress stored in (111) grains for films on deposited on WC-Co.

5.6 Summary of results obtained from this chapter

The obtained results clearly suggest interplay between preferred orientation and intrinsic stress with film thickness. For films on WC-Co, the intrinsic stress along (002) changes from compressive to tensile during film thickening due to the tilted <002> crystallites. Meanwhile, the stress state of grains having <111> orientation is compressive at higher thickness. In contrast for Si, the stress values along (002) remained compressive through the film thickness. SEM surface micrographs for films on WC-Co reveal that the development of (111) orientation is accompanied by an increase in surface roughness resulting in a faceted hill and valley surface. The TEM observations along with the SAED patterns support the XRD results for films on WC-Co and Si. Nanoindentation test reveal that the films deposited on WC-Co exhibit better hardness than those grown on Si.

5.7 Reference

[1] J. -D. Kamminga, Th. H. de Keijser, R. Delhez, E. J. Mittemeijer, J. Appl. Phys. 88 (2000) 6332.

[2] P. Scardia, Y. H. Donga, J. Mater. Sci. 16 (2001) 233.

[3] U. C. Oh, J. H. Je, J. Appl. Phys. 74 (1993) 1692.

[4] G. Abadias, Y. Y. Tse, Ph. Guérin, V. Pelosin, J. Appl. Phys. 99 (2006) 113519.

[5] W. Ensinger, Nucl. Instrum. Methods Phys. Res. Sect. B 106 (1995) 142.

[6] C. V. Falub, A. Karimi, M. Ante, W. Kalss, Surf. Coat. Technol. 201 (2007) 5891.

[7] J. H. Je, D. Y. Noh, H. K. Kim, K. S. Liang, J. Appl. Phys. 81 (1997) 6126.

[8] H. Köstenbauer, G. A. Fontalvo, M. Kapp, J. Keckes, C. Mitterer, Surf. Coat. Technol. 201 (2007) 4777.

[9] Y. Zhao, Y. Qian, W. Yu, Z. Chen, Thin Solid Films 286 (1996) 45.

[10] V. Randle, Texture. Microstruct. 14–18 (1991) 745.

[11] B. Okolo, P. Lamparter, U. Welzel, T. Wagner, E. Mittemeijer, Thin Solid Films 474 (2005) 50.

[12] F. Paritosh, D. J. Srolovitz, J. Appl. Phys. 89 (2001) 4857.

[13] J. A. Thornton, Annu. Rev. Mater. Sci., 7 (1977) 239.

[14] U. Helmersson, J. -E. Sundgren, J. E. Greene, J. Vac. Sci. Technol. A 4 (1986) 500.

[15] L. Hultman, G. Håkansson, U. Wahlström, J. -E. Sundgren, I. Petrov, F. Adibi, J. E.Greene, Thin Solid Films 205 (1991) 153.

[16] Z. Han, J. Tian, J. Lao, G. Li, J. Dai, J. Coating. Tech. Res. 1 (2004) 337.

[17] A. Santana, A. Karimi, V. H. Derflinger, A. Schütze, Mater. Sci. Eng. A 406 (2005) 11.

[18] H. C. Barshilia, M. Prakash, A. Jain, K. S. Rajam, Vacuum 77 (2005) 169.

[19] T. Yamazaki, Y. Okumura, K. Desaki, T. Kikuta, H. Anada, N. Nakatani, Vacuum 83 (2008) 479.

[20] G. Kim, S. Lee, J. Hah, Surf. Coat. Technol. 193 (2005) 213.

[21] A. K. Bhattacharya, W. D. Nix, Int. J. Sol Struct. 24 (1988) 1287.

[22] B. D. Fabes, W. C.Oliver, R. A. McKee, F. J. Walker, J. Mater. Res. 7 (1992) 3056.

[23] A. M. Korsunsky, M. R. McGurk, S. J. Bull, T. F. Page, Surf. Coat. Technol. 99 (1998) 171.

[24] K. D. Bouzakis, S. Hadjiyiannis, G. Skordaris, I. Mirisidis, N. Michailidis, K. Efstathiou, E. Pavlidou, G. Erkens, R. Cremer, S. Rambadt, I. Wirth, Surf. Coat. Technol.177 (2004) 657.

[25] W. J. Chou, G. P. Yu, J. H. Huang, Surf. Coat. Technol. 149 (2002) 7.

[26] C. T. Chen, Y. C. Song, G. P. Yu, J. H. Huang, J. Mater. Eng. Perform. 7 (1998) 324.

[27] H. M. Tung, J. H. Huang, D. G. Tsai, C. F. Ai, G. P. Yu, Mater. Sci. Eng. A, 500 (2009) 104.

[28] W. J. Chou, G. P. Yu, J. H. Huang, Surf. Coat. Technol. 140 (2001) 206.

[29] H. Ljungcrantz, M. Odén, L. Hultman, J. E. Greene, J. E. Sundgren, J. Appl. Phys., 80 (1996) 6725.

[30] J. Haifu, G. Chunzhi, T. Xiubo, Y. Shiqin, R. K. Y. Fu, P. K. Chu, Plasma Sci. Technol. 2 (2010) 212.

[31] P. Martin, A. Bendavid, T. Kinder, IEEE Trans. Plasma Sci. 25 (1997) 675.

[32] H. M. Tung, J. H. Huang, D. G. Tsai, C. F. Ai, G. P. Yu, Surf. Coat. Technol. 205 (2011) 2865.

Chapter 6:

Formation of (113) texture in titanium-rich $Ti_{1-x}Al_xN$

6.1 Overview of the present chapter

We have seen in Chapter 4 that for film composition of $Ti_{0.5}Al_{0.5}N$, the texture growth behavior reveals the off-axis alignment of (002) crystallites. In such a way, the <111> orientation remains parallel to the film normal through the film thickness. To characterize this off-normal behavior at different film compositions, we prepared series of $Ti_{0.67}Al_{0.33}N$ films on Si(100) and glass of various thicknesses, with same deposition parameters as given in chapter 4. Our choice was to increase the concentration of Ti since any further increment in Al would change the crystal structure from cubic to wurtzite [1,2], which is beyond the scope of the thesis. It was found that texture dynamic for $Ti_{0.67}Al_{0.33}N$ is similar to $Ti_{0.5}Al_{0.5}N$, but the final dominant orientation at higher thickness is (113) and not (111). Such behavior has been reported in literature in some cases [3-7]. Different mechanisms which are likely explain the crossover of (002), (111), and (113) orientations through film thickness are discussed. In addition, the development of the less dense (113) orientation is investigated with respect to stress, morphology, and mechanical properties.

6.2 Development of (113) preferred orientation observed by Bragg-Brentano θ–2θ scans

The θ–2θ scans for $Ti_{0.67}Al_{0.33}N$ films deposited on Si(100) substrates for various thickness are featured in Fig. 6.1a. For films of 500 nm and 1.3 μm thicknesses, the θ–2θ scans reveal only a dominant (002) out-of-plane orientation. When the film thickness reaches 2 μm, the (002) orientation still remains predominant, but some weak (111) signal can also be detected. As the thickness increases (3.4 μm), the crystallites reveal a strong (111) orientation along with a decrease in (002) peak intensity. However, for the same thickness, the (113) peak intensity becomes significant also. For 4.3 μm thick film, the peak intensity of (002) and (111) stay nearly constant. On the other hand, the (113) peak intensity manifests a drastic increase. Finally, for the 5.8 μm thick film, the θ–2θ scan reveals the presence of much weaker (002) and (111) reflections along with the existence of a strong (113) out-of-plane orientation.

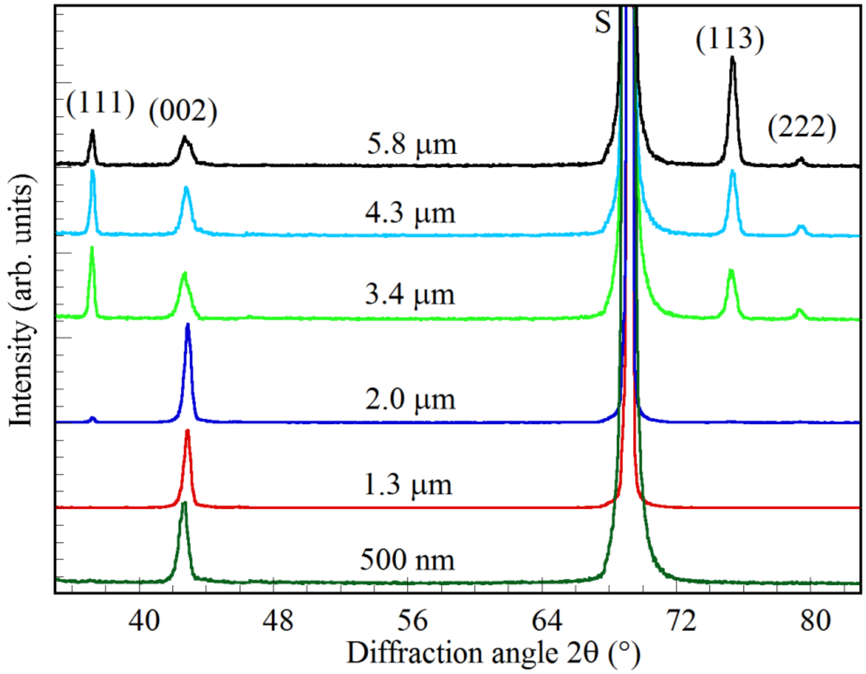

a)

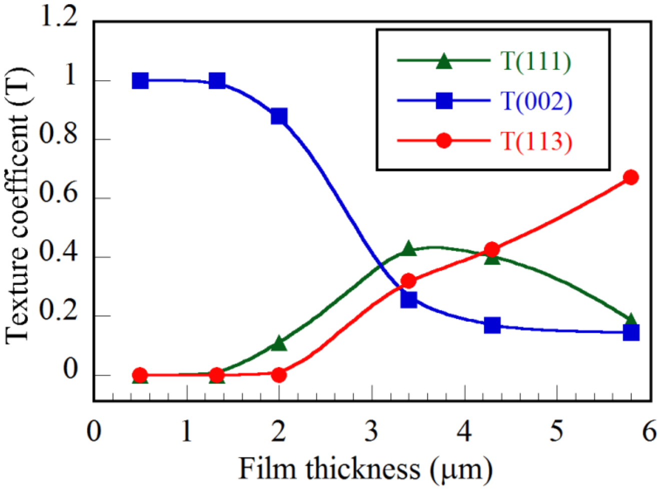

b)

Fig. 6.1: a) *θ–2θ scans of* $Ti_{0.67}Al_{0.33}N$ *films showing the development of (113) out-of-plane orientation with film thickness. The symbol S corresponds to Si substrate.* ***b)*** *The variation of texture coefficients for (111), (002) and (113) reflections obtained from θ–2θ scans over a range of film thickness.*

In order to gain a quantitative information about the evolution of film orientation, the texture coefficients were distilled from (002), (111), and (113) reflections as a function of film thickness (Fig. 6.1b). At low thickness up to 1.2 μm, only the (002) texture coefficient has been observed, which then decreases with film thickness. For films thicker than 1.2 µm, the T(111) shows an increase until the film thickness is around 3.3 µm, and afterwards a downturn of the coefficient value can be seen at higher thickness. On the other hand, T(113) which is initially zero at low thickness, begins to display a linear increase from 2 µm to 5.8 µm.

The growth of (002), (111), and (113) oriented grains calculated by the Scherrer formula [8] for films at various thicknesses is presented in Fig. 6.2. For low thickness values, small crystallites preferentially grow along the <002> direction. At an intermediate stage of the development of (111) oriented grains, the contribution of (002) grains decreases. Finally, the size of (113) orientation grains take over at higher thickness.

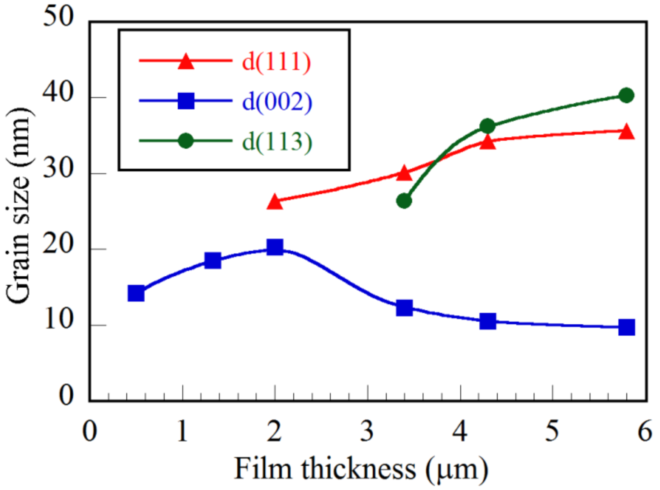

Fig. 6.2: *Comparison among grain sizes of different orientations as a function of film thickness. The plot reveals an increase in (113) grains along with the decrease in (002) grains during film thickening.*

In most of the texture studies on TiN and TiAlN thin films [9-18], it has been reported that preferred orientation at low thickness begins with (002) and ends up with (111) texture at higher thickness. In contrast, in our study, we observe that the preferential orientation at low thickness also grows in the <002> direction, which then switches to (111) at intermediate stages. However, for higher thicknesses, it is the (113) which is the dominant orientation observed. Using the pole figures XRD, we make an attempt to obtain more information on the crystallite orientation of these films.

6.3 Observation of (113) fiber texture using pole figure XRD

In contrast to θ–2θ scans, which provide information on the density of diffracting planes parallel to the substrate surface, the pole figures provide data on the statistical distribution of crystallites orientation within the coating since the sample is subjected to in-plane rotation at different azimuthal angles φ. Fig. 6.3 displays the pole figures for (111), (002), (022), and (113) reflections of selected samples of films for various thicknesses. The (113) pole figure for all the samples displays symmetric intense poles in a circular form at around $\psi \sim 40°$. These poles are diffracted from the Si substrate. The (113) Bragg position of $Ti_{1-x}Al_xN$ lies close to the tail of the (400) peak of Si which gives a superimposition of the film and substrate reflections, thus making the pole figure analysis of (113) difficult.

For a 1.3 μm thick film on Si(100), the (002) pole figure suggest that the (002) intensity is at the origin $\psi = 0°$ denoting that (002) planes are parallel to substrate surface (Fig. 6.3a). Meanwhile, the (111) pole figure is characterized by random distribution of reflections along with ring type intensities at $\psi = 54.5°$. This ring belongs to the family of (002) reflections as the interplanar angle between (111) and (002) is 54.7° for a cubic system. This indicates that (111) planes are not parallel to the surface. The (022) pole figure depicts a ring at around $\psi = 44.4°$ corresponding to (002) reflections in addition to some random intensities surrounding it. The (113) pole figure exhibits a weak ring 24.5° corresponding to (002) planes. Thus films deposited at this thickness range reveal a generic (002) fiber texture.

When the film thickness is increased to 2 μm, the (002) pole figure illustrates that (002) planes are still parallel to the surface (Fig. 6.3b). On the other hand, the (111) pole figure reveals a weak spot at $\psi = 0°$, indicating that (111) planes are now parallel to film surface, and a ring at $\psi = 54.4°$ belonging to (002) planes is also seen. The (022) pole figure displays a ring pattern $\psi = 45.4°$ showing the random in-plane orientation of (002) crystallites.

In case of 3.4 μm thick film, the (002) pole figure reveals weak intensities present at the center of the pole but majority of them are tilted to form a ring at $\psi = 21.5°$ (Fig. 6.3c). This ring formation is due to the two following effects: 1) tilting of (002) crystallites away from the surface, 2) diffraction of grains which have (113) planes parallel to the surface, since the interplanar angle between (002) and (113) is 25.1°. The Bragg position of the ring ($\psi = 21.5°$) is slightly less than the standard value reported (25.1°) probably due to the combination of these two above mentioned effects. Some weak intensities are also observed at $\psi = 72°$. The (111) pole figure now displays the (111) orientation is dominant at the origin. Moreover, the (111) pole figure reveals the (002) diffracted ring is collected at ψ = 53.7° and for (113) reflections at ψ = 30.4°. The (022) pole figure featured the (111) orientation and a weak ring at ψ = 31.4° and 63°, respectively corresponding to in-plane (113) crystallites. The (113) pole figure shows that the (113) planes are now parallel to the surface.

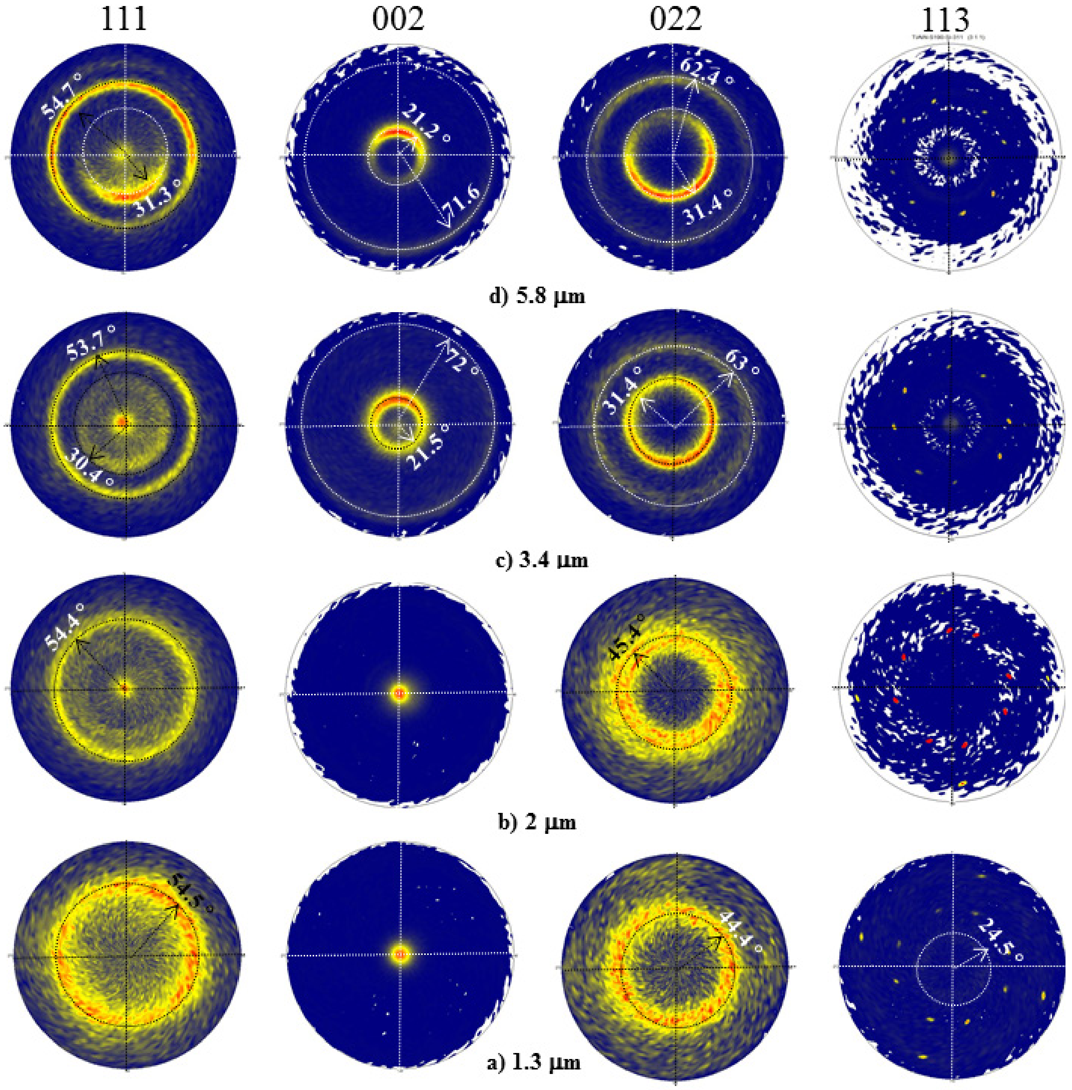

d) 5.8 µm

c) 3.4 µm

b) 2 µm

a) 1.3 µm

Fig. 6.3: *XRD pole figures for $Ti_{0.67}Al_{0.33}N$ coatings deposited on Si(100) measured around (111), (002), (022), and (113) planes showing the fibre texture change from (002) to (113) with film thickness (t), a) t = 1.3 µm, b) t = 2 µm, c) 3.4 µm, d) 5.8 µm. The intense spots observed in the (113) pole figure is due to the Si substrate effect.*

When film thickness is further raised up to 5.8 µm, one can notice a gradual decrease in the number of random reflections with film thickness. The (002) pole figure consist of a sharp ring at a polar angle of ~21.2° and weak ring at about 71.6° (Fig. 4d). The (111) pole figure reveals a weak <111> orientation parallel to film normal. An incomplete ring at $\psi = 31.3°$ corresponding to (113) and a ring at $\psi = 54.7°$ belonging to (002) diffracting planes are observed. The (022) pole figure presents a sharp ring at $\psi = 31.4°$ and weak ring at $\psi = 62.4°$. The (113) pole figure illustrates that the (113) texture is at the origin $\psi = 0°$. The pole figures thus indicate that films deposited at high thickness are dominating and present typical characteristics of (113) fiber texture.

6.4 Determination of stresses

Table 6.1 displays the intrinsic stress values $\sigma_{int}^{<111>}$ and $\sigma_{int}^{<002>}$ relative to the (111) and (002) orientation for various thicknesses. For 1.3 µm thick film, grains having <002> direction are compressively stressed with -4.22 GPa. When the thickness is reached to 4.3 µm, a decrease in the compressive stress state of (002) grains is noticed (-0.46 GPa). On the other hand, the stress state of grains having (111) orientation seems to be more compressive than (002) grains (Table 6.1). However, the values of stress in (111) grains are shown to decrease with film thickness. It is interesting to note that the stress relaxation in (111) crystallites occurs through change in crystallographic orientation and development of less dense (113) planes.

Thickness	$\sigma_{Int}^{<111>}$ **(GPa)**	$\sigma_{Int}^{<002>}$ **(GPa)**	**Dominant orientation**
1.3 µm	---	-4.22	(002)
3.4 µm	-5.89	-0.91	(111)
4.3 µm	-4.03	-0.46	(111) + (113)

Table 6.1: *Calculated stress in the coatings using* $\sin^2\psi$ *method. The table shows the dominant orientation and change in intrinsic stress along (111) and (002) orientation with film thickness.*

These obtained results are consistent with other authors who have also noticed similar behavior. For example, Chekour et al. [5] and Nouveau et al. [7] observed the preferential orientation of crystalline plane changes to (113) with film thickness for CrN films. This change in texture goes together with decrease in stress and film density.

6.5 Topography transformation with film thickness

Figs. 6.4a-d exhibit the surface morphology of $Ti_{0.67}Al_{0.33}N$ films on Si for various thicknesses. It can be seen that the surface morphology evolves continuously with thickness. At low thickness (1.3 µm), fine round grains corresponding to (002) orientation are observed (Fig. 6.4a). For a thickness of 2 µm, facets belonging to (111) grains begin to develop in addition to prevalent grains related to (002) (Fig. 6.4b). With further thickness increased to 3.4 µm, the films display a faceted (111) surface (Fig. 6.4c). Finally, for a 5.8 µm thick film, the surface shows a much pronounced facets of (113) with bigger grain size (Fig. 6.4d).

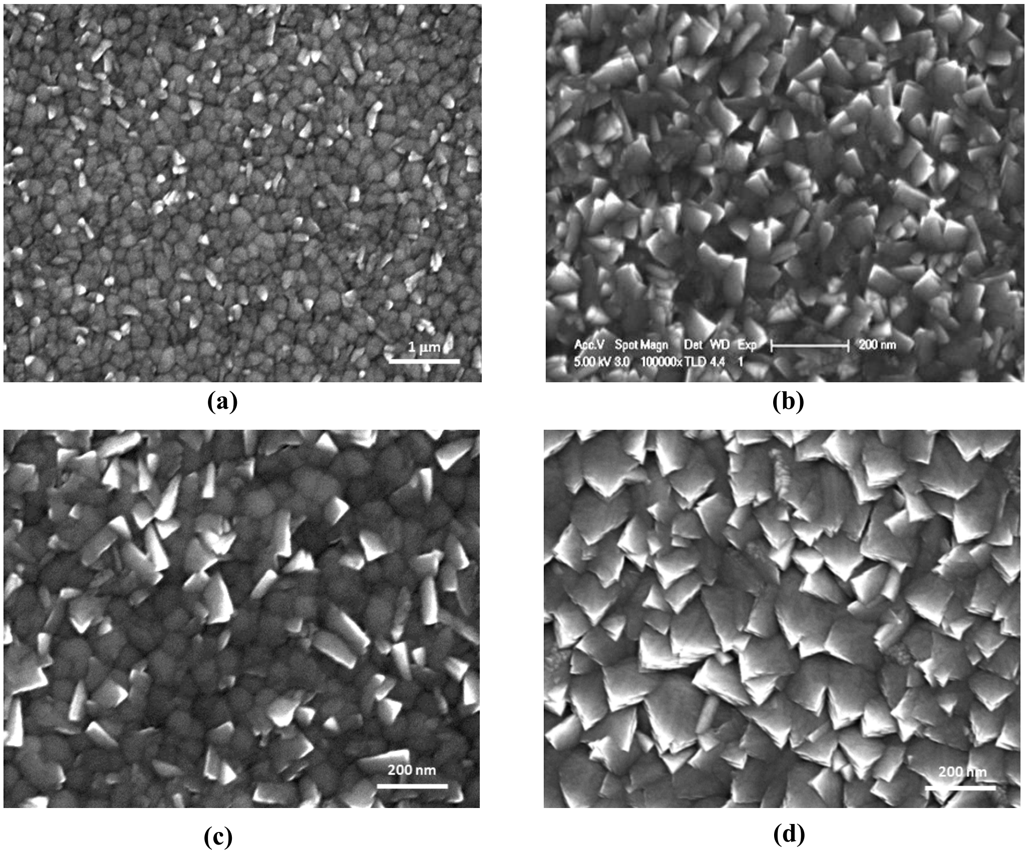

(a) **(b)**

(c) **(d)**

Fig. 6.4: *Surface morphology of $Ti_{0.67}Al_{0.33}N$ films deposited on Si(100) for various thicknesses. Grains of different orientations are seen during the film growth. SEM plane view for a) thickness $t = 1.3$ µm showing (002) grains, b) $t = 2$ µm indicating round and faceted (002) and (111), c) $t = 3.4$ µm featuring faceted (111) and d) $t = 5.8$ µm indicating grains of (113) orientation. The topography is seen to vary drastically with deposition time.*

The influence of thickness on the morphology of the films is evaluated by measuring the roughness of the samples. As a function of film thickness, the roughness is given in Fig. 6.5, and it clearly increases linearly with film thickness. The increase can be understood evoking the atomic shadowing effect theory. Namely, during the film growth some of the crystalline orientations can be more favoured than the others. In such a way, the increase in grain size occurs at the favoured orientation that leads to an increase in surface roughness.

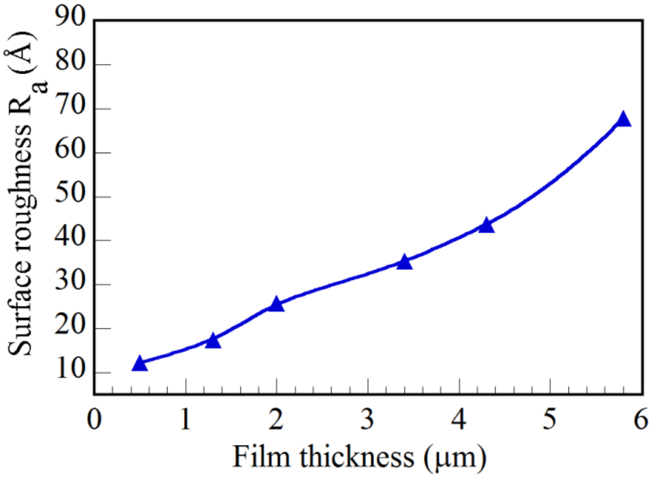

Fig. 6.5: *Effect of film thickness on surface roughness during the texture change.*

6.6 Hardness of (113)-oriented films

Fig. 6.6 presents the values of hardness as a function of film thickness. The hardness increases from 24.4 GPa to 27.2 GPa as thickness is varied from 500 nm to 3.4 µm. However, a drop in hardness is observed when thickness of the film is greater than 3.4 µm. There could be several reasons for this decline in hardness values. First is the high surface roughness for thick films. Another argument could the decrease in compressive stress with film thickness due to the development of less dense dominant (113) planes. (Table 6.1 and Fig. 6.1a).

As the film thickness increases, the surface becomes rougher due to the larger grain size (Figs. 6.2 and 6.5). Films with higher hardness have been reported in literature to have predominantly lower roughness values [19]. Similar results were obtained in our study. It is to note that surface roughness affects hardness measurements [20]. The surface roughness alters the contact between indentor tip and surface of sample and because of that bigger error appears in hardness values of thick films, as shown by error bars in Fig. 6.6. In literature, it is widely reported that hardness in TiAlN film is reduced when compressive stress is decreased [21]. In the current study comparable results were obtained. This apparent decrease in hardness is due to stress relaxation that occurs for thick films.

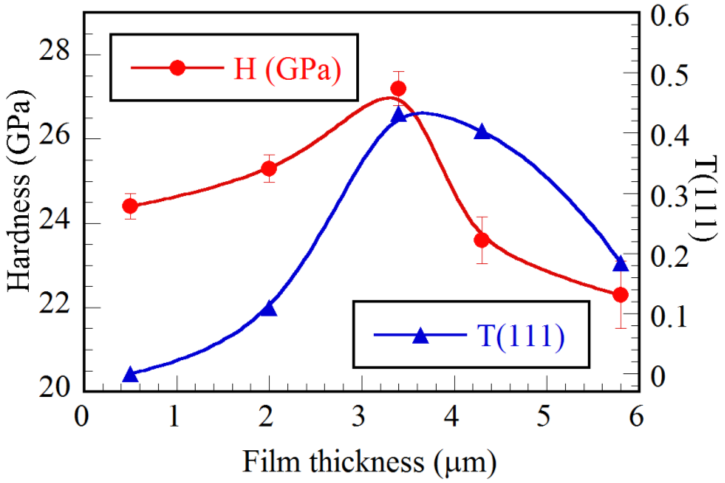

Fig. 6.6: *Interdependence between hardness and T(111) with increasing thickness.*

The interdependence of film hardness and T(111) coefficient as a function of film thickness is also shown in Fig. 6.6. It is well known that <111> is the hardest orientation in fcc nitride films [22]. It can also be seen that an increase in T(111) from 500 nm to 3.4 µm thick films corresponds to an increase in hardness as well. With further increase in film thickness, both H and T(111) decrease. Therefore, it can be concluded that the low hardness values for thicker films are due to the decrease in both T(111) coefficient as well as compressive stress and partially due to higher surface roughness.

6.7 Texture behavior on amorphous substrates

6.7.1 θ–2θ scans study with film thickness

Fig. 6.7a corresponds to the texture transformation of $Ti_{0.67}Al_{0.33}N$ films on glass studied by Bragg-Brentano configuration. The as-obtained XRD profiles are similar to films on Si (Fig. 6.1a). At 570 nm thick film, a strong (002) texture is seen. For a 1.2 µm thick film, a weak peak from (111) reflections appear in addition to dominant (002). Some minor presence of (113) grains is also seen for this film thickness. When the film thickness is further increased to 2.1 µm, the (002) peak intensity became saturated, while the (111) and (113) orientation showed a minor growth in peak intensity. At 4.1 µm thickness, the film reveals a decrease in (002) peak intensity, whereas both the (111) and (113) orientation display a rapid increase in intensities.

With the film thickness increased to 5.1 μm, the crystallites remarkably demonstrate a dominant (111) and (113) orientation along with a minor presence of (002) peak.

For films on Si, the thicker film (5.8 μm) indicates a dominant (113) out-of-plane orientation along with some minor presence of (111) and (002) (Fig. 6.1a). On the other hand, for glass (Fig.6.7b), we notice a significant presence of both (111) and (113) at higher thickness (5.1 μm). This apparent difference could be due to the difference in thickness of the two films. We assume that if the film thickness is further increased upon glass then one can eventually obtain the same result (i.e. dominant (113) orientation) as for films on Si.

The texture coefficients of (111), (002), and (113) planes calculated from XRD profiles are represented in Fig. 6.7b. For films on glass, the T(002), which is dominant at low thickness, showed a decreasing trend with film thickness. On the other hand, it can be seen that the crystallographic orientation shifts towards (111) and (113) at higher thickness. The results indicate that with increasing thickness, the preferential orientation growth switches to (113) plane for $Ti_{0.67}Al_{0.33}N$ films on glass.

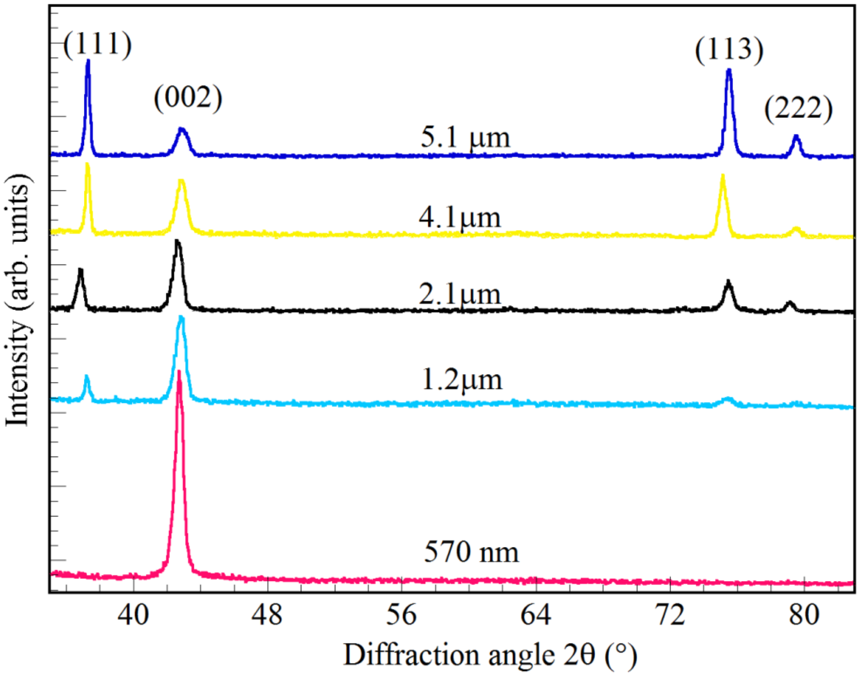

a)

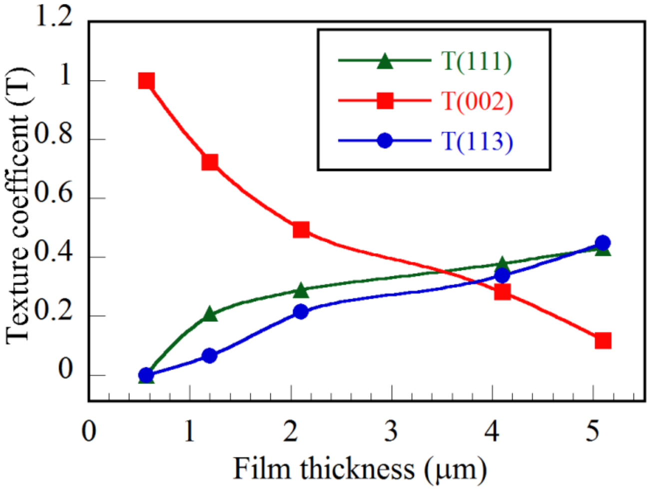

b)

Fig. 6.7: a) *θ–2θ XRD profiles of Ti*$_{0.67}$*Al*$_{0.33}$*N films on glass showing the change in preferential orientation with film thickness.* ***b)*** *Texture coefficients versus film thickness for (111), (002), and (113) reflections.*

The grain size for different orientations was analyzed by applying the Scherrer's equation [8]. Fig. 6.8 displays the evolution of crystal size calculated from $Ti_{0.67}Al_{0.33}N$ (111), (002), and (113) diffraction peaks with film thickness. In case of films deposited on glass, the (002) grains display a steady decrease in size with film thickness. Meanwhile, the share of both (111)- and (113)-oriented grains increase with film thickness.

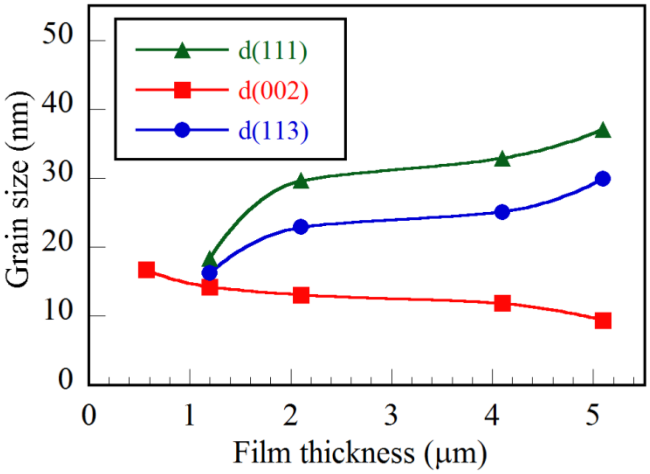

Fig. 6.8: *Grain size values relative to different orientations as a function of film thickness*

6.7.2 Pole figure XRD studies of (113) textured films on glass

The XRD pole figures for films on glass were collected for reflections (111), (002), (022), and (113) and presented in Fig. 6.9. The (002) pole figure for a 570 nm thick film features a strong (002) orientation with a majority of the reflections concentrated at the center of the pole (Fig. 6.9a). On the other hand for (111) pole figure, the diffracted intensity maxima is not located at the center of the pole but forms a ring at a diffraction angle of ψ = 54.4°. This ring corresponds to (002) planes. Similarly in case of the (022) pole figure, the diffracted intensity displays a ring pattern at ψ = 45.1°, which corresponds to the interplanar angle between (022) and (002) being 45°. The (113) pole figure depicts a ring at ψ = 24.1° belonging to the family of (002) planes.

When the film thickness is increased to 2.1 μm, the pole figure for (002) illustrates some weak intensities are present at the center of the pole, but majority of them are tilted to form a ring at ψ = 22.1° (Fig. 6.9b). This ring formation could be due to the combined effects of tilting of (002) crystallites and random in-plane orientation of (113) grains. The (111) pole figure reveals the development of <111> orientation parallel to film normal. A weak ring at ψ = 54° belonging to the family of (002) reflections is seen. The (022) pole figure can be considered consisting of two rings at ψ = 34.5° and 59.7° corresponding to (111) and (113) reflections, respectively. The pole figure for (113) on the other hand now reveals the development of (113) orientation at the origin along with two rings at ψ = 35.7° and 59.6°, both corresponding to (111) reflections.

Similar kind of ring formation was also noticed for films deposited on Si (Fig. 6.3d). However, it is interesting to understand the thickness at which this ring is observed. For films on glass, the ring is seen at 2 μm thickness. Contrastingly, for Si, the ring is noticed when film thickness is reached up to 3.4 μm. One possible explanation for early ring formation on glass could be due to the number of random reflections. Comparing Figs. 6.3 and 6.9, one can notice that the presence of random orientations is more in films on glass than on Si. These random reflections at low thickness might act as templates which are later aligned in an in-plane direction with film thickness, thus resulting in an early ring formation on glass. However, for depositions on Si, at low/intermediate thickness, the texture development may occur during the nucleation stage due to the substrate texture inheritance, resulting in films which have preferred orientation similar to that of substrate i.e (002). There are few random reflections observed as the films are strongly (002) fibre textured at low and intermediate thickness. This explains the delay in ring formation in the (002) pole figure.

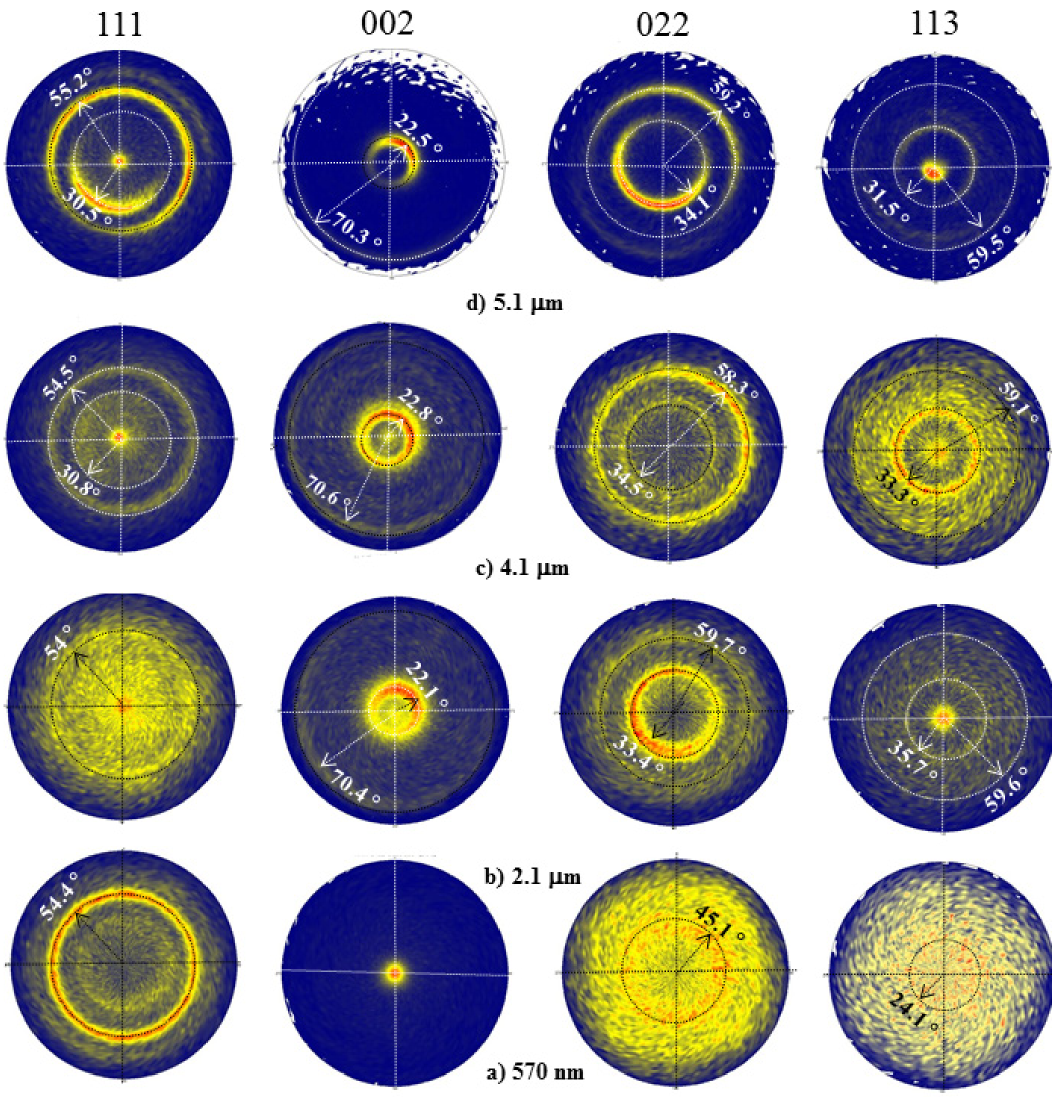

Fig. 6.9: *Pole figures analysis for (111), (002), (022), and (113) reflections of* $Ti_{0.67}Al_{0.33}N$ *films on glass deposited at various thicknesses.*

With the thickness further increased to 4.1 μm, the (002) pole figure reveals a ring at ψ = 22.8° (Fig. 6.9c). Some weak intensities are still seen at the origin indicating that some (002) planes are parallel to surface which is also confirmed by the θ–2θ scans (Fig. 6.7a). The (111) pole figure now features a well-developed <111> orientation parallel to film normal. The pole figure also reveals two weak rings of diffracted intensity at ψ = 30.8° corresponding to (113) reflections and at ψ = 54.5° corresponding to (002). The (022) pole figure also showed two sets of rings at ψ=34.5° and 58.3° belong to random in-plane orientation of (111) and (113) grains, respectively. The (113) pole figure exhibits that (113) reflections are concentrated at ψ = 0° along with a strong ring at ψ = 33.3° and a weak ring at 59.1°, indicating the in-plane orientation of (111) crystallites.

Finally for a 5.1 μm thick film, the (002) pole figure features a complete ring at ψ = 22.5° (Fig. 6.9d). The (111) pole figure depicts a strong pole at the center indicating a well-developed (111) orientation. An incomplete ring at ψ = 30.5° corresponding to family of (113) planes and a ring ψ = 55.2° belonging to (002) reflections are observed. The (022) pole figure displayed two rings at ψ = 34.1° corresponding to (111) and ψ = 59.2° corresponding to (113). Meanwhile the (113) pole figure reveals a concentrated (113) texture at the origin. In addition, a ring at ψ = 31.5° and a weak ring at ψ = 59.5° belonging to (111) are observed.

From θ-2θ scans and pole figures, we notice that films deposited on Si(100) and glass exhibit similar texture growth behaviour.

6.8 Summary of results obtained from this chapter

The crystallographic results indicate that (113) is the final dominant orientation on Si and glass that develops with film thickness for $Ti_{0.67}Al_{0.33}N$ films. This change in preferential orientation is accompanied with a transformation of morphology (increase in surface roughness) and a decrease in compressive stress that leads to a decline in hardness values. The formation of (113) orientation is in contrast to $Ti_{0.5}Al_{0.5}N$ films where the preferential orientation is (111) on glass whereas on Si a dominant (002) texture with film thickness is observed.

6.9 Reference

[1] M. Zhou, Y. Makino, M. Nose, K. Nogi, Thin Solid Films 339 (1999) 203.

[2] A. Horling, L. Hultman, M. Od´en, J. Sjolen, L. Karlsson, J. Vac. Sci. Technol. A 20 (2002) 1815.

[3] H. Wulff, A. Lunk, R. Basner, Vacuum 41 (1990) 2201.

[4] A. Karimi and W. Kalss, Surf. Coat. Technol. 202 (2008) 2241.

[5] L. Chekour, C. Nouveau, A. Chala, C. Labidi, N. Rouag, M. A. Djouadi, Surf. Coat. Technol. 200 (2005) 241.

[6] M. -A. Djouadi, C. Nouveau, O. Banakh, R. Sanjinés, F. Lévy, G. Nouet, Surf. Coat. Technol. 151-152 (2002) 510.

[7] C. Nouveau, M. A. Djouadi, O. Banakh, R. Sanjinés, F. Lévy, Thin Solid Films 398-399 (2001) 490.

[8] B. D. Cullity, Elements of X-ray Diffraction Addison-Wesley, Reading (1978).

[9] U. C. Oh, J. H. Je, J. Appl. Phys. 74 (1993) 1692.

[10] J. E. Greene, J. E. Sundgren, L. Hultman, I. Petrov, D. B. Bergstr, Appl. Phys. Lett. 67 (1995) 2928.

[11] M. Beckers, N. Schell, R. M. S. Martins, A. Mücklich, W. Möller, J. Appl. Phys. 98 (2005) 044901.

[12] Q. Li, S. Noda, H. Komiyama, T. Yamamoto, Y. Ikuhara, J. Vac. Sci. Technol. A, 21 (2003) 1717.

[13] D. S. Rickerby, A. M. Jones, B. A. Bellamy, Surf. Coat. Technol. 37 (1989) 111.

[14] T. Q. Li, S. Noda, Y. Tsuji, T. Ohsawa, H. Komiyama, J. Vac. Sci. Technol. A, 20 (2002) 583.

[15] N. Schell, W. Matz, J. Bøttiger, J. Chevallier, P. Kringhoj, J. Appl. Phys. 91 (2002) 2037.

[16] J. P. Zhao, X. Wang, Z. Y. Chen, S. Q. Yang, T. S. Shi, X. H. Liu, J. Phys. D, 30 (1997) 5.

[17] J. Pelleg, L. Z. Zevin, S. Lungo, N. Croitoru, Thin Solid Films 197 (1991) 117.

[18] A. R. Shetty, A. Karimi, Appl. Surf. Sci. 258 (2011) 1630.

[19] C. Carney, D. Durham, J. Vac. Sci. Technol. A 17 (1999) 2850.

[20] W.G. Jiang, J. J. Su, X.Q. Feng, Engng. Fract. Mech. 75 (2008) 4965.

[21] K. D. Bouzakis, S. Hadjiyiannis, G. Skordaris, I. Mirisidis, N. Michailidis, K. Efstathiou, E. Pavlidou, G. Erkens, R. Cremer, S. Rambadt, I. Wirth, Surf. Coat. Technol. 177 (2004) 657.

[22] H. M. Tung, J. H. Huang, D. G. Tsai, C. F. Ai, G. P. Yu, Surf. Coat. Technol. 205 (2011) 2865.

Chapter 7:

Texture formation under oblique angle deposition

7.1 Overview of the present chapter

In previous chapters, we have noticed the phenomena of off-axis texture under normal incidence deposition where the (002) planes are titled away while the <111> orientation is parallel to the film normal for fcc-$Ti_{0.5}Al_{0.5}N$ films. All the experiments were formed with ion flux angle arriving normal to the substrate (i.e α = 0°). The deposition angle α is defined as the angle sub-tended between the substrate normal and the incident vapor flux. In order to resolve whether the incident angle α plays any role in this off-axis texture formation, we have deposited series of $Ti_{0.5}Al_{0.5}N$ films under various incident angles from 0° to 60° on Si(100) substrates. All the films were deposited at room temperature with thickness of 2 μm. The as-obtained films were characterized for various properties such as crystallographic (θ–2θ, pole figure XRD), microstructure (SEM, TEM), and mechanical properties (nanoindentation). In this chapter, we demonstrate that films deposited under oblique angle deposition (OAD) display no inclined fiber texture. On the other hand, we notice that (111) planes are inclined towards the flux direction and <002> orientation is tilted away thus forming a biaxial texture.

7.2 Crystallographic orientation with deposition angle

7.2.1 θ–2θ scans study with incident flux angle

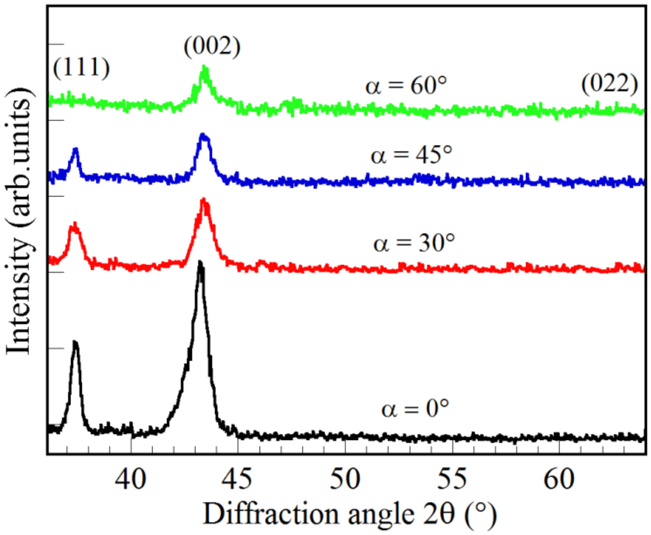

Fig. 7.1: *θ–2θ XRD profiles for $Ti_{0.5}Al_{0.5}N$ films deposited under various incident angles α = 0° to 60°. The figure reveals a reduction in (111) and (002) peak intensities with increasing α.*

The θ–2θ scans of $Ti_{0.5}Al_{0.5}N$ films having the same thickness deposited under various incident angles from $\alpha = 0°$ to $60°$ are featured in Fig. 7.1. Films deposited at $\alpha = 0°$ reveal a strong (111) and (002) out-of-plane orientation, suggesting that both the lattice planes are parallel to the substrate surface. This indicates that films deposited under normal incidence exhibit a mixed (111) and (002) preferred orientation. Increasing the incident angle above 0° causes a decrease in the intensity of (111) and (002) peak. Finally, at $\alpha = 60°$, the presence of a weak (002) peak is seen but the (111) peak is no longer visible. This indicates that the crystal orientation is changed with deposition angle. It can be expected that, due to the oblique angle flux, the <111> and <002> orientation of the $Ti_{0.5}Al_{0.5}N$ crystallites are no longer parallel to the film normal but tilted away and this explains the observed reduction of intensity at the Bragg angles.

7.2.2 Biaxial texture formation with flux angle

A sequence of pole figures for (111), (002), and (022) reflections for films deposited under various incident angles are displayed in Fig. 7.2. From an investigation of pole figures, it is clearly observed that (111), (002) and (022) pole distributions in an azimuthal and polar direction with an incident angle were far different.

Films deposited at an incident angle of 0° reveal a mixed (111) and (002) fiber texture, surrounded by random intensity distributions (Fig. 7.2a). There are two groups of reflections observed in the (111) pole figure. In the first group, the (111) diffracted intensity is at the center of the pole, illustrating that the (111) planes are parallel to the substrate surface and another group of reflection is in the form of a ring pattern at a diffraction angle of 54.3°. These reflections correspond to (002) planes as the interplanar angle between (111) and (002) is 54.7° for a cubic system. The (002) pole appears in a central zone, suggesting that the direction of <002> is parallel to the substrate normal. In case of (022) pole figure, the diffracted intensity is not located at the center of the pole, but is in the form of a ring that can be considered as consisting of 2 rings at a diffraction angle 34.2° and 46.1° corresponding to (111) and (002), respectively.

However, the (111) pole of the film deposited at an incidence angle of 30° is deflected with respect to the substrate normal, towards the incoming vapor direction at around 15.1° (Fig. 7.2b). The (111) tilt angle is the angle between the origin and (111) pole. This is somewhat near to the value predicted by the tangent rule $\tan\beta = \frac{1}{2} \tan\alpha$ ($\beta = 16.06°$). However, the development of in-plane texture is quite different. A limited in-plane alignment corresponding to (002) is observed at 56.8°. The (002) pole figure also exhibited an off-axis tilt but away from the direction of the deposition flux at around 20.7° (Fig. 7.2b). The (022) pole figure reveals two high intensity concentration regions at 32.7° and 32.1°, which coincide with the angular position of (111), indicating a strong (111) in-plane alignment. A very weak in-plane alignment of (002) is also seen at 60.1° and 60.5°.

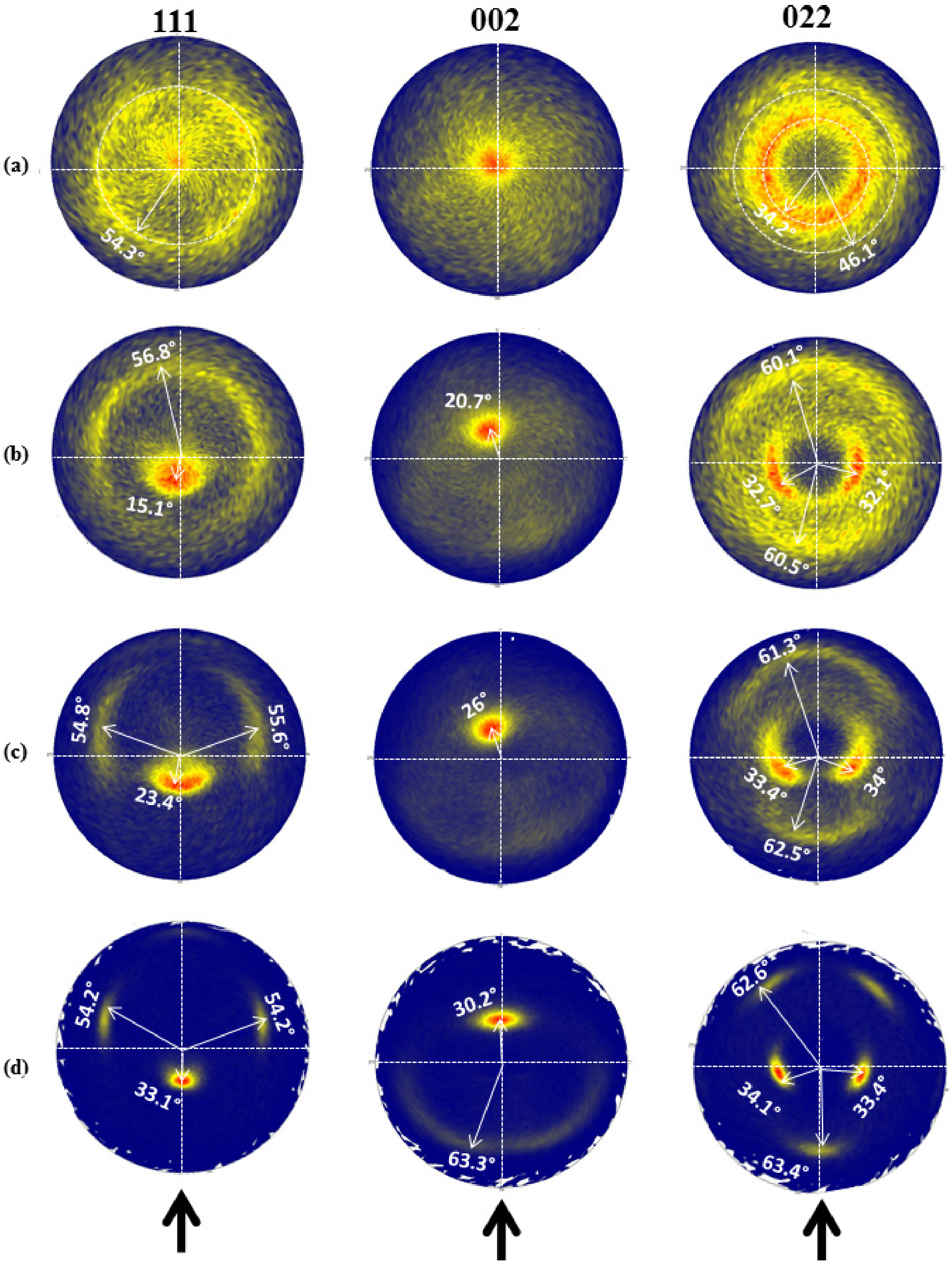

***Fig. 7.2**: XRD pole figures for (111), (002) and (022) reflections deposited at various incident angles of a) 0°, b) 30°, c) 45°, and d) 60°. The arrows indicate the direction of incident flux for figures b-d.*

The tilt of (111) texture increased further to 23.4° when the incident flux angle is increased to 45°. The (111) pole figure featured an improved in-plane alignment with two distinct intensity maxima at 54.8° and 55.6° corresponding to (002) (Fig. 7.2c). The (002) diffracted intensity maxima is seen tilted away from the vapor direction at around 26° as reported in Fig. 7.2c. The (022) pole figure depicts two group of planes for in-plane alignment. The first group has two distinct intensity maxima at Bragg angles 33.4° and 34° corresponding to (111) and other group at 61.3° and 62.5° belonging to the family of (002) reflections.

The pole figures demonstrates an improved in-plane alignment for films deposited under $\alpha = 60°$. In addition, the pole figures exhibit a decrease in random orientations with flux angle. It seems that the random distribution of reflections are biaxially aligned when $\alpha > 0°$. The (111) texture tilt angle from the substrate normal increased with the deposition angle towards the flux direction (33.1°, Fig. 7.2d). The (111) off-axis angles for OAD films are nearly close to β values obtained by the tangent rule. On the other hand, the tilt angle of (002) orientation is further moved away from the vapor direction to 30.2° for $\alpha = 60°$. There is also a weak in-plane alignment observed at 63.3° in the (002) pole figure (Fig. 7.2d). The (022) pole figure also demonstrated an improved in-plane alignment corresponding to (111) at Bragg angles 34.1°, 33.4° and for (002) at diffracted angles 62.6°, 63.4° when the deposition angle is varied from $\alpha = 45°$ to 60° (Figs. 7.2c and d).

Thus the nearly well-defined pole intensity concentration in the pole figure is a signature of bi-axial texture, i.e. it has not only an out-of-plane preferred orientation but also a clear in-plane preferred orientation. Increasing the flux angle α significantly changes the in-plane texture of the film.

7.3 Influence of flux angle on the microstructure

7.3.1 Topological modifications with variation in incidence angle

Changes in surface morphology of $Ti_{0.5}Al_{0.5}N$ films as a function of incident flux angles were investigated by scanning electron microscope (SEM). Fig. 7.3 corresponds to surface micrographs of films deposited under different flux angles α from 0° to 60°.

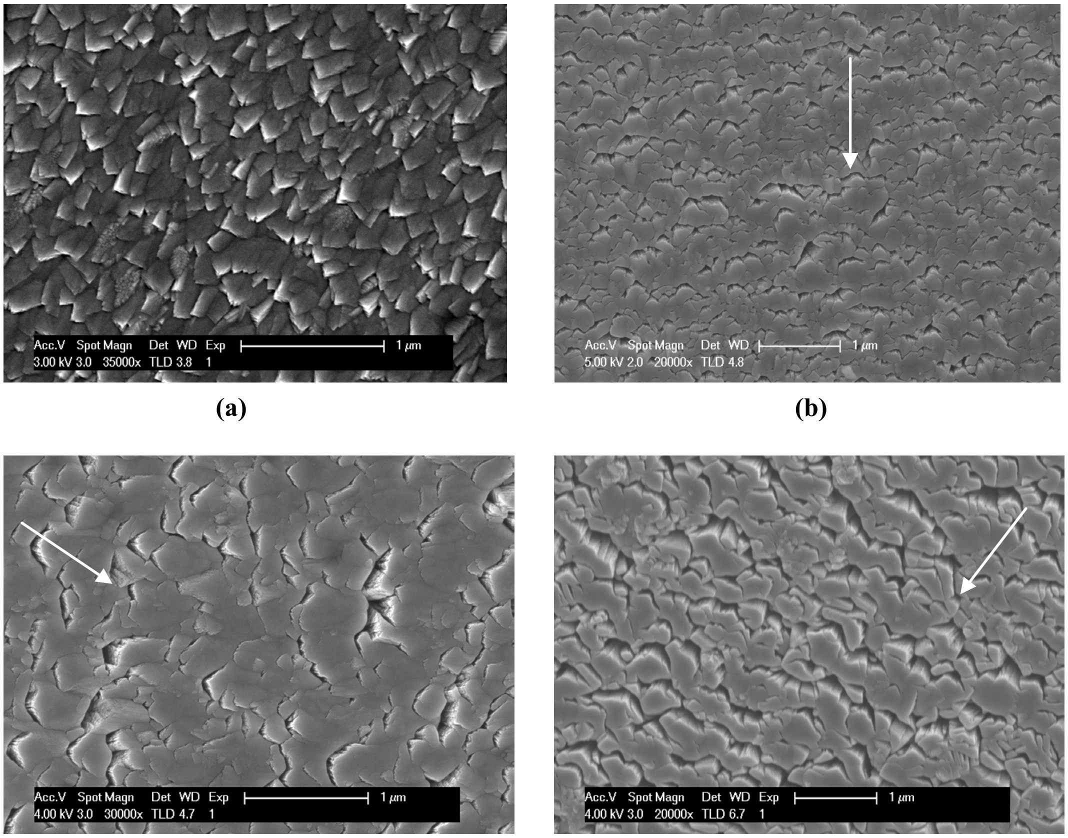

(a) **(b)**

(c) **(d)**

Fig. 7.3: *Top-view SEM images of the deposited* $Ti_{0.5}Al_{0.5}N$ *films on Si substrate at incident flux angles α: a) 0°, b) 30°, c) 45° and d) 60°. The arrows indicate the direction of incoming ion flux.*

Films deposited at α = 0° display a faceted crystallite structure (Fig. 7.3a). However, the surface morphology changes dramatically with the increase in flux angle α. “Roof-tile structure” or “stepwise structure” is seen on films, with no faceted crystallites when flux angle α is greater than 0° (Figs. 7.3b-d). Xu et al. [1] who deposited MgO films by inclined substrate deposition also observed a similar surface morphology and suggested a formation of a structure with in-plane and out-of-plane texture. Fig. 7.4 displays the surface morphology at higher magnification for film deposited under α = 45°. It can be seen that the incident flux arrives at oblique angles to the substrate causing atomic shadowing, which produces areas that incident flux cannot reach resulting in a voided microstructure (see Fig. 7.4) [2].

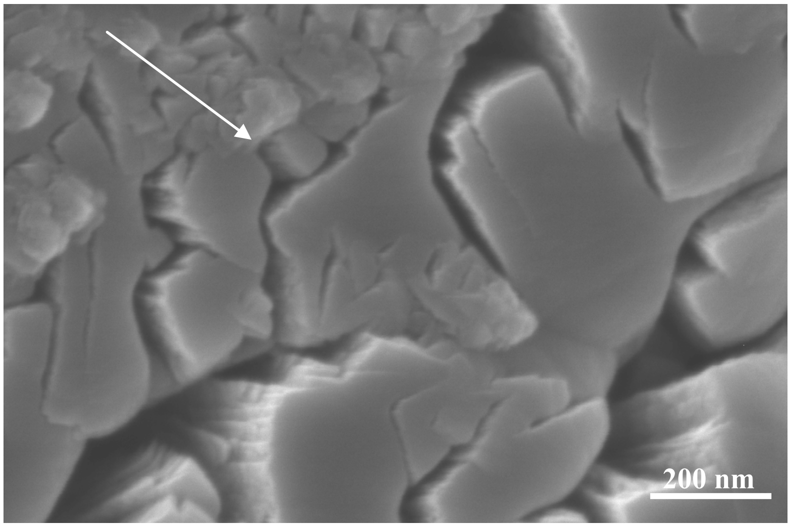

Fig. 7.4: *High magnification SEM image showing in detail the voids formed due to shadowing effects under oblique angle deposition (α = 45°).*

7.3.2 Cross-sectional morphologies with flux angle

The influence of incident flux angle on the columnar structure of the films is depicted in Figs. 7.5a-d. For films deposited by normal incidence (α = 0°), a distinct columnar structure consisting of thin columns is observed, which is in accordance with the zone 1 of the Thornton's structure zone model [3]. As seen for films deposited under normal incidence (see Fig. 7.5a), no tilt in the columns is observed. Tilted columnar structures towards the incoming ion flux are seen when depositions are made greater than 0° (Figs. 7.5b-d). These features are characteristics of the zone 1a of the extended structure zone model given by Mahieu et al. [4].

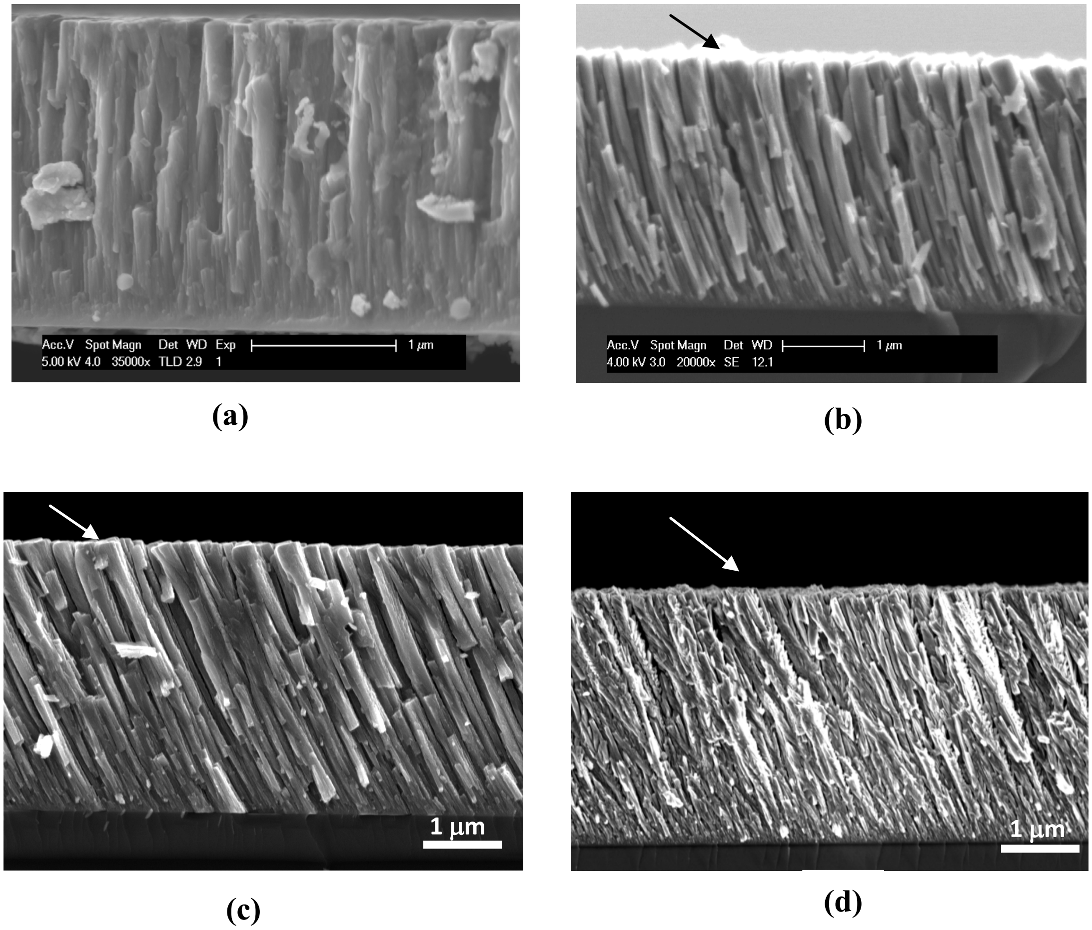

***Fig. 7.5:** Cross-sectional SEM images of $Ti_{0.5}Al_{0.5}N$ films deposited at different flux angles α; a) 0°, b) 30°, c) 45°, and d) 60°. Films deposited at $\alpha > 0°$ reveal that columns are inclined towards incident vapor direction*

A higher magnification image for one of the samples ($\alpha = 45°$) confirms the same, with tilted columns/bundles inclined towards the incident atoms with elongated voids (Fig. 7.6). As seen from Figs. 7.5c-d, if the flux angle α increases, the tilting of the columns also increases. It is well known that the flux angle α and the column angle β are not equal, because of the shadowing effects [5].The column angle (β), defined as the angle between the substrate surface normal and the long axis of the slanted columns, is measured from the cross-section SEM images. The SEM micrographs show that the columns are titled more in the direction of deposition flux when the incident flux α is varied from 0° to 60°.

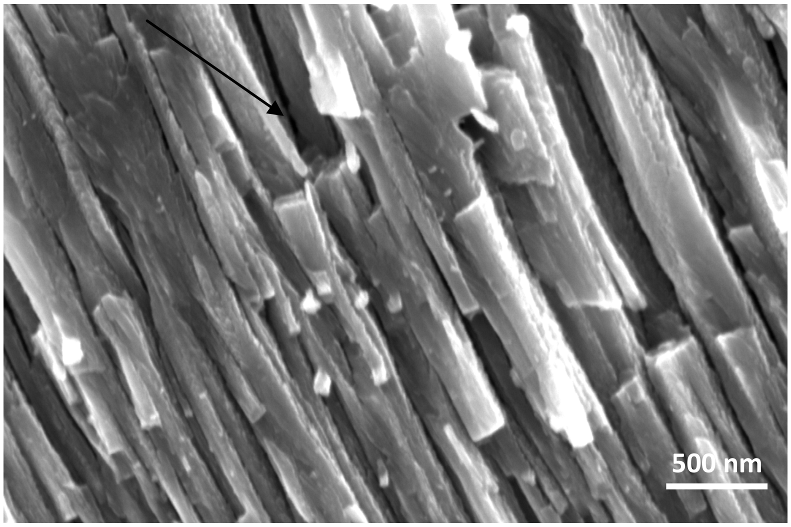

Fig. 7.6: *Higher magnification cross-sectional SEM micrograph showing in detail the voids between the inclined columns for depositions under α = 45°. The arrow indicates the direction of the flux.*

7.3.3 Crystallographic and microstructural characterization of nanocolumns

Fig. 7.7 displays the TEM cross-sectional view of the sample deposited at α = 30° and the corresponding selected area diffraction pattern (SAED) from the top region of a nanocolumn. The film exhibits a pronounced columnar microstructure separated by voided and porous intercolumnar boundaries. The columns are tilted towards the direction of the incident flux. This structure has the classic appearance of a zone 1a type film in the extended structure zone model by Mahieu et al. [4]. This voided growth structure is a fundamental consequence of atomic self-shadowing and its effect is maximized by an oblique deposition angle. As discussed in our previous section 7.2.2, the pole figures for films deposited at oblique angle reveal that (111) orientation is tilted towards the flux direction, whereas the (002) texture is titled away. This is confirmed by the SAED pattern for the top region as shown in Fig. 7.7. The diffraction pattern clearly indicates that (111) growth is in the direction of the incident flux and the (002) orientation is tilted away but close to the substrate normal. These scattered diffraction spots reveal that the crystallites have been reoriented. The nearly spot-like diffraction pattern indicates the presence of biaxial orientation which is also confirmed by pole figure analysis (Fig. 7.2).

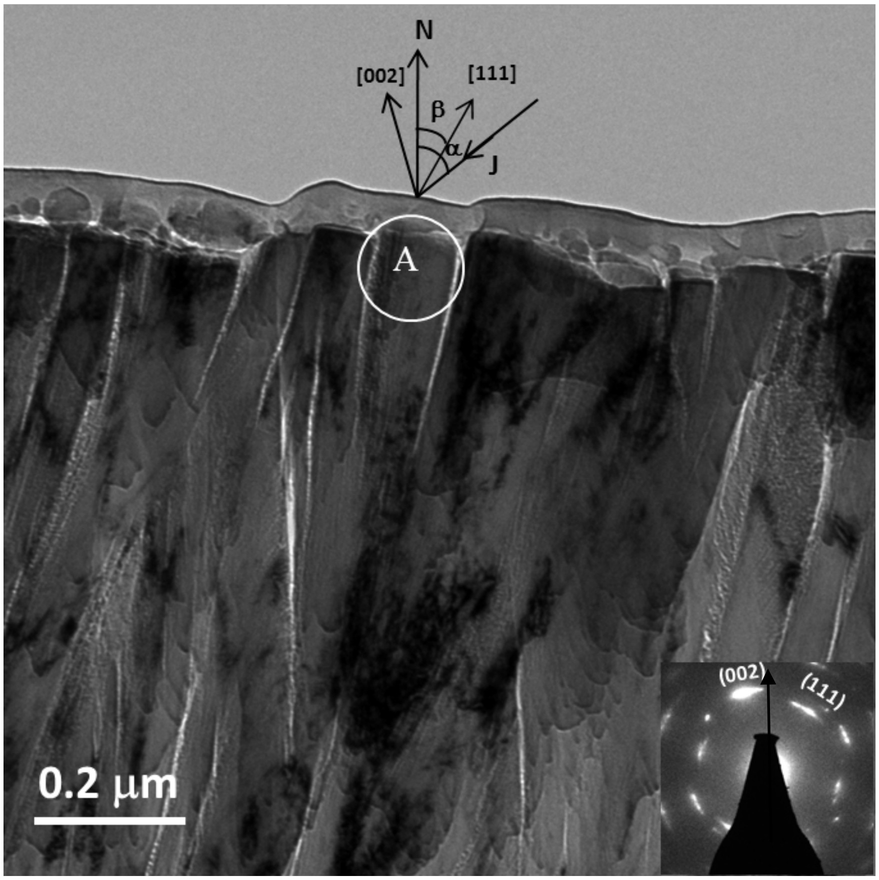

***Fig. 7.7**: Cross-sectional bright field image of the $Ti_{0.5}Al_{0.5}N$ film demonstrating the intercolumnar voids at oblique angle deposition of $\alpha = 30°$. The inset features the selected area diffraction pattern corresponding to circled area A of a nanocolumn, indicating the texture development. The arrow in the SAED pattern indicates the direction of film normal with respect to the bright field image. The symbol N is the substrate normal, J is the direction of the flux, α is the incident flux angle and β is the column angle.*

7.4 Relation between deposition angle, column angle, and texture tilt angle

It is accepted that there is a fixed relationship between flux angle α and column angle β for a given set of deposition conditions; the column angle β is uniquely determined by the choice of the deposition angle α [6]. This relationship is complex and poorly understood, although a number of attempts at understanding and quantifying this relationship have been presented.

The empirical ‘‘tangent rule’’[7] is a simple relationship based on near normal deposition and gives very poor results for α greater than about 50°.

$$\tan \beta = \tfrac{1}{2} \tan\alpha. \qquad (7.1)$$

A relationship by Tait et al.[8] based on geometrical analysis gives much better results for highly oblique angles (α large).

$$\beta = \alpha - \sin^{-1}[(1 - \cos\alpha)/2]. \qquad (7.2)$$

Lichter and Chen [9] proposed a more complex relationship between column angle β and incident angle α:

$$tan\beta = \frac{{}^{2}/_{3}\ tan\alpha}{(1 + \phi.tan\alpha.sin\alpha)} \qquad (7.3)$$

Xu et al. [1] proposed another expression, termed as “two-third relationship” given by:

$$\beta = \frac{2}{3}\alpha \qquad (7.4)$$

As studied previously by Nieuwenhuizen and Haanstra [7], Tait et al. [8], Lichter and Chen [9], and Xu et al. [1], the columns angle β is closely linked to the flux angle α and fits well with empirical functions. In Fig. 7.7, the experimental values of column angle β and (111) tilt angle obtained from the pole figure data are compared with the theoretical values, which are calculated from equations 7.1 to 7.4. Our observation regarding column angle β, (111) tilt angle and incident flux angle α is only based on the four above mentioned models. However, there are other models such as by Meakin [10] and Krug [11] which we have not discussed in this thesis. It is worthy to note that column angle β and (111) tilt angle fit better with the tangent rule for low deposition angle (α ≤ 45). For higher deposition angle (α ≥ 45°), all the models deviate from the experimental observations.

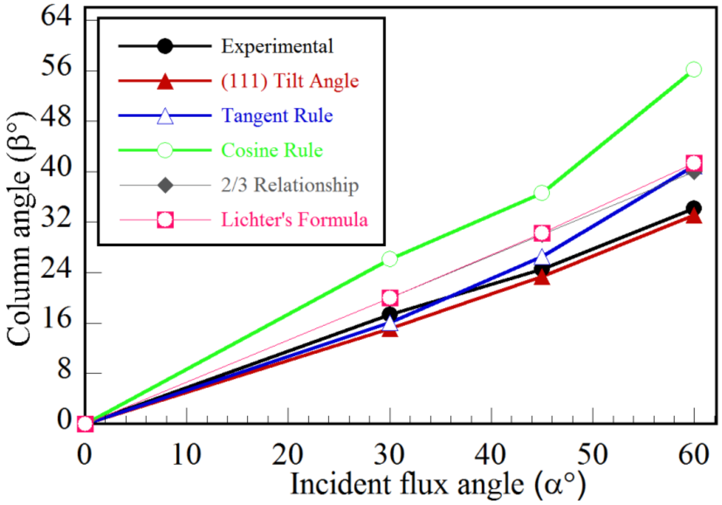

Fig. 7.8: *A comparison of the tilt angles predicted by different laws with the measured results.*

7.5 Variation of mechanical properties with column angle

A great influence of column angle on the mechanical properties of the coating was observed. Fig. 7.9 displays the variation of hardness (H) and Young's modulus (E) as a function of column angle β. The H and E are maximum for β = 0° and decreases when the column angle is increased. For β > 0°, the column angles became significant enough to modify the microstructure of the films. One can suppose that the noticeable decrease of H and E as *α* changes from 30 to 60°, mainly originates from a much more porous and voided structure of the films as shown in Figs. 7.3, 7.5, and 7.7. Since an oblique angle deposition *α* leads to inclined columns increasingly separated by elongated void network structures, the self-shadowing lateral effect is favoured and the overall mass density is decreased [12], thus leading to lower hardness and Young's modulus [13,14]. The voids reduce the amount of probed matter during the indentation and also decrease both hardness and modulus. Moreover, these voids alter the contact between the indentor tip and surface of sample. Because of that a somewhat bigger error occurs in hardness and Young's modulus values of films deposited under α > 0°, as shown with error bars in Fig.7.9.

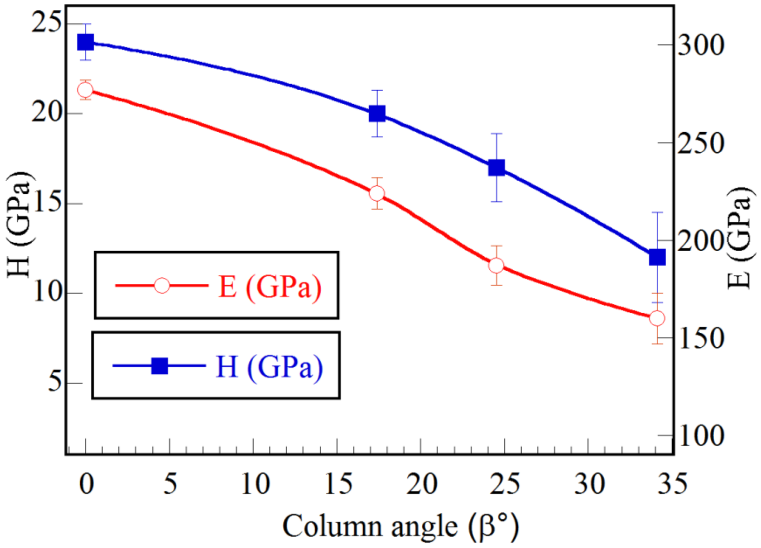

Fig. 7.9: Influence of column angle β on the hardness (H) and Young's modulus (E).

7.6 Summary of results obtained in the chapter

We have shown that the vapor incidence angle has great impact on the crystallographic orientation and morphology of the film. The texture of the films was analyzed by XRD and showed that under normal incidence (α = 0°) both the <111> and <002> orientations are parallel to film normal. On the other hand, for films deposited onto an inclined substrate, the (111) plane grows towards the flux direction whereas the <002> growth direction is tilted away from the deposition source but nearly parallel to the substrate normal, thus forming a biaxial texture. The surface morphology of obliquely deposited films exhibited a "roof-tile" or a "stepwise" shape, and a cross-sectional view showed a columnar structure tilted towards the incident flux direction. Both hardness and Young's modulus decreases when the flux angle changes from α = 0° to 60.

7.7 Reference

[1] Y. Xu, C. H. Lei, B. Ma, H. Evans, H. Efstathiadis, M. Rane, M. Massey, U. Balachandran, R. Bhattacharya, Supercond. Sci. Technol. 19 (2006) 835.

[2] S. Chen, Z. Li, Z. Zhang, Nanoscale Res Lett. 6 (2011) 326.

[3] J. A. Thornton, Annu. Rev. Mater. Sci. 7 (1977) 239.

[4] S. Mahieu, P. Ghekiere, D. Depla, R. De Gryse, Thin Solid Films 515 (2006) 1229.

[5] L. Chen, C. Chen, Y. Sung, Y Hsu, J. Electrochem. Soc. 156 (2009) H471-H474.

[6] K. Robbie, J. C. Sit, M. J. Brett, J. Vac. Sci. Technol. B 16 (1998) 1115.

[7] J. M. Nieuwenhuizen, H. B. Haanstra, Philips Tech. Rev. 27 (1966) 87.

[8] R. N. Tait, T. Smy, J. M. Brett, J Vac. Sci. Technol. A 10 (1992) 1518.

[9] S. Lichter, J. Chen, Phys. Rev. Lett. 56 (1986) 1396.

[10] P. Meakin, Phys. Rev. A 38 (1988) 994.

[11] J. Krug, Materialwissenschaft und Werkstofftechnik 22 (1995) 26.

[12] J. Lintymer, J. Gavoille, N. Martin, J. Takadoum, Surf. Coat. Technol. 174–175 (2003) 316.

[13] A. R. Shetty, A. Karimi, M. Cantoni, Thin Solid Films 519 (2011) 4262.

[14] A. R. Shetty, A. Karimi, Phys. Status Solidi (b) 249 (2012) 1531.

Chapter 8:

Effect of substrate temperature and other parameters on the texture and microstructure of films deposited under oblique angles

8.1 Overview of the current study

Most of the research work [1-5] on oblique angle deposition (OAD) is carried out at considerably low temperature (room temperature (RT)). In Chapter 7, the effect of flux angle on the texture, microstructure, and mechanical properties of $Ti_{0.5}Al_{0.5}N$ films was examined at RT. However, in this chapter, the influence of substrate temperature on texture growth of obliquely deposited $Ti_{0.5}Al_{0.5}N$ films will be discussed. The films were deposited at 200°C, 400°C and 650°C on Si. Consequently, when the substrate temperature is elevated from RT to the above-mentioned temperatures, due to the enhanced mobility of the adatoms, the surface diffusion length is likely to overrule the self-shadowing effects in traditional OAD at ambient temperature. The mobility affects the angle of columns, off-axis angles of (111) and (002) texture as well as the microstructure and mechanical properties of the coatings that will be studied in this chapter. In addition, we also demonstrate that the biaxial alignment and inclination of columns is independent of film composition.

8.2 Effect of deposition temperature on the crystallographic orientation of obliquely deposited films

8.2.1 Out-of-plane texture with substrate temperature

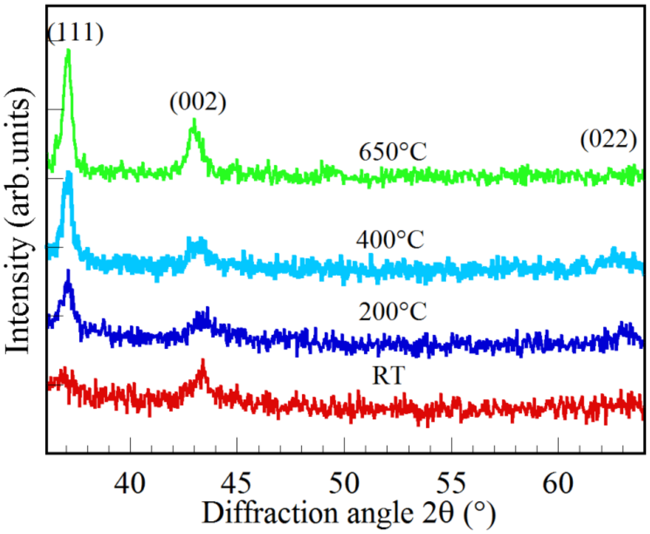

Fig. 8.1: *θ-2θ XRD scans for* $Ti_{0.5}Al_{0.5}N$ *showing the elevation of (111) and (002) out-of-plane orientation with deposition temperature for films deposited under* $\alpha = 45°$.

The θ-2θ XRD line profiles for films deposited at α = 45° with increasing substrate temperature are displayed in Fig. 8.1. Films deposited at RT exhibit very weak signals from (111) and (002) reflections. However, the plot points out that there is some increase in peak intensities at (111) and (002) Bragg positions when the deposition temperature is raised from RT to 650°C. During the increase in deposition temperature, adatoms can gain momentum and this leads to an increase in mobilities of the adatoms on the film surface, which improves the crystallinity and results in the (111) and (002) planes to approach almost parallel to the substrate surface.

8.2.2 Weakening of biaxial texture with enhanced adatom mobility

In section 8.2.1, it was determined that the $Ti_{0.5}Al_{0.5}N$ films deposited under oblique angles display enhanced preferential out of plane orientation with deposition temperature. To understand whether these films are biaxially oriented (having both out-of-plane and in-plane alignments), we conducted X-ray pole figure measurements. Fig. 8.2 corresponds to the pole figures of (111), (002), and (022) diffraction peaks for various temperatures deposited at α = 45°. The pole figures for films deposited at RT exhibit a well-defined biaxial texture (Fig. 8.2a). The (111) pole figure reveals a concentrated (111) pole tilted towards the direction of ion flux at ψ = 23.4° from the center. The presence of two diffracted intensity maxima regions at ψ = 54.8° and 55.6° indicate the in-plane orientation of (002). Meanwhile, the <002> crystallographic direction is tilted 26° away from the deposition source. The presences of strong intensity poles concentrated at specific regions, which match with the angular positions of (111) and (002), demonstrate that there is a clear in-plane orientation as observed in the (022) pole figure. Thus films deposited at RT exhibit sharp concentrated poles in the pole figures with no random reflections which is a characteristic feature of biaxial films.

When the substrate temperature is raised up to 400°C, the (111) pole is no longer concentrated but slightly diffused thus becoming larger and less intense and starts to move towards the origin by 20.7°. From Fig. 8.2b, it can also be seen that the <002> direction is inclined back to 23.7° towards the center. The (022) pole figure reveals that the concentrated regions of (111) become more enlarged with less intensity and move rather close to each other along with the weakening of in-plane orientation belonging to (002) at ψ = 62.5° and 64.2°. In addition to this, at this temperature range, the pole figures also display a rise in the degree of random orientations.

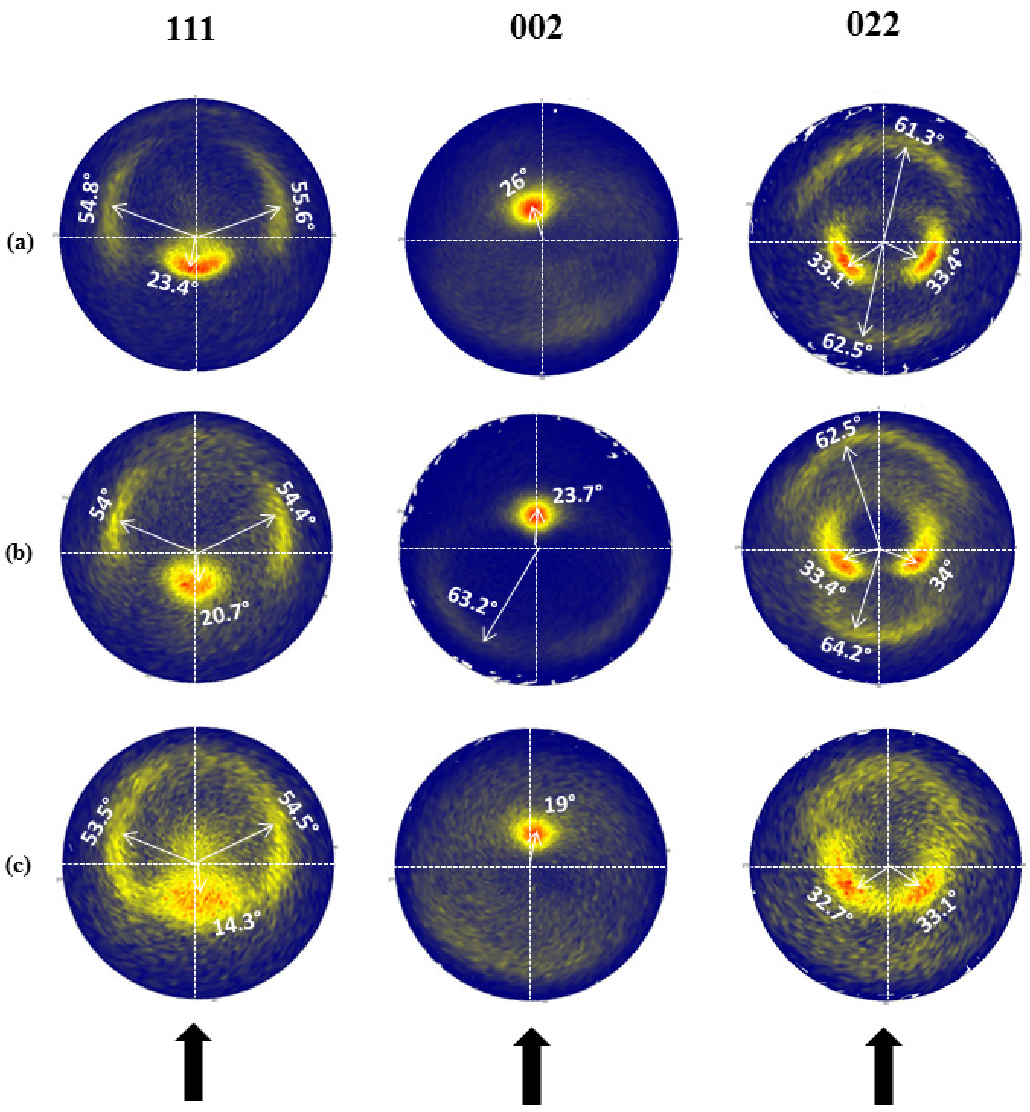

Fig. 8.2: *The pole figures of* $Ti_{0.5}Al_{0.5}N$ *for (111), (002), and (002) reflections deposited at* $\alpha = 45°$ *with increasing temperature: a) RT b) 400°C, and c) 650°C. The biaxial texture is seen to wane at higher temperatures. The arrows indicate the direction of incident flux.*

The pole figure plots for films at 650°C display a loss of consistent orientation. The (111) and (002) poles are no longer concentrated but diffused at this temperature range. In addition, the crystallites which were biaxially aligned at room temperature now display random orientations with increasing temperature. The films display a near complete collapse of biaxial texture with the <111> and <002> directions both approaching the surface normal at 14.3° and 19°, respectively (Fig. 8.2c). This is also confirmed by the increase in (111) and (002) peak intensities as observed in the θ-2θ scans made for the same sample (Fig. 8.1, 650°C). The (111) pole is no longer concentrated but scattered reflections are seen near the center of the pole. The in-plane texture corresponding to (002) seems to have become more random at higher substrate temperature. The (002) pole is seen to be surrounded by random intensity distributions. The (022) pole figure shows the potential merge between two (111) biaxial texture poles that forms a fiber texture of random in-plane alignment. However, in the same pole figure, the (002) reflections are seen to be completely scattered. Thus for films deposited at higher substrate temperature under oblique angles, more random distributions appear which may acts like a template for fiber texture formation.

These observations are consistent with earlier reports [6,7] that a lowered substrate temperature exhibits an improved in-plane texture. With increasing deposition temperature, the pole figure analysis indicates that the preferential alignment of <111> and <002> growth direction is perpendicular to the substrate surface. When films are grown at sufficiently higher substrate temperatures, the grains gain more energy for greater mobility on the surface. Each individual grain is able to align its growth direction close to the normal of the substrate [8]. Still, as the substrate temperature is increased from RT to 650°C, the in-plane texture began to decline due to the enhancement of surface diffusion which results in the appearance of random reflections.

8.3 Transition from porous to dense microstructure with deposition temperature

We report a detailed SEM analysis to study the effect of substrate temperature on the column angle and surface morphology of films deposited under oblique angle deposition. Fig. 8.3 illustrates the top view and cross-section of films deposited under $\alpha = 45°$ at various temperatures.

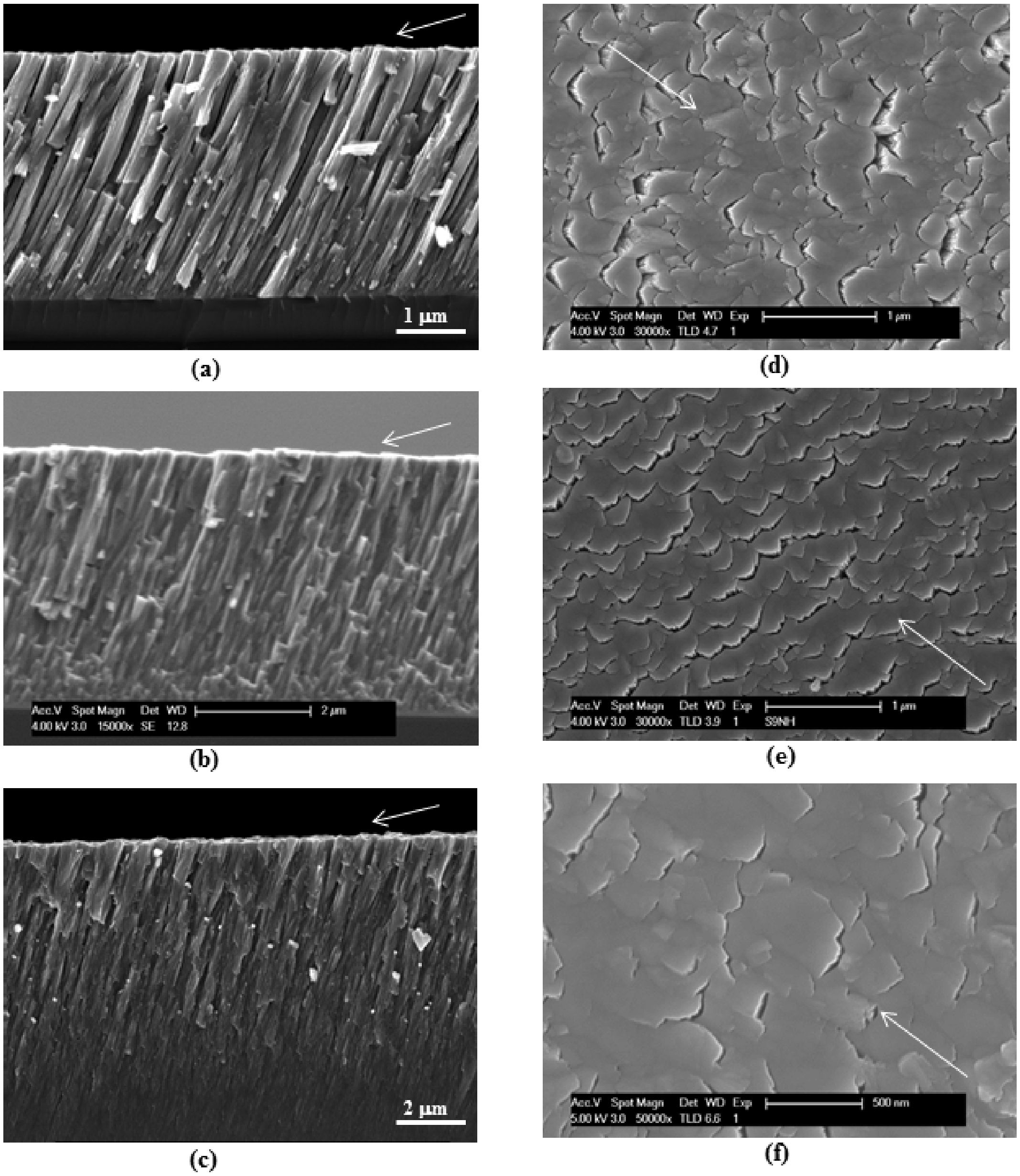

Fig. 8.3: *SEM micrographs showing microstructure of* $Ti_{0.5}Al_{0.5}N$ *thin films prepared under oblique angle deposition (α = 45°) at various temperatures. a, b, c) Transverse cross-section of samples deposited at room temperature, 400 °C and 650 °C, respectively. d, e, f) Plane view of the sample samples. The arrows indicate the direction of incident flux.*

Films deposited at RT reveal a columnar structure inclined towards the flux direction at β = 29.3° (Fig. 8.3a). The coatings exhibit a voided columnar structure. At 400°C, the surface diffusion starts influencing the film morphology. In other words, contrary to negligible or zero surface diffusion at RT, where the arriving adatoms stick to growing column where they land, diffusion driven mass transport at 400°C allows the adaparticles to travel some distance along the column side after attachment. Hence for films deposited at 400°C, close packed columnar structures are observed with a reduced inclination angle (β = 22.5°, Fig. 8.3b). When the substrate temperature is further elevated to 650°C, the column orientation nearly approached the substrate normal (β = 12.2°, Fig. 8.3c). A pronounced trend of decreasing intracolumnar voids along with the reduced inclination of columns is readily apparent with increasing temperature.

Figs. 8.3d-f corresponds to surface topography of the same films. For films deposited at RT, large voids are observed as a result of atomic shadowing (Fig. 8.3d). However, it can be seen that voids are closed up as the deposition temperature is increased (Fig. 8.3e-f)

At low substrate temperature, inclined columnar structure with voids between them is observed, showing low mobility of adatoms. By increasing the substrate temperature, as expected diffusion process dominate other process (eg. atomic shadowing), and film changes from porous/columnar structure to densely packed film without microvoids [9]. The SEM surface for film deposited at RT show large voids on the surface of the coating. These voids are formed due to the atomic shadowing effect because the vapor flux cannot be reached directly and the mobility of surface atoms is too slow for surface diffusion to fill up the voids. With increasing substrate temperature, the surface diffusion effects are enhanced hence it becomes possible for the adatoms to diffuse along the surface of the columns and fill the crystalline sites that are shadowed at room temperature [10].

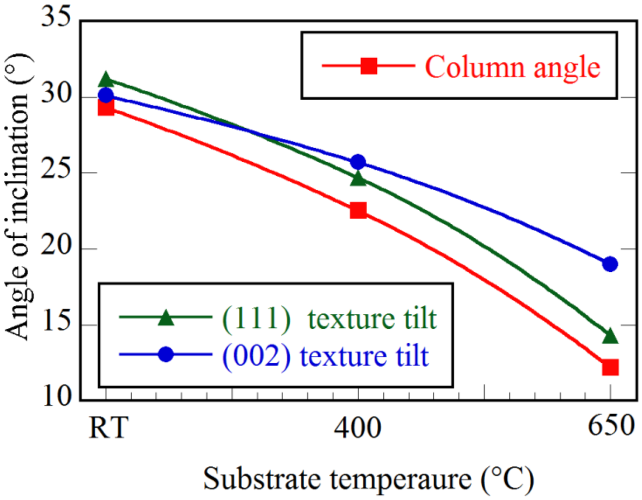

Fig. 8.4: *Effect of substrate temperature on the (111) and (002) texture tilt angles measured from the center of pole for* $Ti_{0.5}Al_{0.5}N$ *films. For comparison, the column inclination angle, β, is also shown.*

The tilt angle (τ) of (111) and (002) orientations was obtained from the pole figure data (Fig. 8.2).We notice that the tilt angles (τ) of 30°–32° at RT reduces to about 20°–15° at 650°C (Fig. 8.4b). In the same figure, column inclination angle (β) as a function of substrate temperature is also plotted. As noticed in the figure, the column inclination behavior is consistent with the <111> and <002> texture direction as temperature is varied from RT to 650°C. It is clear that with the increase in substrate temperature, the column inclination angle β approaches the film normal which in turn results in (111) and (002) planes nearing the substrate surface.

8.4 Mechanical properties of OAD films as a function of substrate temperature

In chapter 7, a great influence of flux angle α on the hardness and Young's modulus of the coatings was observed for OAD films at room temperature. If the substrate temperature is increased, the mechanical behavior is changed. In Fig. 8.5, one can notice an increase in hardness and Young's modulus when the substrate temperature is varied from RT to 650°C for films deposited under α = 45°.

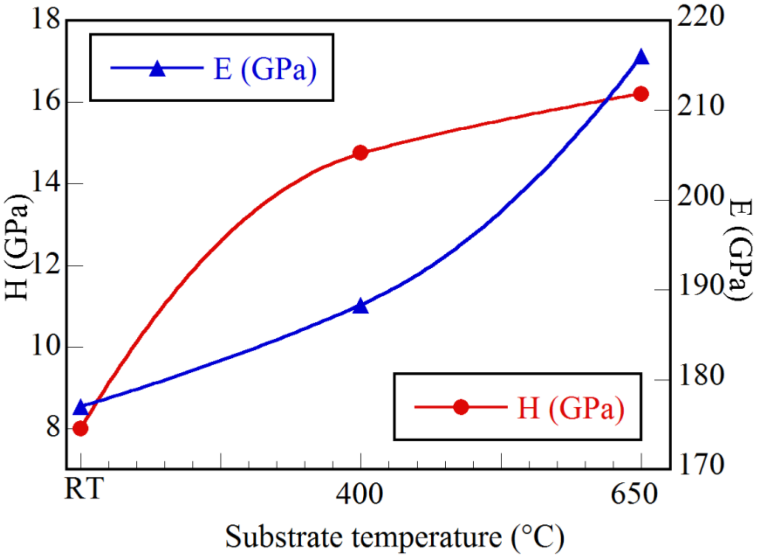

Fig. 8.5: *Improvement in hardness and Young's modulus as a function of substrate temperature for* $Ti_{0.5}Al_{0.5}N$*. The films were deposited under oblique angle of α = 45°.*

This variation in mechanical properties is in agreement with change in microstructure (Fig. 8.3). With an increase in deposition temperature, the shadowing effect is reduced and the voids in the microstructure are filled due to the surface diffusion of adatoms thus causing an improvement in mechanical properties [11]. However the mechanical properties of the films are still poor in comparison to films deposited under α = 0°.

8.5 Study of biaxial alignment of texture for different film composition and processing conditions

In this section, we will study the effect of deposition angle on the structure and properties of TiAlN films prepared using different target composition (60/40, at. %). $Ti_{0.6}Al_{0.4}N$ films were deposited onto Si(100) substrates under $\alpha = 0°$ and 45°. The substrate temperature was set at RT, 400 °C and 650 °C, and the bias was kept at 0, − 25, − 50, and − 80 V for both the deposition angles. The obtained results demonstrate that texture tilt angles and β−α relationship do not depend on film composition.

8.5.1 Crystalline structure and texture

a) θ-2θ scans

The θ–*2*θ scans of TiAlN films deposited at $\alpha = 45°$ for different substrate temperatures are shown in Fig. 8.6. The films exhibit a single phase cubic B1 NaCl-type structure. For films deposited at room temperature, no presence of (111) peak and weak signals from (002) reflections are observed. However, as the substrate temperature is increased, the coatings exhibit an improvement in peak intensities of (111) and (002) out-of-plane orientation (Fig. 8.6).

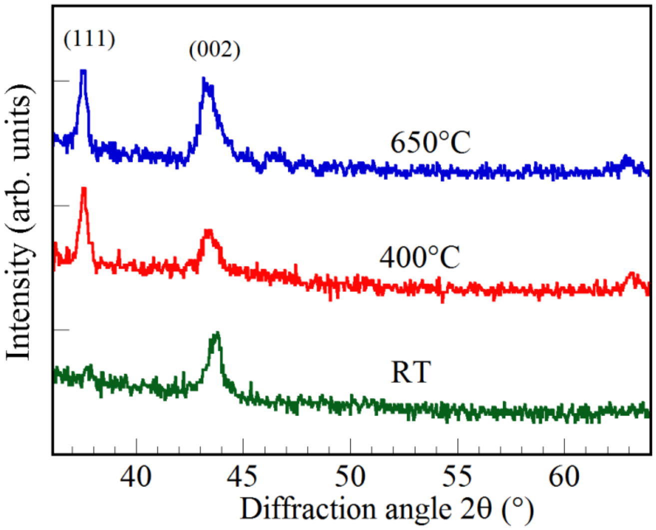

Fig. 8.6: *θ–2θ XRD patterns of* $Ti_{0.6}Al_{0.4}N$ *coatings deposited at* $\alpha = 45°$ *with a substrate bias of − 25 V. Deposition temperatures are indicated in the plots.*

Films deposited under oblique angle are considered by several authors to be amorphous; however, this is not the case. OAD films are crystalline, but due to the arrival of flux in the oblique direction which results in titling of columns in the direction of incident flux, the <hkl> growth direction is no longer parallel but tilted away from the substrate normal. As a result, no peak appears in the θ–2θ scan (Fig. 8.6, RT). However, as the substrate temperature is increased from room temperature to 650 °C, the increased surface diffusion allows the inclined lattice planes to approach parallel to the substrate surface, as a result of which improved peak intensities for (111) and (002) reflections are seen for depositions at higher substrate temperature under $\alpha = 45°$ (Fig. 8.6).

b) Pole figure XRD

The pole figures for films deposited under $\alpha = 45°$ at RT and 650 °C are displayed in Figs. 8.7a and b, respectively. In case of films deposited at room temperature, the (111) planes are not parallel to the substrate surface, but titled towards the direction of incident flux at an angle around 23.4°. This is somewhat near to the value predicted by the tangent rule $\tan\beta = \frac{1}{2} \tan\alpha$ ($\beta = 26°$). A preferred in-plane alignment corresponding to (002) planes is seen at $\psi = 56.6°$ and 56.1°. The (002) pole figure also reveals that the <002> orientation is not present at the center of the pole, but titled away from the direction of the deposition flux at around 30° from the substrate normal. In addition, some weak intensities are seen at $\psi = 71.2°$ (Fig. 8.7a). The (022) pole figure exhibits a preferred in-plane texture of (111) orientation at a diffraction angle of $\psi = 33.4°$ and 33° and an in-plane alignment of (002) reflections at 66.2° and 67.6°.

For OAD films at 650 °C, (111) pole figure shows that (111) planes are approaching close to the substrate normal (Fig. 8.7b). This can also be corroborated from the θ–2θ scan for the same sample which show that for deposition under $\alpha = 45°$, the (111) peak which is absent at room temperature is however seen at higher deposition temperature (Fig. 8.6). The in-plane texture corresponding to (002) is seen to weaken at 650°C. Similarly, the (002) pole figure reveals that the tilting of <002> has reduced to 22.11° from 30° for room temperature deposition (Fig. 8.7b). The (022) pole figure reveals that the preferred in-plane alignment corresponding to (111) and (002) planes is not well developed as compared to films deposited at room temperature. In addition, we notice a rise in random orientations with deposition temperature.

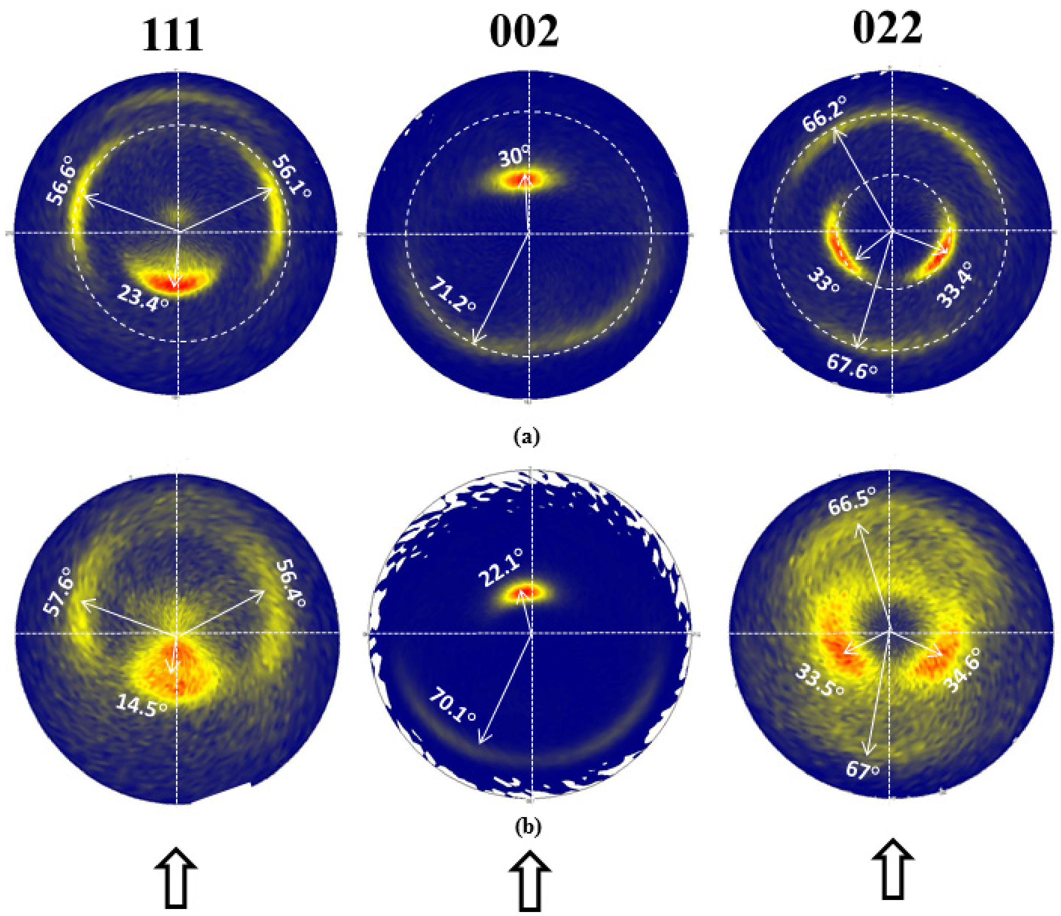

Fig. 8.7: *Pole figures for (111), (002) and (022) reflections of* $Ti_{0.6}Al_{0.4}N$ *films deposited at a) RT and b) 650 °C for α = 45°.The growth direction of <111> and <002> approaches the center of the pole along with the weakening of in-plane texture at higher substrate temperature. The arrows indicate direction of incident flux.*

The plot of grain size obtained from the Williamson–Hall plot for α = 0° and 45° as a function of bias voltage is shown in Fig. 8.8. For α = 0°, the grain size is decreased as the bias is increased. The decreasing grain size with increasing substrate bias is due to the increased renucleation rate of the growing films, which is induced by the ion-irradiation-generated defects [12]. For α = 45°, we also observe the same effect, the only difference is that the grain size is slightly higher. One possible reason could be that in oblique deposition some grains grow faster and, consequently, at the expense of other grains that are consumed during the process of growth which results in large grain sizes. This observation is also supported by others as well [13,14]. However, in the study of obliquely deposited copper oxide films, Akkari et al. found a decrease in grain size with increasing incident angle [15].

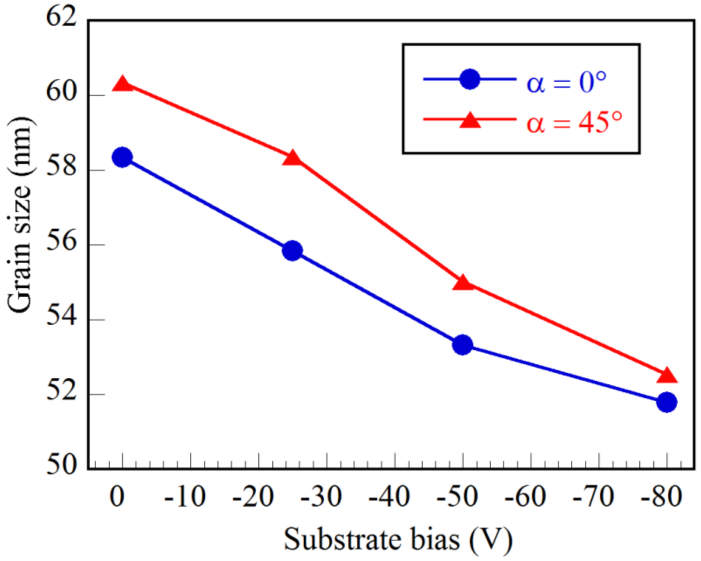

Fig. 8.8: *Grain size calculated by Williamson–Hall plot as a function of bias voltage for depositions under α = 0° and 45°.*

The effect of substrate bias on the microstrain (ε) deduced by the Williamson–Hall plots for films deposited under normal and oblique angle incidence is displayed in Fig. 8.9. The microstrain (ε) shows an increasing trend with increasing bias for both α = 0° and 45. However for α = 45°, ε is less compared to films deposited at α = 0°. A reduced microstrain values may result from the voids and defects associated with the shadowing effect during oblique angle deposition [11]. An increase in substrate bias leads to an increase in the ion bombardment and the number of defects (dislocations and points defects) of the lattice associated with the microstrain also increases [16]. Perry et al. [17] and Valvoda et al. [18] in their study concluded that this increase in strain with bias is due to an increasing lattice distortion and disorder.

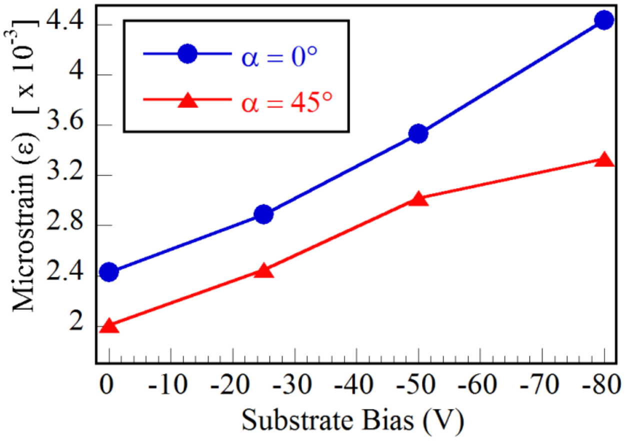

Fig. 8.9: *Microstrain (ε) values obtained by Williamson–Hall plot as a function of bias voltage at α = 0° and 45°.*

8.5.2. Effect of temperature on the microstructure of obliquely deposited $Ti_{0.6}Al_{0.4}N$ coatings

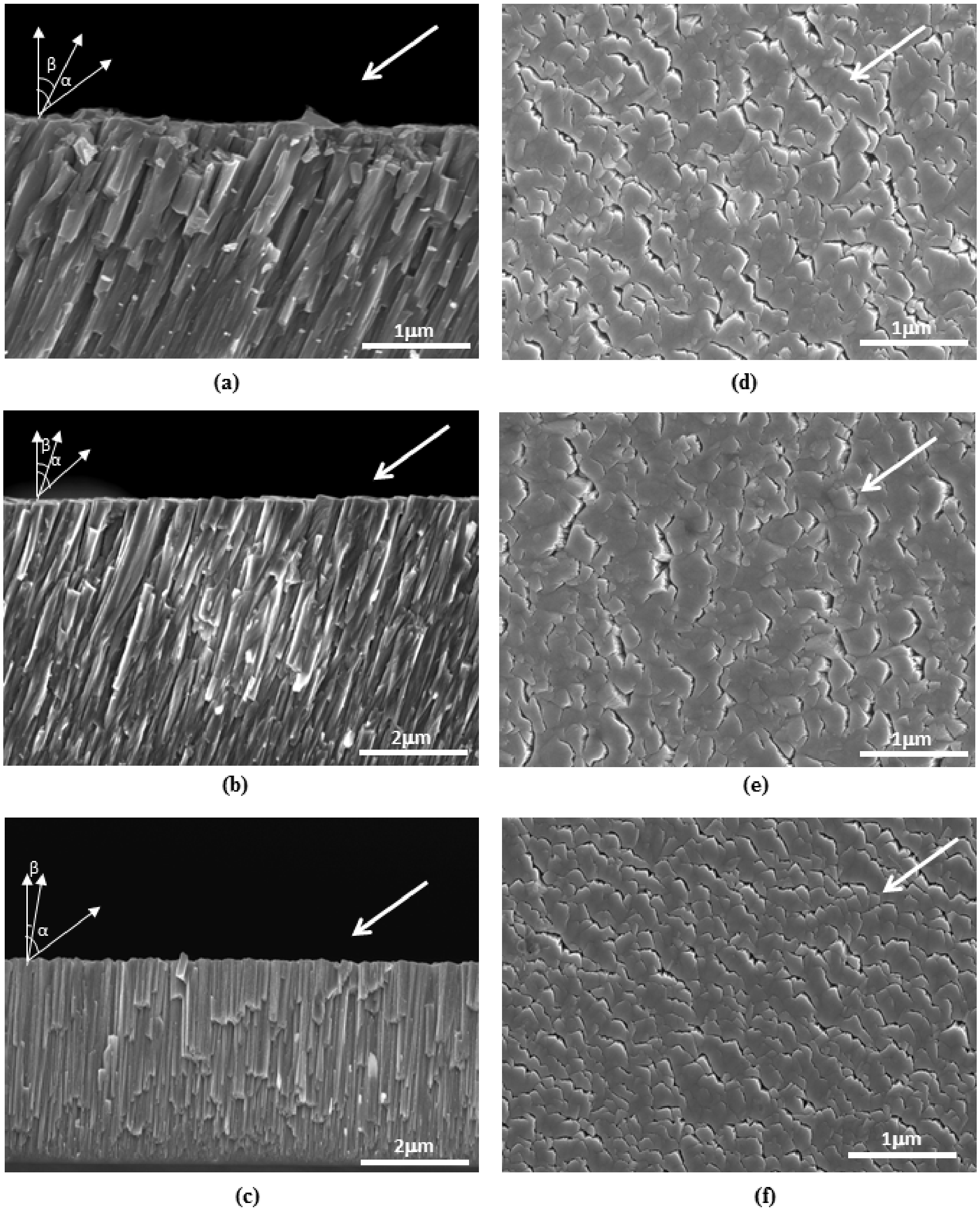

Fig. 8.10: *SEM micrographs showing microstructure of* $Ti_{0.6}Al_{0.4}N$ *films prepared under oblique angle deposition (α = 45°) at − 25 V bias. a, b, c) Transverse cross-section of samples deposited at room temperature, 400 °C and 650 °C, respectively. d, e, f) Plane view of the same samples. In all micrographs, α is the incident flux angle and β is the column angle. The arrows indicate the direction of incident flux.*

The cross-section of $Ti_{0.6}Al_{0.4}N$ film deposited under $\alpha = 45°$ at room temperature with a bias of − 25 V is shown in Fig. 8.10a. For oblique angle deposition, the columns are titled in the direction of the incident flux. The column angle β measured was 21°, which was somewhat near to the value predicted by the tangent rule ($\beta = 26°$) given by the formula $\tan\beta = ½ \tan\alpha$ [19]. It has been demonstrated that flux angle α and column angle β are not equal because of the shadowing effect [20]. Flux angle has a major influence on the coatings deposited in room temperature than at higher temperature [21]. It can be seen from Figs. 8.10b and c that the columns are less inclined towards the incoming flux as the substrate temperature is increased. For deposition at 400 °C, the column angle was found to be around 17° which is less compared to the column angle at room temperature. Finally at 650 °C, the inclination was further decreased to 11°. Nakhodkin and Shaldervan [22] studied the deposition of a variety of materials at multiple angles of incidence. As the substrate temperature was increased, they also found that the column orientation approached the substrate normal ($\beta = 0°$). In experiments on iron films deposited at $\alpha = 45°$, Hashimoto et al. [23] found a similar relation between β and substrate temperature.

Fig. 8.10d displays the surface of $Ti_{0.6}Al_{0.4}N$ film ($\alpha = 45°$) deposited at room temperature, with − 25 V bias. Since in oblique angle deposition, the incident flux arrives at oblique angles to the substrate causing atomic shadowing, which produces areas that incident flux cannot reach resulting in a voided microstructure. We can say that the surface of coating in an oblique angle deposition resembles to that of a “tiles of a roof” or “stepwise structure” viewed from the top. This particular morphology is due to the oblique arrival of the ion flux and not from the SEM because the samples are not tilted. As we increase the flux angle, the shadowing effects will also increase [24]. Figs. 8.10e and f exhibit the surface of $Ti_{0.6}Al_{0.4}N$ coating ($\alpha = 45°$) deposited at 400 °C and 650 °C. As the substrate temperature is increased, the spaces between the voids are getting closed up. Voids are known to form as a consequence of both surface roughness and shadowing effects. According to Dong et al. [25], at any deposition angle, increasing the temperature increases the mobility of atoms at the surface which is capable of overcoming the atomic shadowing effects that produces void. As the angle of incidence α is increased, the shadowing becomes more effective, and to overcome this problem the temperature must be further increased in order to produce a film with the same density as one produced at $\alpha = 0°$.

8.5.3. Mechanical properties

To investigate the influence of flux angle on the mechanical properties of the coatings, nanoindentation tests were performed. The plots of hardness and Young's modulus of $Ti_{0.6}Al_{0.4}N$ films deposited at 650 °C under $\alpha = 0°$ for different bias voltages are shown in Fig. 8.11a and b. As the negative substrate bias is increased, the hardness also increases accordingly. Increase in bias has been associated with change in the microstructure of the coating. In other words, the increased bias voltage results in a denser, less columnar structure [26]. In addition, this rise in hardness can partly be explained by decrease in grain size (Fig. 8.8). When the substrate bias is increased, the coatings are exposed to ion bombardment with high energy atoms, thus creating preferential nucleation sites and hence enhancing the atom mobility, which in turn reduces the void formation and creates fine grain structure [27,28].

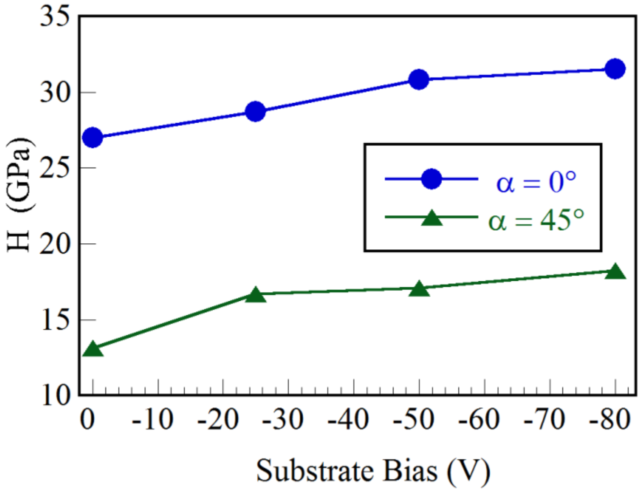

(a)

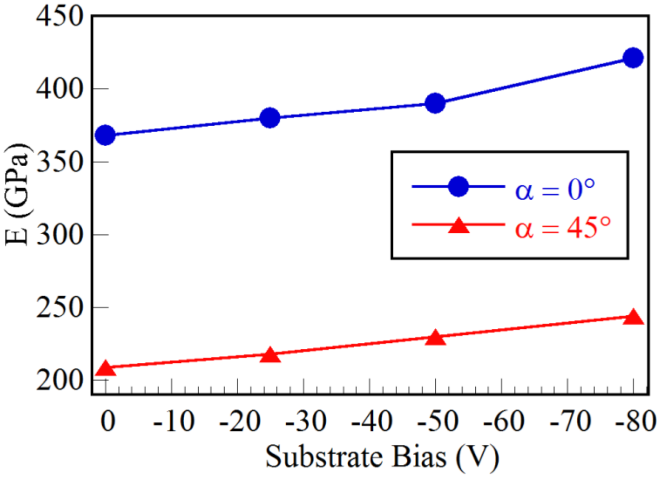

(b)

Fig. 8.11: *Influence of deposition angle on the mechanical properties of* $Ti_{0.6}Al_{0.4}N$ *coatings deposited at 650 °C under different bias, a) hardness for* $\alpha = 0°$ *and 45°, b) Young's modulus for* $\alpha = 0°$ *and 45°.*

Fig. 8.11a and b depicts the graph of hardness and Young's modulus of $Ti_{0.6}Al_{0.4}N$ deposited at α = 45° as a function of bias voltage at 650°C. The hardness and Young's modulus values are low compared with α = 0° though both show a similar increasing trend with bias. This decrease in hardness and Young's modulus can be explained by two phenomena: 1) voids formed in the film surface and 2) lower stress. The residual stress is compressive with − 1.23 GPa for α = 0°, and shows a tensile stress of 1.45 GPa for α = 45°. These voids are formed due to the tensile stress in the films. Change in the flux angle has a major influence on the microstructure of the coating leading to inclined columns separated by voids. These ones reduce the amount of probed matter during indentation test leading to decrease in hardness [29].

Because the column inclination angle (β) lies between the film normal and the vapor incidence angle (α) and is dependent upon many factors such as substrate temperature, deposition rate, angular distribution of the deposition flux and background pressure. It was found interesting to study the role of substrate temperature on the hardness and Young's modulus of the coatings deposited by oblique angle deposition. Fig. 8.12 corresponds to the graph of hardness and Young's modulus of films deposited under α = 45° at a bias of − 25 V for different substrate temperature. The hardness and Young's modulus shows an increasing trend with increase in substrate temperature. As seen from the SEM images in Fig. 8.10, we can assume that as the substrate temperature is increased, the surface diffusion is enhanced which leads to covering of voids thus improving the hardness as compared to films at room temperature. Both $Ti_{0.5}Al_{0.5}N$ (Fig. 8.5) and $Ti_{0.6}Al_{0.4}N$ (Fig. 8.12) displayed similar trend in mechanical properties with substrate temperature for depositions under α = 45°.

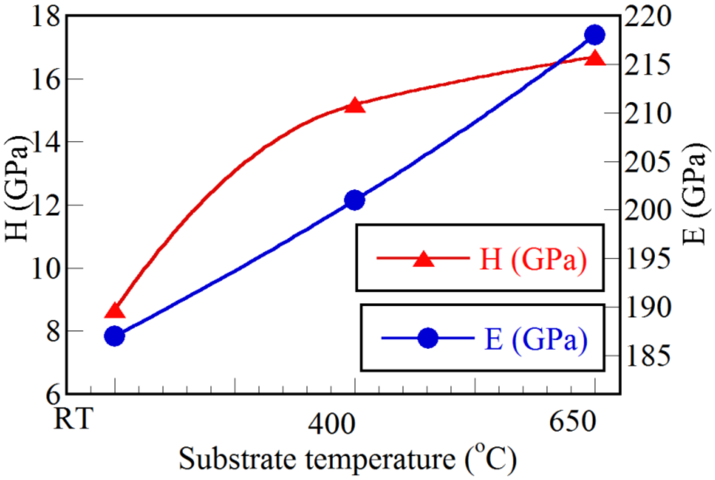

Fig. 8.12: *Hardness and Young's modulus of obliquely deposited* $Ti_{0.6}Al_{0.4}N$ *samples as a function of temperature for a bias of − 25 V.*

8.6 Summary of results obtained in this chapter

The biaxial alignment and its related properties of $Ti_{1-x}Al_xN$ films prepared by sputtering using targets of various compositions are investigated. The experimental data show that the in-plane texture and α-β relationship do not depend on the film composition. Besides the deposition angle, the substrate temperature is also found to play an important role in biaxial alignment and inclination of columns. The degree of in-plane texture is weakened along with the shifting growth directions for <111> and <002> towards the substrate normal when the substrate temperature is varied from RT to 650°C. It was shown that by enhancing the adatom mobility (i.e. increasing substrate temperature), the inclination of column angle β decreases thus diminishing the influence of flux angle. The film microstructure changes from inclined columnar structure with large voids to a dense film with few voids along with the column angle nearly approaching the film normal with increasing deposition temperature. Mechanical properties for OAD films was found to increase with temperature since the intracolumnar voids are filled with diffusing adatoms resulting in growth being more homogeneous than for the coatings deposited at room temperature. However, the values of hardness and Young's modulus are smaller as compared to those deposited at $\alpha = 0°$.

8.7 Reference

[1] D. Singh, R. Nagar, J. P. Singh, J. Appl. Phys. 107 (2010) 074306.

[2] F. Tang, D. -L. Liu, D. -X. Ye, Y. -P. Zhao, T. -M. Lu, G. -C. Wang, A. Vijayaraghavan, J. Appl. Phys. 93 (2003) 4194.

[3] J. P. Singh, T. Karabacak, D. -X. Ye, D. -L. Liu, C. Picu, T. -M. Lu, G. -C. Wang, J. Vac. Sci. Technol. 23 (2005) 2114.

[4] E. Schubert, J. Fahlteich, B. Rauschenbach, M. Schubert, M. Lorenz, M. Grundmann, G. Wagner, J. Appl. Phys. 100 (2006) 016107.

[5] M. Pyun, E. Kim, D. Yoo, S. Hahn, Appl. Surf. Sci. 257 (2010) 1149.

[6] P. Li, J. Carroll, J. Mazumder, J. Phys. D: Appl. Phys. 36 (2003) 1605.

[7] K. Thiele, S. Sievers, C. Jooss, J. Hoffmann, H. Freyhardt, J. Mater. Res. 18 (2003) 442.

[8] C. Khare, J. Gerlach, M. Weise, J. Bauer, T. Hoche, B. Rauschenbach, Phys. Status Solidi A 208 (2011) 851.

[9] H. Savaloni, M. Shahraki, Nanotechnology 15 (2004) 311.

[10] H. G. Chew, W. K. Choi, W. K. Chim, E. A. Fitzgerald, Int. J. Nanosci. 05 (2006) 523.

[11] A. R. Shetty, A. Karimi, M. Cantoni, Thin Solid Films 519 (2011) 4262.

[12] P. K. Huang, J. W. Yeh, J. Phys. D Appl. Phys. 42 (2009) 115401.

[13] J. Lintymer, J. Gavoille, N. Martin, J. Takadoum, Surf. Coat. Technol. 174–175 (2003) 316.

[14] J. Lintymer, N. Martin, J. -M. Chappé, P. Delobelle, J. Takadoum, Surf. Coat. Technol. 180–181 (2004) 26.

[15] F. Chaffar Akkari, M. Kanzari, B. Rezig, Eur. Phys. J. Appl. Phys. 40 (2007) 49.

[16] P. Y. Jouan, G. Lempérière, Thin Solid Films 237 (1994) 200.

[17] A. J. Perry, M. Jagner, P. F. Woerner, W. D. Sproul, P. J. Rudnik, Surf. Coat. Technol. 43 (1990) 234.

[18] V. Valvoda, R. Kuzel Jr., L. Dobiásová, R. Cerný, V. Poulek, J. Musil, Surf. Coat. Technol. 41 (1990) 377.

[19] J. M. Nieuwenhuizen, H. B. Haanstra, Philips Tech. Rev. 27 (1966) 87.

[20] A. R. Shetty, A. Karimi, Phys. Status Solidi (b) 249 (2012) 1531.

[21] D. Deniz, J. M. E. Harper, J. W. Hoehn, F. Chen, J. Vac. Sci. Technol. A 25 (2007) 1214.

[22] N. G. Nakhodkin, A. I. Shaldervan, Thin Solid Films, 10 (1972) 109.

[23] T. Hashimoto, K. Okamoto, K. Hara, M. Kamiya, H. Fujiwara, Thin Solid Films 91 (1982) 145.

[24] K. Robbie, M. J. Brett, J. Vac. Sci. Technol. A 15 (1997) 1460.

[25] L. Dong, R. W. Smith, D. J. Srolovitz, J. Appl. Phys. 80 (1996) 5682.

[26] A. C. Vlasveld, S.G. Harris, E.D. Doyle, D. B. Lewis, Surf. Coat. Technol. 149 (2002) 217.

[27] K. Bobzin, E. Lugscheider, M. Maes, P. Immich, S. Bolz, Thin Solid Films, 515 (2007) 3681.

[28] Y. H. Cheng, B. K. Tay, S. P. Lau, X. Shi, J. Vac. Sci. Technol. A, 19 (2001) 736.

[29] J. Lintymer, N. Martin, J. -M. Chappé, P. Delobelle, J. Takadoum, Surf. Coat. Technol. 200 (2005) 269.

Chapter 9:

Discussion

9.1 Dynamics of off-axis tilt of (002) through film thickness

Factors that influence the formation of crystallographic orientation in films with thickness can be ascribed to energy minimization and kinetic factors. Examples of kinetic factors are growth velocity differences between different crystal faces, flow induced by stress, and interaction effects with the ion beam such as channelling. Texture development may occur during the nucleation stage due to the substrate texture inheritance, resulting in films which have preferred orientation similar to that of substrate (single crystal). In the situation where amorphous or randomly oriented polycrystalline substrates are used, nucleation of island occurs and texture development may be controlled either during coalescence and/or during film thickening. The results in our case indicate that the preferred orientation in nitride films with thickness is controlled by thermodynamics in initial stages and later by kinetic effects at final stages of film growth.

Fig. 9.1 illustrates the schematics of the preferential orientation mechanism for polycrystalline $Ti_{0.5}Al_{0.5}N$ and $Ti_{0.67}Al_{0.33}N$ films with deposition time. Texture development with respect to film thickness consists of:

- At initial stages (<1 μm), the films tend to minimize its surface energy and hence a <002> orientation parallel to substrate normal is seen (Fig. 9.1a).

- During midway stages (1–3 μm), the films show a gradual buildup of (111) in addition to dominant (002) due to competitive growth and kinetic factors (Fig. 9.1b).

- Finally, at higher thickness (>3 μm), the dominant <111> orientation parallel to film normal is observed, while the <002> is off-axis tilted to accommodate these growing (111) planes (Fig. 9.1c).

- However, for $Ti_{0.67}Al_{0.33}N$, the texture evolution follows the process as discussed above, but the final dominant orientation at higher thickness is (113) at not (111) as excepted (Fig. 9.1e).

In this case, one can consider the evolution of texture in three different stages of film growth.

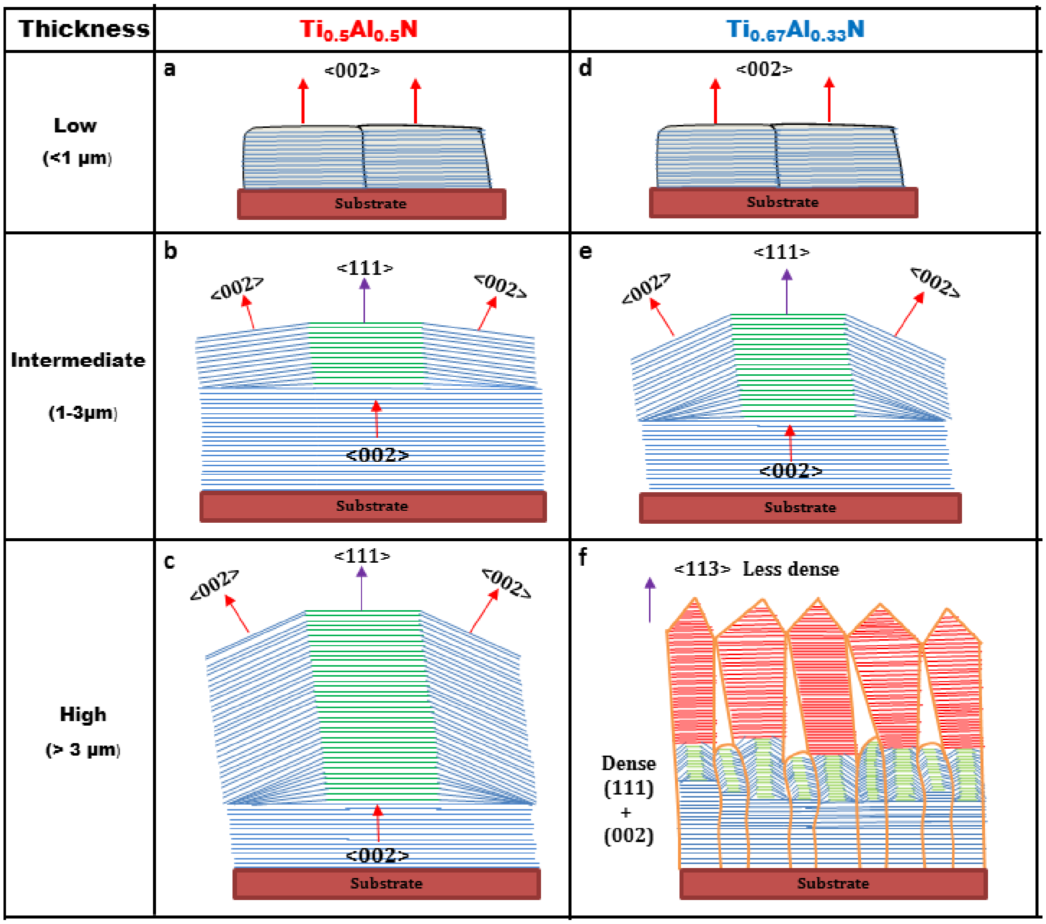

Fig. 9.1: *Typical illustrations of texture development with thickness for* $Ti_{1-x}Al_xN$ *films. For* $Ti_{0.5}Al_{0.5}N$*: a) at low thickness, grains with (002) orientation are parallel to film normal. b) During the intermediate stage of film growth, the (002) planes begin to tilt away due to the build-up of <111> orientation parallel to film growth. c) At higher thickness, in order to accommodate the fast growing (111) planes, the slow growing (002) grains are tilted away from the substrate normal. In case of* $Ti_{0.67}Al_{0.33}N$*: the growth mechanism of similar to* $Ti_{0.5}Al_{0.5}N$ *(d,e). However, the final dominant orientation is (113) and not (111).*

9.1.1 Initial stage

The lowest surface energy face of $Ti_{1-x}Al_xN$ is the (002). Hence the (002) surface would be expected to be the preferred orientation at elevated growth temperatures where adatom mobilities are sufficient to form crystallites bounded by low energy planes during nucleation and/or liquid-like coalescence [1]. This is precisely what we observe, the *θ–2θ* and pole figure XRD studies reveal that at low thickness, a (002) orientation is seen (chapters 4 and 6). The calculated surface energy for TiN (100) 0.395×10^{-3} J/cm^2, is less than those for both (111) and (311) TiN planes, 0.66×10^{-3} J/cm^2 and 0.74×10^{-3} J/cm^2, respectively, indicating that the (100) is the lowest energy surface (Fig. 9.2). Thus under high temperature depositions where thermodynamics control the texture formation rather than kinetics, (001) is expected to be the dominant growth orientation [2]. The same argument can be applied to a TiAlN thin film.

(hkl)	**111**	**100**	**311**
Atomic structure of (hkl)	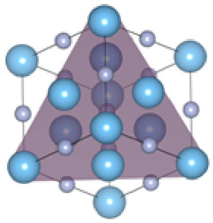	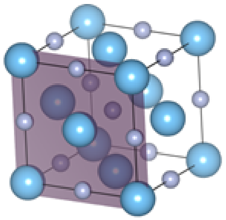	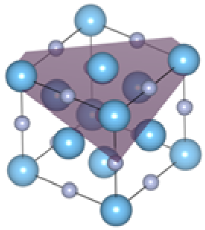
$S_{hkl} \times 10^{-3}$ (J/cm^2)	0.66	0.395	0.74

Fig. 9.2: *Atomic structure and surface energy (S_{hkl}) of (hkl) plane of TiN crystal with NaCl-type structure.*

However, the (002) pole figure for low thickness films on WC-Co (104 nm, Fig. 4.9a) also reveals that the (002) planes are not exactly parallel to the substrate surface but are tilted slightly off-axis. This few degrees of off-axis tilt could be due to the interface energy between the substrate and the growing film. According to Riesz [3], at the very beginning of the film growth, the interface energy is dominant, and therefore the film is expected to be in complete accommodation with the substrate to minimize the interfacial energy. When the film growth progresses by forming islands on the substrate, a strain relief is developed due to the lattice mismatch and changes the lattice spacing which in turn results in small tilt of lattice planes [4]. This is precisely seen from the (002) pole figure of a 104 nm thick film. The (002) planes are slightly tilted away from the surface normal (Fig. 4.9a). The *θ–2θ* scan of the same sample alone cannot reveal any such information. Usually this off-axis tilt is often seen in epitaxial systems [3-5]. However, in such systems the tilt angle is proportional to the lattice mismatch between the substrate and the film. In some cases, a large tilt angle up to 58° is observed [6]. However, since we have randomly oriented polycrystalline substrate, the growth at the interface is not fully epitaxial, but only partially coherent with only a fraction of crystallites are aligned and of that the tilt angle is much less (see Fig. 9.3). This is why the (002) pole figure (Fig. 4.9a) exhibits a random intensity distribution along with a diffraction intensity maxima concentrated close to the center of the pole (~5° in our case). To ensure reproducible results, we have deposited films on WC-Co at same thickness range (~ 100 nm) and noticed the similar tilt on all the samples.

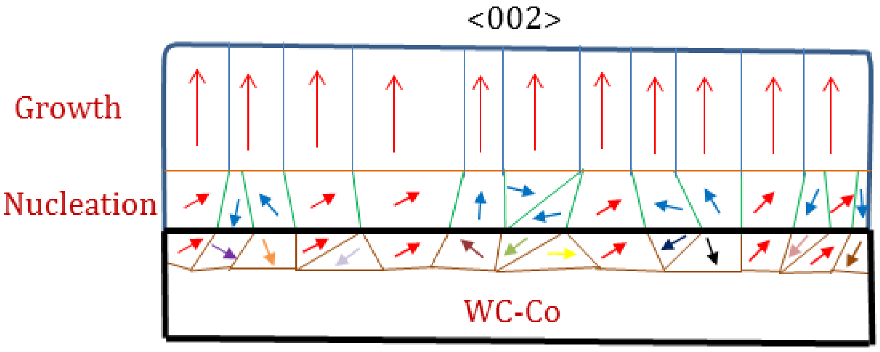

Fig. 9.3: *Schematic of texture formation at low thickness for films on WC-Co. During the initial stages of film growth, only a fraction of the crystallites are aligned (red arrows) with substrate and tilted slightly away from the film normal to relieve the strain at the interface. At later stages, the growth direction of <002> is parallel to film normal.*

In contrast no such off-axis tilt is observed for a 288 nm thick film deposited on glass (Fig. 4.3a). This could be due to the substrate effect. Since glass is amorphous, the bonding energy between adatoms is dominant for nuclei formation with no need to lattice mismatch. Therefore, it seems likely that nuclei on amorphous substrates have random orientations to eventually lead to the development of a (002) texture once the film has become continuous (Fig. 9.4).

As the film thickens and becomes continuous, grain growth can occur through minimization of grain boundary, surface and interface energy. For the 860 nm thick film on WC-Co, the (002) planes are now parallel to the substrate surface (Fig. 4.9b). That means the lattice mismatch which caused the tilting of (002) planes at low thickness is now no longer seen with increasing thickness. This confirms that the off-axis tilt originated from the interface alone. This recovery is due to the stress relaxation with increasing film thickness and to the surface energy which becomes dominant with respect to interface energy. Films deposited on glass around the same thickness range (900 nm, Fig. 4.3b) have a complete (002) texture. Indeed, in this later stage, growth occurs mainly in the direction normal to the substrate, and the system tends to minimize the surface energy.

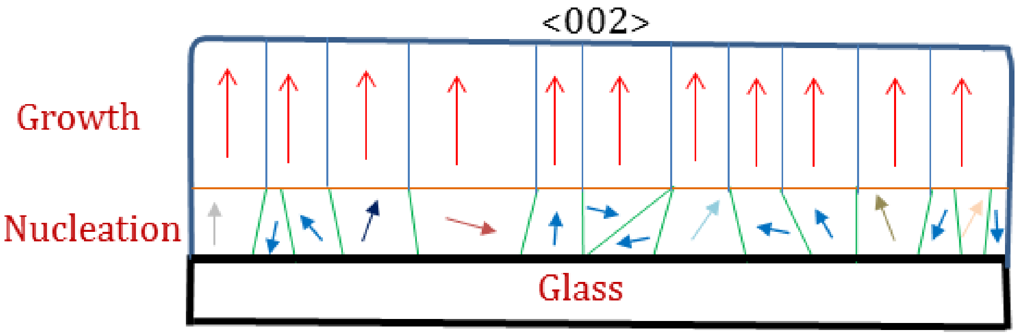

Fig. 9.4: *Typical illustration of texture development on glass substrates at low thickness. Grains nucleated here often exhibit random orientation, which later develop a preferential orientation with film thickness.*

9.1.2 Intermediate stage

In this range of film thickness, the gradual development of (111) orientation is due to the kinetic effects rather than thermodynamic driving forces as described for previous low thickness regime films. For a 2.32 μm and 1.92 μm thick film on glass and WC-Co, the (002) pole figures reveal that most of the reflections are concentrated at the center of the pole, but some reflections are tilted which signify that from this stage the (002) planes begins to tilt away (Figs. 4.3c and 4.9c). In contrast, the (111) pole figure reveals that the (111) planes become parallel to the substrate surface (Figs. 4.3c and 4.9c), which indicates the development of a (111) texture within this range of film thickness. TEM and SAED observations (section 5.4, Fig. 5.9) support the XRD results that appearance of (111) orientation occurs only at a particular thickness below which the majority of grains are (002) oriented [7].

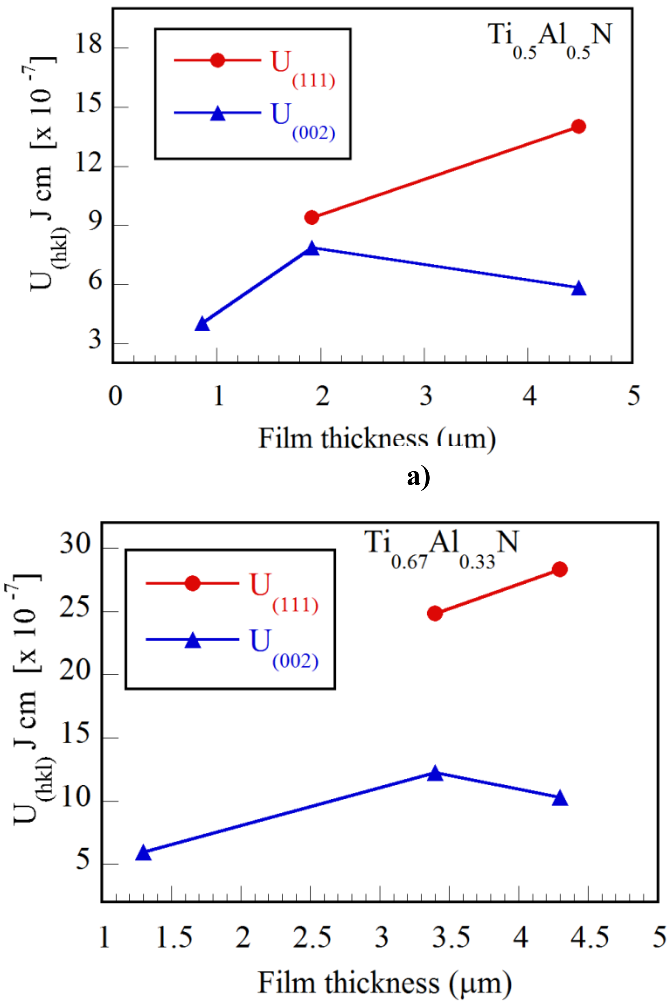

b)

Fig. 9.5: *Variations of strain energy $U_{(hkl)}$ of $Ti_{0.5}Al_{0.5}N$ and $Ti_{0.67}Al_{0.33}N$ with film thickness. The strain energy value along the (111) was found to be higher than (002) as well as increases with deposition time which is in contradiction with energy minimization model.*

Several authors [8-10] have attributed the change from a (002) to a (111) preferred orientation using thermodynamics arguments, i.e., as being the result of minimizing the overall free energy of the film (including surface, strain, and stopping energy). The surface energy does not vary with film thickness whereas the strain energy increases with it. The increase in strain energy, which is dependent on the plane (hkl) is larger on the (111) than on the (002) plane (see Fig. 9.5). This means that strain level is increased in grains having (111) planes parallel to film surface. Since these planes are more compliant, they can store more strain energy as the film thickens. Abadias and Tse [11] determined the elastic strain energy and deformation of (001) and (111) for TiN, and obtained $u^{001}{}_{el} = 32\ J/cm^3$ and $u^{111}{}_{el} = 59\ J/cm^3$, and $\varepsilon_{111} = 1.4\%$ and $\varepsilon_{002} = 1.1\%$, respectively. In chapter 5, we have also shown out that

(111)-oriented grains sustain higher compressive stress than (002) ones (Fig. 5.1). This result clearly shows that the development of a (111) orientation with film thickness does not arise from strain energy minimization. There is additional experimental evidence [12] which suggest that strain energy is not responsible for the change in preferred orientation in magnetron sputtered TiN films. Other mechanisms such as competitive growth are likely to take place and to compete with thermodynamic effects [11]. Van der Drift [13] pointed out that surface morphology is varied with film thickness (see Fig. 5.4) and that an evolutionary selection of grains with a preferred orientation takes place. For $Ti_{1-x}Al_xN$, the fast growing surface is the (111) plane [14]. In chapters 7 and 8, we have shown that for $Ti_{1-x}Al_xN$ films deposited under oblique angles, the (111) plane has the largest capture cross-section, and it turns towards the flux direction by outgrowth of grains with (002) preferred orientation [15]. Cross sectional TEM micrographs and SAED patterns reveal that the (111) orientation develops steadily through a competitive growth (Fig. 5.9) [7]. Adibi et al. [16] in their study of crossover in $Ti_{0.5}Al_{0.5}N$ alloy films reported that the (111) preferred orientation is developed gradually through competitive growth as columns with other orientations slowly grow out of existence. Therefore in our case, the eventual growth of the high-energy polar (111) surface parallel to substrate is due to the kinetic limitations rather than thermodynamic driving forces.

9.1.3 Final stage

The (002) pole figures for 4 μm thick films on glass and WC-Co reveal that there are no reflections at the center of the pole and the majority of (002) planes are tilted away from the surface normal (Figs. 4.3d and 4.9d). At the same time, the (111) reflections are at the center of the pole indicating that growth direction of <111> is parallel to the substrate normal. In evolutionary selection, the grains with <111> direction normal to the substrate enveloped the grains with (002) plane due to anisotropy of growth rates and were enclosed by slowest growing (002) planes. Hence the (002) oriented grains should perish in the bulk by the overlapping of (111) grains with increasing thickness. In contrast in our study, the share of (002) grains decreases on the surface and they are tilted away with an in-plane alignment from the surface normal. This tilting of (002) planes allows the <111> orientation remain parallel to film normal (Fig. 9.1c).

Hence, combining the pole figure measurements and SEM image observation, the <111> direction can be considered having the largest geometric growth rate and the (111) grains are (002) facetted. The nuclei with their fastest growing orientation perpendicular to the surface will overgrow the slower facets as the film coalesces.

Thus the roughness of the film increases with film growth (Fig. 5.5). This roughness becomes more pronounced at the onset of competitive growth and influences preferred orientation (in our case (111)) and crystal coarsening. With increasing film thickness, the (111) planes are parallel to the substrate surface, and in order to accommodate these growing number of planes, the slow growing (002) grains are tilted away from the substrate normal, showing substantial in-plane alignment. Along with the evolutionary selection, some roughening dominant mechanism such as shadowing effect could also contribute to the growing surface and texture. This off-axis tilt of (002) at higher thicknesses is decreases with the deposition temperature as shown in Fig. 4.12. This can be explained by the increased mobility of the adatoms at higher temperature, which promotes diffusion across grain boundaries and then these (002)-oriented grains try to anchor close to the film normal.

The texture dynamic for $Ti_{0.67}Al_{0.33}N$ is similar to $Ti_{0.5}Al_{0.5}N$ as discussed above, but the final dominant orientation at higher thickness is (113) and not (111). The major (113) orientation parallel to the sample surface is in contrast to the expected (111) orientation as reported by other authors [17-19]. With increasing thickness, the crystallites remarkably exhibit a change from (111) to (113) dominant orientation. We assume that because of high compressive stress in grains with the (111) orientation, which might result in cohesive fracture of the films, the growing film adapts its orientation by choosing a less dense plane, i.e (113) in our case. Noveau et al. [19] claim that for CrN thin films, the preferential orientation of the crystalline plane changes to (113) as the thickness increases. They have reported that this change in orientation results in decrease in stress and film density. Also, in our study, one can notice that the stress relaxation in (111) grains (Table 6.1) occurs through the transformation of crystallographic orientation of films with its thickness. At higher thickness, the growth is finalized by the formation of less dense planes i.e (113). This change results in decrease in stress and hardness for thicker films. Our investigations demonstrate that the stress profile is not uniform through film thickness. This change in stress involves the transition from a dense structure to a less compact one, promoting accordingly the growth of (113) at higher thickness (Fig. 9.1f).

9.2 Sustaining (002) texture through film thickness on Si substrates with no off-axis tilt

The accommodation of (002) planes with Si is different from WC-Co and glass substrates. The pole figures for films deposited on Si did not exhibit any tilted <002> growth direction at higher thickness (Fig. 4.6d). Instead, the films feature a dominant <002> texture nearly parallel to the film normal through the film thickness, with only a small fraction of (111) grains detected at later stages of film growth. Such growth behaviour of <002> is quite opposite to films grown on glass and WC-Co. This indicates that grains give rise to such a well-defined orientation relationship with respect to the substrate, i.e. these are coherent grains. The SAED patterns (Fig. 5.12) indicate a marked improvement in film crystalline quality and texture from the film-substrate interface up to the film surface which is in good agreement with θ-2θ scans (see Fig. 4.4). In this case, the surface and interface energy anisotropy provides a driving force for grain growth. Grains with low combined surface and interface energy have an energetic advantage and can grow preferentially. There are systems for which surface and interface energy minimization cooperate or compete during the grain growth. However there is always a specific crystallographic orientation that produces a global minimum in the sum of the surface and interface energies [20]. In our case it is the (002) orientation. As the surface and interface energy driving force for grain growth is size independent, it can overcome the competitive growth driving force for thick films. The minor presence of (111) in addition to prevalent (002) texture indicate that competitive growth is not dominant enough to promote the growth of (111) within this thickness range. Rather, the thermodynamic driving forces are responsible for the build-up of (002) as the main orientation. Though many authors have reported a cross-over from (002) to (111) on a single crystal substrate like silicon. This could be due to the different deposition techniques and parameters involved.

In this study, we have come up with correlation between the orientation of grains and surface roughness for $Ti_{0.5}Al_{0.5}N$. Especially for films on WC-Co and glass, the development of (111) orientation is accompanied by an increase in surface roughness (Fig. 5.8) resulting in a faceted hill and valley structure as in the work of Je et al. [21]. It should be noted that in relevant studies a change from (002) to (111) is observed, but no tilted (002) texture is reported (except in the work of Je et al. [21]). Since they did not record pole figures for various Bragg reflections at different thicknesses the origin of their tilted textures remains unclear. The absence of any major change in surface morphology with film thickness (Fig. 5.6) coupled with the observation of smooth surface support the fact that the competitive grain growth mechanism is not active for films on silicon substrates. This is confirmed by TEM and AFM studies (Figs. 5.7c and 5.12) for thicker films in addition to low roughness values during film growth (Fig. 10) on Si. There is no indication of gradual competitive growth resulting in rougher surfaces, eventually leading to the development of (111) orientation, which is observed for films on WC-Co and glass at higher thicknesses. The observations support the notion that the (002) is the equilibrium growth surface for films on Si.

9.3 Biaxial texture formation in $Ti_{1-x}Al_xN$

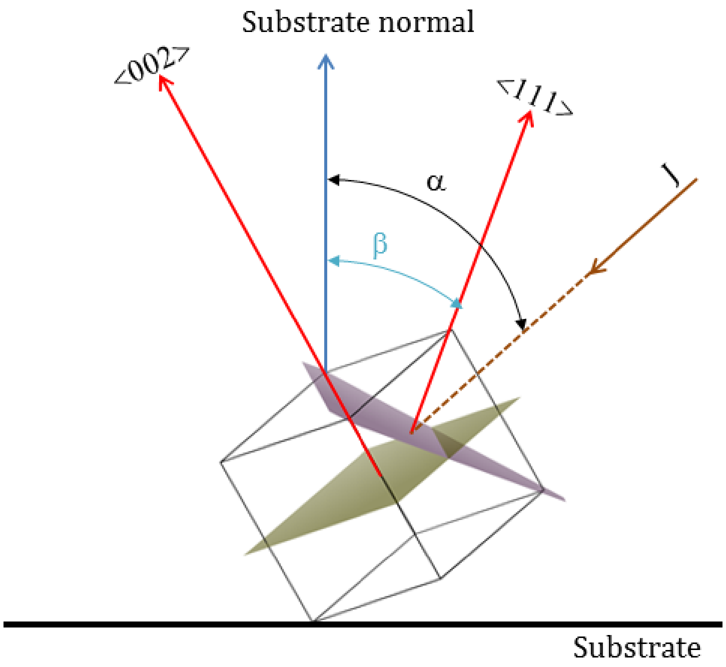

Fig. 9.6: *Schematic drawings showing the orientation relationship of the* $Ti_{1-x}Al_x$ *unit cell with respect to substrate and oblique flux. J corresponds to incident flux direction.* α *and* β *are the flux and column angles, respectively.*

For films deposited under oblique angle, the (111) and (002) mixed orientations are still present, but their directions are no longer parallel but tilted away from the film normal. This can be confirmed by the decrease in (111) and (002) peak intensities with deposition angle in the θ–2θ scans (Fig. 7.1). In an oblique angle deposition, the preferred orientation of the film is strongly dependent on the processing parameters. When depositions are carried out under the conditions of low adatom mobility (low temperature), the development of crystal planes will become dependent on the local angle of vapor incidence. Because of the limited mobility of adatoms, the atoms captured by the grains cannot redistribute on the growth surface, and grain growth will depend solely on the geometric distribution of flux as dictated by the self-shadowing construction, regardless of the initial grain shape or orientation.

The texture tilt observed in our case can be explained by the low adatom mobilities hence, high vertical growth rates of grains with different orientations and shadowing effects. As for in-plane alignments, if there existed a competition among the grains due to geometrical restrictions and mobility differences on different grains, then certain orientations would be favoured at the expense of others. Adatom mobility differences cause the grains to have different vertical growth rates. As one orientation grows taller, it wins the competition and stops further growth of the other orientations due to shadowing effects [22]. Deniz and Harper [23] studied the development of crystallographic texture in TiN films by OAD at room temperature. They observed that (002) planes are slightly tilted with respect to the substrate normal away from the ion beam source, and (111) planes are tilted 50° toward the ion beam source and concluded that the existence of biaxial texture in TiN films is due to kinetic effects such as geometrical effects rather than thermodynamic effects, i.e., surface mobilities of adatoms. We believe that lowering the surface mobilities, i.e., allowing kinetic effects to dominate, has an important role in forming the biaxial texture of the films as well as their crystal habits. In our case, the surface facing the incident flux is the (111) plane. The pole figure results indicate that (111) plane has the largest capture cross-section, and it turns towards the flux direction by outgrowth of grains with preferred orientation. The (002) plane rotates to grow away from the direction of incident flux when the substrate is inclined. These observations suggest that competition between (111) and (002) makes the columns grow with [002] direction closely perpendicular to the substrate surface while maintaining the minimization of surface free area by maximizing the (111) surface area (Fig. 9.6). The TEM bright field image and diffraction pattern show that the top face of the $Ti_{1-x}Al_xN$ column is the (002) plane (Fig. 7.7), thus supporting the pole figure results (Fig. 7.2). As the direction of incident flux is rotated away from the substrate normal by an angle α, the (111) crystal planes can only be maximized while maintaining the [002] preferred growth direction by balancing the two competing effects. In addition, the shadowing effect also defines the in-plane preferred orientation during the film growth. This is achieved by selecting crystals with the azimuthal orientation that has the highest vertical growth rate. This natural selection or physical self-assembly allows us to grow biaxial texture.

9.4 Effect of substrate temperature on the microstructure of OAD films

Increasing the substrate temperature resulted in a transition of voided columnar microstructure (at room temperature) to a much densified columnar structure. When the deposition is carried out at higher temperature, the mobility of the adatoms increases. Due to the increase in the substrate temperature, the adaparticles are able to overcome the diffusion barrier. That means the adatoms are able to diffuse on underlying crystals and grains, which show the occurrence of self-diffusion. At higher deposition temperature, the intergrain voids begin to fill up and the structure passes from porous columnar microstructure to a much densified columnar structure. Also, it can be seen that for all normal incidence deposition at all temperatures, no tilt in the columns was observed since the incident flux is arriving normal to the substrate.

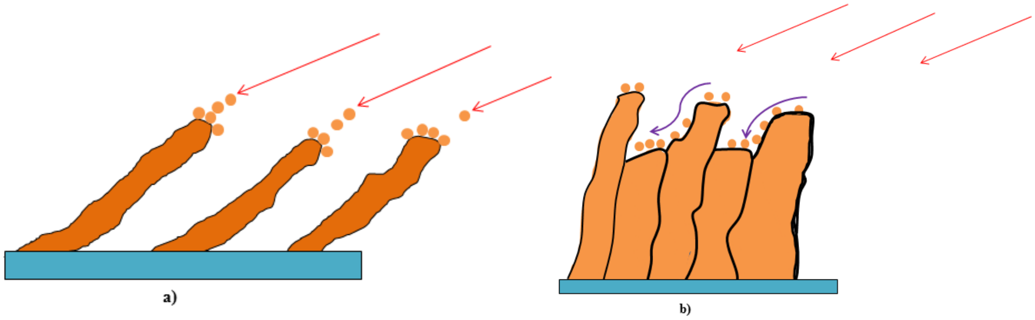

Fig. 9.7: *Schematic illustration of columnar structure for films deposited under oblique angles. At low temperature (a), the adatoms have no moblitiy and will stick to the growing film at the same place where they hit it. This results in a columnar structure separated by voids. When the deposition temperature is raised (b), the voids are now filled due to diffusion of adatoms thus enabling the columns to approach the film normal.*

Increasing substrate temperature leads to surface diffusion which tends the columnar structure towards the substrate normal. In an oblique angle deposition system, self-shadowing occurs and favors the formation of zone 1a structure of the Mahieu's model, which shows high porosity and low hardness (Fig. 9.7a) [24]. To reduce the porosity, the substrate temperature is generally increased to enhance the surface diffusion and fill the voids [25]. As the substrate temperature is increased, the spaces between the voids are getting closed up. Voids are known to form as a consequence of both surface roughness and shadowing effects. According to Dong et al. [26], at any deposition angle, increasing the temperature increases the mobility of atoms at the surface which is capable of overcoming the atomic shadowing effects that produces void (Fig. 9.7b). As the angle of incidence α is increased, the shadowing becomes more effective, and to overcome this problem the temperature must be further increased in order to produce a film with the same density as one produced at $\alpha = 0°$.

9.5 Reference

[1] S. H. Lim, D. G. McCulloch, M. M. M. Bilek, D. R. McKenzie, J. Appl. Phys. 93 (2003) 4283.

[2] M. Beckers, N. Schell, R. M. S. Martins, A. Mücklich, W. Möller, J. Appl. Phys. 98 (2005) 044901.

[3] F. Riesz, Vacuum, 46 (1995) 1021.

[4] L. J. Schowalter, E. L. Hall, N. Lewis, S. Hashimoto, Thin Solid Films, 184 (1990) 437.

[5] A. Yamada, P. J. Fons, R. Hunger, K. Iwata, K. Matsubara, S. Niki, Appl. Phys. Lett. 70 (2001) 608.

[6] E. C. Young, F. Wu, A. E. Romanov, A. Tyagi, C. S. Gallinat, S. P. DenBaars, S. Nakamura, J. S. Speck, Appl. Phys. Exp. 3 (2010) 011004.

[7] A. R. Shetty, A. Karimi, Appl. Surf. Sci. 258 (2011) 1630.

[8] J. Pelleg, L. Z. Zevin, S. Lungo, N. Croitoru, Thin Solid Films 197 (1991) 117.

[9] J. P. Zhao, X. Wang, Z. Y. Chen, S. Q. Yang, T. S. Shi, X. H. Liu, J. Phys. D, 30 (1997) 5.

[10] J. S. Chun, I. Petrov, J. E. Greene, J. Appl. Phys. 86 (1999) 3633.

[11] G. Abadias, Y. Y. Tse, J. Appl. Phys. 95 (2004) 2414.

[12] J. E. Greene, J. E. Sundgren, L. Hultman, I. Petrov, D. B. Bergstr, Appl. Phys. Lett. 67 (1995) 2928.

[13] A. van der Drift, Philips Res. Pep., 22 (1967) 267.

[14] A. R. Shetty, A. Karimi, M. Cantoni, Thin Solid Films 519 (2011) 4262.

[15] A. R. Shetty, A. Karimi, Phys. Status Solidi (b) 249 (2012) 1531.

[16] F. Adibi, I. Petrov, J. E. Greene, L. Hultman, J. -E. Sundgren, J. Appl. Phys. 73 (1993) 8580.

[17] L. Chekour, C. Nouveau, A. Chala, C. Labidi, N. Rouag, M.A. Djouadi, Surf. Coat. Technol. 200 (2005) 241-244.

[18] M.-A. Djouadi, C. Nouveau, O. Banakh, R. Sanjinés, F. Lévy, G. Nouet, Surf. Coat. Technol. 151-152 (2002) 510.

[19] C. Nouveau, M.A. Djouadi, O. Banakh, R. Sanjinés, F. Lévy, Thin Solid Films 398-399 (2001) 490.

[20] R. Carel. Ph.D. Thesis, Massachusetts Institute of Technology (1995).

[21] J. H. Je, D. Y. Noh, H. K. Kim, K. S. Liang, J. Appl. Phys. 81 (1997) 6126.

[22] D. Deniz, J. M. E. Harper, J. W. Hoehn, F. Chen, J. Vac. Sci. Technol. A 25 (2007) 1214.

[23] D. Deniz, J. M. E. Harper, J. Appl. Phys. 104 (2008) 063519.

[24] S. Mahieu, P. Ghekiere, D. Depla, R. De Gryse, Thin Solid Films, 515 (2006) 1229.

[25] C. Khare, J. Gerlach, M. Weise, J. Bauer, T. Hoche, B. Rauschenbach, Phys. Status Solidi A 208 (2011) 851.

[26] L. Dong, R. W. Smith, D. J. Srolovitz, J. Appl. Phys. 80 (1996) 5682.

Chapter 10:

Conclusions and future directions

The present results clearly exhibit that the texture development in fcc nitrides is a complex interplay between thermodynamic and kinetic forces at various stages of film growth.

- The results obtained by XRD distinctly suggest that grains with (002) orientation are present at low thickness to minimize the surface energy of the system. In a different manner, mechanism of kinetic nature such as the competitive growth promotes the growth of (111) orientation at higher thickness. Contrary to prediction of growth models, the (002)-oriented grains do not perish in the bulk by the rapid growth of (111) grains parallel to the film surface. Rather the (002) grains still constituted the surface but are tilted away with a preferential in-plane alignment in order to allow the growth of <111> parallel to the film normal. Meanwhile, the intrinsic stress along (002) changes from compressive to tensile with thickness due to these tilted <002> crystallites. On the other hand, the stress state of grains having (111) orientation parallel to film normal is compressive at higher thickness. The development of (111) texture is accompanied by an increase in surface roughness resulting in faceted hill and valley structure as confirmed by SEM. The TEM observation along with the SAED pattern supports the XRD results. The film only hardness was found to increase with thickness and this was attributed to the compressive stress stored in (111) grains and increase in (111) preferred orientation.

- However, the texture growth mechanism for $Ti_{0.5}Al_{0.5}N$ was found to be substrate dependent for depositions on Si. A dominant (002) texture is present from the onset of film growth up to the film surface. This indicates that the surface and interface energy anisotropy provide the driving force for texture development. The stress state along (002) remained compressive through the film thickness due to the absence of cross-over and other growth mechanism. TEM observations were in good agreement with XRD results regarding the texture formation on Si.

- In chapter 6, for titanium rich-TiAlN i.e $Ti_{0.67}Al_{0.33}N$ films, the growth mechanism was found to be similar to $Ti_{0.5}Al_{0.5}N$. However, the final dominant orientation parallel to film normal is <113> and not <111>. The crystallites remarkably exhibit the dominant (113) texture with increasing film thickness. The final orientation of (113) is evidenced to experience three different stages of film growth. The change in preferential orientation is accompanied with a change in morphology (increase in surface roughness) and a decrease in compressive stress that leads to a decline in hardness values. Our interpretation is that due to the high compressive stress formed in the (111) oriented grains, the growing film adopts the most suitable orientation -- less dense (113).

- We have shown in Chapters 7 and 8, $Ti_{1-x}Al_xN$ films responds to the incident flux direction by developing a biaxial texture alignment. The texture formation mechanisms of $Ti_{1-x}Al_xN$ films films deposited under various incidence angles have been investigated, and the crystallographic orientation relationship has been carefully addressed. It was found that the vapor incidence angle has great impact on the crystallographic orientation and morphology of the film. The texture of the films was analyzed by XRD and showed that under normal incidence ($\alpha = 0°$), the competitive growth between (111)- and (002)-orientations results in a mixed fiber texture with random in-plane alignments. On the other hand, for films deposited onto an inclined substrate, the (111) plane grows towards the flux direction to maximize its capture cross-section while the [002] growth direction is tilted away from the deposition source but nearly parallel to the substrate normal. The dependence of (111) texture tilt angle and column angle β on the incidence flux angle α follows the "tangent rule" only for low deposition angles. All the models deviated from experimental values at higher deposition angles. The inclination of columns and the in-plane alignment depend on the deposition angle. The surface morphology of obliquely deposited films exhibited a "roof-tile" or a "stepwise" shape, and a cross-sectional view showed a columnar structure tilted towards the incident flux direction. The cross-sectional TEM image revealed a voided and tilted columnar structure, while the SAED pattern of the same film supported the pole figure XRD results. Both hardness and Young's modulus decreases when the flux angle changes from $\alpha = 0°$ to 60°, due to the formation of voids under the shadowing effect. The tilt angles of (111) and (002) orientations decreases when substrate temperature is varied from RT to 650°C. In addition, the degree of in-plane alignment was found to be strongly dependent on substrate temperature. The inclination of columns decreases with increasing substrate temperature and they become homogenous thus decreasing the influence of flux angle.

While this thesis made progress along several areas regarding the texture formation mechanism in fcc nitrides, it is clear that many issues remain open. Some of the future directions emerging out of this thesis are listed below.

- One interesting point which is not discussed throughout the present study is to calculate and compare the surface and strain energy values of $Ti_{0.67}Al_{0.33}N$ and $Ti_{0.5}Al_{0.5}N$ for (111), (002), (022) and (113) reflections. Using simulations, Lim et al. reported the values for (111) and (002) of different TiAlN compositions such as $Ti_{0.25}Al_{0.25}N_{0.50}$. However, to the best of our knowledge, there has been no studies related to the strain and surface energy values for (113) plane of any TiAlN film composition. This is because the occurrence of (113) texture is not dominant in majority of the earlier studies. We believe that the film composition plays an important role in the (113) texture formation. For example, in chapter 4 we noticed the (111) orientation at higher thickness for $Ti_{0.5}Al_{0.5}N$, whereas using $Ti_{0.67}Al_{0.33}N$ (chapter 6), the (113) texture was observed. It would be interesting to calculate the surface and strain energies for (111), (002), (022), and (113) planes of TiAlN films with different film compositions.

- In chapter 4 and 6, we noticed the phenomena of off-axis tilt of (002) and development of (113) texture for TiAlN films with film thickness. These depositions were performed under non-bias conditions. The effect of substrate bias on the texture evolution for various thicknesses is another interesting direction. It is well known that texture of the coatings can be changed by the application of negative bias to the substrate. It would be appealing to the study the texture behaviour of $Ti_{1-x}Al_xN$ films with bias at higher thickness.

- We could extend our research work to study the absence of substrate dependence for $Ti_{0.67}Al_{0.33}N$ films on Si. This is in contrast to $Ti_{0.5}Al_{0.5}N$ films deposited on Si, where a dominant (002) texture was observed not changing with film thickness.

- Several studies have reported that the in-plane orientation distribution narrows as film thickness increases during OAD. Hence it would be of great interest to study the evolution of biaxial texture with film thickness for nitrides deposited under oblique angles.

Akshath R. Shetty

Avenue du Tir-Fédéral 92, Studio No 14
Lausanne, Vaud 1024, Switzerland

Cellular 0041783160380
akshathshetty@gmail.com

Areas of Interest

Challenging Materials Development / Research Management position specializing in thin film growth dynamics, nanostructure evolution, and characterization of thin films.

Educational Background

Doctor of Philosophy, Physics **2012**
EPFL, Lausanne, Switzerland
Research Guide: Dr. Ayat Karimi
Title of PhD thesis: Off-axis texture and crystallographic accommodation in multicomponent nitride thin films deposited by pulsed magnetron sputtering.
PhD defense expected: November 2012

Master of Science (By Research), Polymer Physics **2006**
University Institute of Chemical Technology (UICT), Mumbai, Maharashtra, India
Research Guide: Dr. R. R. Deshmukh
Title of M.Sc. Thesis: Plasma Processing of Polymeric Films and their Applications

Bachelor of Science, Physics **2002**
D. G. Ruparel, Mumbai, Maharashtra, India

Professional Highlights

EPFL, Lausanne, Switzerland **2009 - 2012**
Doctoral Assistant

- Involved in preparation and characterization of films of various compositions deposited on various substrates and studied its crystallographic, structural and mechanical properties.
- Conducted practical's for 3rd year graduate students. Teaching them to deposit ZnO:Al films by sputtering and characterizing its properties using various techniques like XRD, Van der Pauw method, Hall effect, optical properties, and surface morphology study by AFM.

KGL, Mumbai, India **2007 - 2009**
Associate Copyeditor

- Edited accepted manuscripts for reputed publishers like Elsevier, LWW and JBC. Proofreading of manuscripts. Copyedit manuscripts online and on hard copy.
- Joined the company as a trainee Copyeditor and promoted to Associate Copyeditor within a year.

- Knowledge of scientific, technical, and medical texts. Knowledge of the following styles: CBE, AMA, APA, Chicago, MLA.

Technical Expertise

- Transmission Electron Microscopy (TEM): able to prepare TEM lamellas by polishing and later by ion milling. Manipulated the microscope to observe the columnar structure and the crystal orientation of the films.
- High Resolution-Scanning Electron Microscopy (HR-SEM): employed to observe the surface morphology and fractured cross-section of the coatings. AFM was used to determine the surface roughness and observe the topography.
- Thorough knowledge of X-rays diffraction techniques like Bragg-Brentano and grazing incidence geometries to determine the crystallographic phases of samples. In addition, to obtain the texture of the coatings, pole figure XRD was used. The residual stress determined by $\sin^2\psi$ method.
- Experience in nanoindentation techniques to determine hardness and Young's modulus.
- Knowledge of PVD techniques by pulsed DC magnetron sputtering.
- Acquainted with techniques like the Hall effect, Van der Pauw method, optical studies and AFM during teaching assistantship period.
- Gained working knowledge of several analytical instruments like plasma processing unit, gas chromatography (GC), differential scanning calorimeter (DSC), FTIR spectroscopy, universal tensile machine (UTM) and electron spectroscopy for chemical analysis (ESCA) during Master’s thesis.

Computer Systems

Office Packages (MS Word, MS Excel, MS Power point)
Complete understanding of Windows OS, Web browsers
Adobe Acrobat Professional, Photoshop
Kaleidagraph
Completed DNIIT course from NIIT securing 62%

Awards and Scholarships

- Off-axis texture and crystallographic accommodation in multicomponent nitride thin films deposited by pulsed magnetron sputtering, Swiss National Science Foundation, Switzerland, 2009 – 2012 - Scholarship for PhD thesis.
- Sir Ratan Tata Scholarship, Sir Ratan Tata Trust, Mumbai, India, 2004 - 2006 - Scholarship for Master's thesis.

Professional Training

- Practical Course in Diffraction Methods-Laboratory of Crystallography (LCR).
- Intensive TEM and SEM training course-Interdisciplinary Centre for Electron Microscopy (CIME) .

Articles and Publications

AT EPFL

- "Formation of (113) texture in fcc nitrides thin films and its influence on the film properties"
  Thin Solid Films, 2012.
  A. R. Shetty and A. Karimi
  Accepted, In press

- "Texture mechanisms and microstructure of biaxial thin films grown by oblique angle deposition"
  Phy. Stat. Sol B. April 2012, 1531-1540.
  A. R. Shetty and A. Karimi
  http://dx.doi.org/10.1002/pssb.201248010

- "Texture change through film thickness and off-axis accommodation of (002) planes"
  Appl. Surf. Sci. October 2011, 1630-1638.
  A. R. Shetty and A. Karimi
  http://dx.doi.org/10.1016/j.apsusc.2011.10.037

- "Effect of deposition angle on the structure and properties of pulsed-DC magnetron sputtered TiAlN thin films"
  Thin Solid Films. March 2011, 4262-4270.
  A. R. Shetty, A. Karimi, and M. Cantoni
  http://dx.doi.org/10.1016/j.tsf.2011.02.090

- "Structure and Properties of TiAlN Thin Films At Oblique Angle"
  European Conference on Nano Films. March 2010.
  A. R. Shetty and A. Karimi

- "Deposition and characterization of pulsed direct current magnetron sputtered $Al_{95.5}Cr_{2.5}Si_{2}$ $(N_{1-x}O_{x})$ thin films"
  Thin Solid Films. October 2010, 319-324.
  H. Najafi, A. Shetty, A. Karimi, and M. Morstein
  http://dx.doi.org/10.1016/j.tsf.2010.07.080

- " Mechanisms of crossover through film thickness and effect of different substrate"
  J. Vac Sci. Technol. A
  A. R. Shetty, A. Karimi, A. Neels, and A. Dommann
  Under review

AT UICT

- "Surface characterization of polyethylene films modified by gaseous plasma"
  J. Appl. Polym. Sci. April 2007, 449-457.
  R. R. Deshmukh and A. R. Shetty
  http://dx.doi.org/10.1002/app.25554

- "Modification of polyethylene surface using plasma polymerization of silane"
  J. Appl. Polym. Sci. December 2007, 4075–4082.
  R. R. Deshmukh and A. R. Shetty
  http://dx.doi.org/10.1002/app.26957

- "Comparison of surface energies using various approaches and their suitability"
  J. Appl. Polym. Sci. March 2008, 3707–3717.
  R. R. Deshmukh and A. R. Shetty
  http://dx.doi.org/10.1002/app.27446

Conferences and Seminar

- "Texture Change and Off-axis Accommodation Through Film Thickness in *fcc* Structured Nitrides"
  A. R. Shetty and A. Karimi
  Poster presented at 39th International Conference on Metallurgical Coatings and Thin Films
  April 23-27, 2012 San Diego, CA.

- "Structure and Properties of TiAlN Thin Films At Oblique Angle Deposition"
  A. R. Shetty and A. Karimi
  Poster presented at European Conference on Nano Films
  March 22-25, 2010 Liege, Belgium.

- "Pole Figure and Bragg-Brentano X-Ray Diffraction Geometries to Study Tilted Texture and its Evolution through the Film Thickness"
  A. R. Shetty and A. Karimi
  Poster presented at International Conference on Metallurgical Coatings and Thin Films
  April 26-30, 2010 San Diego, CA.

Background Summary

Gender	: Male
Date of birth	: January 31, 1982
Nationality	: Indian
Marital Status	: Single
Languages known	: English, Hindi, Marathi, Kannada, Tulu, French (Basic)